# Stability of Controlled Mechanical System with Parametric Uncertainties in a Realistic Friction Model

by

Yun-Hsiang Sun

A Thesis submitted to the Faculty of Graduate Studies of
The University of Manitoba
in partial fulfillment of the requirements of the degree of

Doctoral of Philosophy

Department of Mechanical Engineering
The University of Manitoba
Winnipeg, Manitoba, Canada
February 2016

Advisor
**Christine Q. Wu**

Author
**Yun-Hsiang Sun**

**Stability of Controlled Mechanical System with Parametric Uncertainties in a Realistic Friction Model**

# Abstract

Friction compensation is always challenging but imperative for control engineers. For high-performance engineering systems, a friction-model-based controller is typically required to accommodate the nonlinearities arisen from the friction model employed. It is well known that the parameters of the friction model used in the friction compensation are nearly impossible to be accurately identified. Therefore, the objective of this research is to study the effect of these parametric uncertainties on the stability of a set-point position control system.

With the above goal in mind, a variety of aspects are investigated in this work. Firstly, several common friction features and friction models are surveyed to provide some background knowledge which helps select the friction model with the highest accuracy for our study. Secondly, an experimental setup is proposed and fabricated to validate the levels of accuracy given by the candidate friction models. The comparisons between the numerical and experimental results confirm that the LuGre friction model is the best approximation of the observed friction behaviours among all models selected. Moreover, a series of profound discussions addressing the relation between the candidate models' structures and their numerical friction feature predictions are provided and followed by a summary table that recapitulates the properties of the candidate friction models. Last but not least, the state space models of the proposed setup formulated by the improved version of the LuGre model and the two controllers of interest, namely input-output linearization controller and nominal characteristic trajectory following (NCTF) controller, are derived for the stability analysis under the parametric uncertainties. Two parameters in the friction model used, $\sigma_0$ and $\sigma_1$, are perturbed for the stability analysis in which the results applying the concept of

Lyapunov exponents (LEs) clearly illustrate the significant effect of the varying $\sigma_0$ and $\sigma_1$ values on the system stability. For the input-output linearization controller employed to perform the set-point position control on our setup, the minor perturbations less than 0.01% off the nominal values of the studied parameters can result in limit cycles and even diverging system states; by contrast, the NCTF controller demonstrates better robustness where the system's qualitative behaviour remains unchanged when the studied parameters are perturbed 30% more or less with respect to the nominal values.

The effect of parametric uncertainties can depend quite significantly on the incorporated controller, and the stability results obtained here are applicable to the design and analysis of other systems that are inherently similar to our setup. The stability analysis conducted is this work is recommended for other control systems to avoid unwanted qualitative behaviours under parametric perturbations.

*This thesis is dedicated to the people who kept me going when I wanted to give up.*

# Acknowledgments

I would like to begin by thanking my advisor Dr. Christine Wu and co-advisor Dr. Nariman Sepehri. Their guidance, insights and support have been invaluable in completion of this research. I would like to also acknowledge the effort and input of my committee members Dr. Udaya Annakkage and Dr. Qingjin Peng. I would like to express my gratitude to Dr. Cyrus Shafai who kindly shared his expertise in MEMS with me.

I am grateful for those who helped me with building testing setup and data interpretation. I would like to thank Yuming Sun for helping me with stability analysis carried out in my work. Nishant Balakrishnan, Mansoor Alghooneh and Tao Chen helped me refine my setup, for which I am very appreciative. Sushil Doranga, Khashayar Pejhan and Graham Leverick are my good friends and I will not forget the good time we have shared during this program. Also, I would like to thank Ehsan Jalayeri for ordering equipments for my setup.

I would like to acknowledge the financial support from NSERC, the University of Manitoba, the Faculty of Engineering, the Department of Mechanical Engineering and the Faculty of Graduate Studies.

I am also grateful for the encouragement and patience of my family. Thanks for listening to me talking about my research for the past four years. Finally, this thesis would not have been possible without the unconditional love and encouragement of my beloved wife Rui Zhou. Thanks for being the only support I have ever had and I will ever be needing.

# Contents


Abstract . . . . . ii
Dedication . . . . . iv
Acknowledgments . . . . . v
Table of Contents . . . . . viii
List of Figures . . . . . ix
List of Tables . . . . . xii

**1 Introduction** **1**
1.1 Motivation . . . . . 1
1.2 Background and Related Work . . . . . 2
1.2.1 Features of Friction . . . . . 3
1.2.1.1 Break-away force . . . . . 3
1.2.1.2 Viscous friction . . . . . 3
1.2.1.3 Varying break-away force . . . . . 4
1.2.1.4 Friction lag . . . . . 4
1.2.1.5 Presliding . . . . . 5
1.2.2 Friction Models . . . . . 6
1.2.2.1 Classical Model . . . . . 6
1.2.2.2 Dahl Model . . . . . 6
1.2.2.3 Bliman and Sorine Model . . . . . 8
1.2.2.4 LuGre Model . . . . . 10
1.2.2.5 Numerical Accuracy of Various Friction Models . . . 11
1.2.3 Experimental Setups . . . . . 13
1.2.3.1 Friction Oscillator . . . . . 13
1.2.3.2 DC motor . . . . . 13
1.2.3.3 Self-excited System . . . . . 15
1.2.4 Stability Analysis of Systems with Friction . . . . . 16
1.3 Thesis Objectives and Methodology . . . . . 20
1.4 Organization of Thesis . . . . . 21

**2 Development of One-dimensional Sliding Block Experimental Setup 22**
2.1 Introduction . . . 22
2.2 Approach . . . 23
2.2.1 Setup Design . . . 23
2.2.2 Design of Capacitance Displacement Sensor . . . 26
2.2.3 Friction Estimation . . . 30
2.3 Parameter Identification . . . 32
2.3.1 Classical Model . . . 32
2.3.1.1 Procedure . . . 32
2.3.1.2 Results . . . 32
2.3.2 Dahl Model . . . 34
2.3.2.1 Procedure . . . 34
2.3.2.2 Results . . . 35
2.3.3 Bliman and Sorine Model . . . 38
2.3.3.1 Procedure . . . 38
2.3.3.2 Results . . . 40
2.3.4 LuGre Model . . . 43
2.3.4.1 Procedure . . . 43
2.3.4.2 Results . . . 44
2.4 Feature Comparison . . . 46
2.4.1 Experimental Trials for Feature Demonstration . . . 46
2.4.2 Break-away Force . . . 48
2.4.3 Viscous Friction . . . 50
2.4.4 Friction Lag . . . 52
2.4.5 Varying Break-away Force . . . 55
2.4.6 Presliding . . . 56
2.4.7 Comparison of Candidate Friction Models . . . 60
2.5 Summary . . . 63

**3 Stability Analysis 65**
3.1 Introduction . . . 65
3.2 Concept of Lyapunov Exponents . . . 66
3.3 State Space Model . . . 70
3.4 Controller Design and Simulations . . . 73
3.4.1 Input-Output Linearization Controller . . . 73
3.4.1.1 Development of Controller . . . 73
3.4.1.2 Simulation Results . . . 74
3.4.2 Nominal Characteristic Trajectory Following (NCTF) Controller 76
3.4.2.1 Development of Controller . . . 76
3.4.2.2 Simulation Results . . . 80
3.5 Effect of Parametric Uncertainties . . . 82

3.5.1 Structural Stability Analysis for Input-Output Linearization Controller . . . 82
3.5.1.1 Perturbed System 1: . . . 82
3.5.1.2 Perturbed System 2: . . . 83
3.5.1.3 Perturbation Region $\Gamma_1$ . . . 85
3.5.2 Structural Stability Analysis for NCTF Controller . . . 88
3.5.2.1 Perturbed System 1: . . . 89
3.5.2.2 Perturbed System 2: . . . 91
3.5.2.3 Perturbation Region $\Gamma_2$ . . . 91
3.6 Summary . . . 94

**4 Conclusions** **96**
4.1 Contributions . . . 96
4.2 Future Work . . . 98

**Appendix: Detailed description of $f(x)$ and $\hat{f}(x)$** **99**

**References** **101**

# List of Figures


1.1 True contact surfaces shown in micro-scale. The physical properties of the involved asperities give rise to the friction within this regime. . . 3
1.2 Break-away force versus force loading rate. The curve becomes steeper as the force rate moves toward left. . . . . 4
1.3 Loop observed on the friction-velocity map showing a multi-value behavior. . . . . 5
1.4 Microfine displacement with applied force. . . . . 5
1.5 Velocity-friction relation of Classical model. . . . . 7
1.6 Dahl model showing position dependency of friction. . . . . 8
1.7 Friction hysteresis cycle. $x_e$ is the displacement where the break-away force $F_s$ is experienced. Friction converges to Coulomb friction $F_c$ for relative displacement greater than $x_p$. $x_p$ is the displacement which makes the $\frac{|F(x_p)-F_c|}{F_c^2}$ equal to 5%. . . . . 9
1.8 (a) Contact area between two solid bodies is thought of as a contact between bristles. (b) The average deflection of the bristles between the contact area is represented by a single bristle with the average deflection $z$. . . . . 11
1.9 Stribeck curve characterizes friction as a function of velocity. . . . . 12
1.10 (a) General view of the friction oscillator proposed in [1]. 1-shaker; 2-pneumatic actuator; 3-friction tongue; 4-guiding post; 5-case of LVT and LVDT; 6-mass; 7-accelerometer; 8-force transducer; 9-coil springs; 10-clamping device. (b) Simplified model of the friction oscillator [1]. 14
1.11 (a) Typical DC motor with encoder and gear head. (b) Friction versus velocity [2]. . . . . 15
1.12 (a) Self-excited system model. (b) Phase portrait of mass block [3]. . 16
1.13 State trajectory of single mass system with position PID control [4]. 17
1.14 General view of experimental rig [5]. . . . . 18
1.15 (a) Block diagram of system with friction compensation and PD control [5]. (b) Limit cycle generation map [5]. . . . . 19
1.16 Inclined-spring model [6]. . . . . 20

2.1 Photo of sliding table. . . . . 24
2.2 Control loop, power source and the sensing system. . . . . 25
2.3 (a) Tools to build the sensor. (b) Transmission of measurement data to Simulink environment. AD7747 helps convert the analog capacitance signal to digital, and MX7-ck board transmits the digital signal to Matlab. . . . . 27
2.4 (a) Installation of two conducting plates. (b) Vertical clearance between the table surface and the conducting plate edge. (C)Left: schematic and notations for a parallel-plate capacitor. Right: two square conducting plates with a square overlap area are used to form the capacitor. 29
2.5 Calibration curve versus experimental measurements. . . . . 30
2.6 (a) Close-up view of the brass block and the aluminium table under. (b)Schematic of the sliding block subject to friction. . . . . 30
2.7 Friction-velocity map: experimental findings and classical model output. 33
2.8 Experimental data and fitted curve (trial No. 7). . . . . 37
2.9 Identified parameters spreading out within two standard deviation band. 38
2.10 (a) Input profile giving block cyclic motion and its resultant hysteresis loop. (b) Selected two reference points plotted on break-away region in zoom. (c) Model estimation versus realistic friction profile. . . . . 41
2.11 Experimental results obtained from a representative trial. . . . . 45
2.12 Identified parameters spreading out within two standard deviation band. 46
2.13 Desired input force trajectory used to demonstrate presliding. . . . . 48
2.14 Static friction-velocity map together with break-away force reproduced by selected models. . . . . 51
2.15 Viscous friction behaviour under static velocity profiles. . . . . 53
2.16 Friction lag characteristics of friction (unidirectional velocity variation, slide sinusoidally within $0.5-2.5\,mm/s$, freq.=$0.48\,Hz$, two successive cycles of velocity variation are plotted). . . . . 54
2.17 Relation between break-away force and force rate. . . . . 56
2.18 Presliding measurements along with model predictions (slope=$0.25\,N/s$) 58
2.19 Presliding response of Dahl model due to instantaneous change in input force. . . . . 59

3.1 Evolution of 2-dimensional infinitesimal sphere. . . . . 67
3.2 Graphical interpretation of GSR for a set of 2D vectors. . . . . 69
3.3 Block diagram of plant with controller. . . . . 70
3.4 Numerical time response of displacement. . . . . 75
3.5 Voltage source applied to motor during set-point position control. . . 76
3.6 Structure of NCTF control system. . . . . 76
3.7 Construction of NCT. . . . . 79
3.8 NCT and curve fitting results. . . . . 80
3.9 Numerical time response of displacement. . . . . 81

3.10 Voltage source applied to motor during set-point position control. . . 81
3.11 States $x_1$ and $x_2$ of input-output linearization control system. . . . . 83
3.12 States $x_3$ and $x_4$ of input-output linearization control system. . . . . 83
3.13 Evolution of system Lyapunov exponents (ordered in decreasing value). 84
3.14 State $x_1$ and $x_2$ of input-output linearization control system. . . . . 84
3.15 States $x_3$ and $x_4$ of input-output linearization control system. . . . . 85
3.16 Phase portrait for system states $x_1$ and $x_2$. . . . . 85
3.17 Evolution of system Lyapunov exponents (ordered in decreasing value). 86
3.18 Structure stability region of experimental rig determined by the simulation results. The golden star pins on the nominal $\sigma_0$ and $\sigma_1$ values. 87
3.19 States $x_1$ and $x_2$ of NCTF control system. . . . . 89
3.20 States $x_3$, $x_4$ and $x_5$ of NCTF control system. . . . . 90
3.21 Evolution of system Lyapunov exponents (ordered in decreasing value). 90
3.22 States $x_1$ and $x_2$ of NCTF control system. . . . . 92
3.23 States $x_3$, $x_4$ and $x_5$ of NCTF control system. . . . . 92
3.24 Evolution of system Lyapunov exponents (ordered in decreasing value). 93

# List of Tables


1.1 Definition of states for the signal mass system with position PID control. 17

2.1 Parameters of motor, ball screw and load cell . . . . . 25
2.2 Desired step input force values for classical model parameter identification. . . . . 33
2.3 Nominal model parameters for classical model. . . . . 34
2.4 Desired velocity trajectories for Dahl model parameter identification. 35
2.5 Nominal model parameters for Dahl model. . . . . 38
2.6 Desired velocity trajectories for B.S. model parameter identification. . 39
2.7 Identified parameters for B.S. model. . . . . 42
2.8 Desired step input force values for LuGre model dynamic parameter identification. . . . . 43
2.9 Identified parameters for LuGre model. . . . . 46
2.10 Desired step input force values for break-away force demonstration. . 47
2.11 Desired velocity trajectories for friction lag demonstration. . . . . 47
2.12 Summary of candidate friction models. . . . . 62

3.1 Physical interpretation of parameters and their nominal values . . . . 72
3.2 Definition of states . . . . . 72
3.3 Largest Lyapunov exponents for perturbed systems subject to region $\Gamma_2$. 94
3.4 Largest Lyapunov exponents for perturbed systems subject to region $\Gamma_2$ (cont'd). . . . . 94

# Chapter 1

# Introduction

## 1.1 Motivation

Friction appears in all mechanical systems incorporating parts in contact and with relative motion. Although friction can be desirable in certain applications, such as for brakes, it in general has negative influences on the efficiency and the motions of the mechanical systems; thus, it is necessary to have a proper friction compensation action which leads to a satisfactory performance. Several control strategies have been proposed to date to compensate the undesired effects of friction. They are generally categorized as friction-model-based and non-friction-model-based. The former is usually easier to implement in practice and could offer strong robustness but requires an accurate friction model [7] at the design phase. The latter normally considers friction as a disturbance when designing the control strategy, however, it imposes more constraints on studied setups as pointed out in [7]. It is then concluded that none of these two types of strategies is superior to another, considering the pros and cons arisen inherently from each of them. However, for the friction-model-based control strategies, the parameters in friction model have been proven difficult to estimate precisely [6, 8, 9] due to unmodelled dynamics, measurement noise, material aging, and so far few studies have focused on exploring the effect of such parameter uncertainties on the control system stability.

In order to bridge the gap pointed out above and provide researchers with in-

sights into the ability of the chosen controllers to withstand the uncertainties when performing the control tasks, a variety of aspects are discussed in this work: starting with an introduction of various friction features and friction models, continuing with a survey of existing experimental setups that have been taken to produce accurate friction data, and finishing with a discussion of the existing works that uncover the effect of parametric uncertainties on the system stability.

## 1.2 Background and Related Work

In this section, a group of features of friction are firstly reviewed. The feature selection is by no means complete but covers most of the features occurring during the static regime, dynamic regime, and the transition between the two. A more thorough discussion of the mechanisms behind these features can be found in [10]. It may not be necessary to master the true mechanism behind each feature, but it is imperative to have a good model for these features.

The review of a group of friction models, including the static classical friction model and three dynamic friction models, is presented in this section. These models are selected in this work due to their long history and popularity in the control discipline. References [1, 11–15] suggested several advanced friction models in which the switching functions and too many parameters are used to describe the friction. These models are excluded in this work since they are too complicated to apply in practical engineering problems.

Several existing and popular experimental setups in the friction-related studies are also surveyed in this section. General diagrams of these setups are provided along with some experimental data to give the readers a better understanding on the type of the frictional contact and the dynamics of the conducted tests. These setups are valuable tools in analyzing and modelling of the friction.

Finally, some works addressing the stability of systems are surveyed in which the frictional parameters are perturbed in a bounded range. Different stability analysis techniques and friction models are employed to carry out the analysis in literature where the results can provide general description and stability conditions of the

studied systems. The parametric perturbations can affect not only the qualitative behaviours of a system but also can produce a destabilizing effect on the system, depending on the degree of the perturbations. They should be studied carefully to avoid the occurrence of the undesired behaviours of the systems.

### 1.2.1 Features of Friction

#### 1.2.1.1 Break-away force

When examined on a microscopic scale, two contact surfaces are connected by a large number of asperities as shown in Fig. 1.1. The break-away force is the force required to slip the asperities and results in the continuous motion of the object. Researchers usually postulate that the break-away force remains a constant if there is no significant change in operating conditions. Friction decreases and converges to sliding friction right after the break-away force is reached.

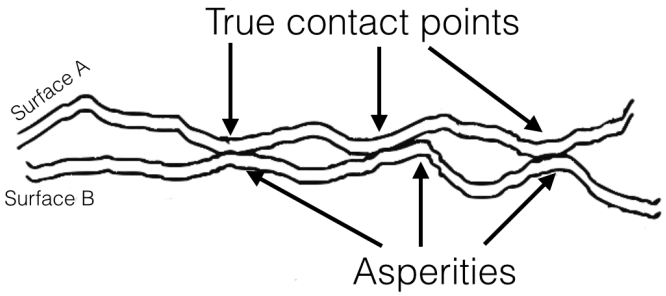


Figure 1.1: True contact surfaces shown in micro-scale. The physical properties of the involved asperities give rise to the friction within this regime.

#### 1.2.1.2 Viscous friction

Viscous friction accounts for the friction behaviour of an object sliding with gross motion, such a friction is approximated as a linear function of the velocity. Overall the viscosity of the lubricant governs the friction in this regime. However, references [16–18] revealed that the linear function does not adequately capture the friction

observed within this regime, instead, the more sophisticated equations proposed by the authors fit the experimental observations better.

#### 1.2.1.3 Varying break-away force

It is experimentally found that the break-away force varies with force loading rate as can be seen in Fig. 1.2 rather than a constant. The break-away force is greater with low loading rate and the curve remains constant once the critical value of loading rate is reached, where the critical value differs from case to case. This feature of friction was confirmed in [19, 20]. The same feature were observed in [21, 22], though the authors did not focus on this phenomenon.

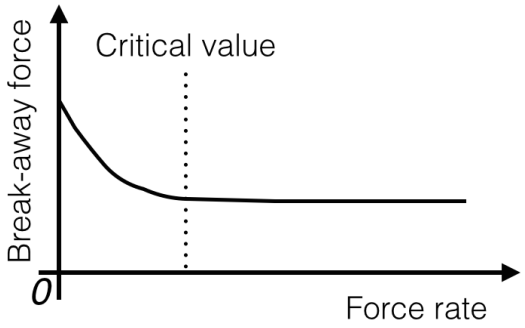


Figure 1.2: Break-away force versus force loading rate. The curve becomes steeper as the force rate moves toward left.

#### 1.2.1.4 Friction lag

Hess and Soom studied the friction of a line contact observed during unidirectional motion [23] with changing velocity. As shown in Fig. 1.3 the friction is lower during the deceleration period than the acceleration period. Such a loop always surrounds the Stribeck curve clockwise during the oscillating velocity. It has been shown in [23] that for a given load and lubricant, a constant time delay can be observed between a changing velocity and the corresponding friction. The authors justified that such a time delay results in the loop showing on the friction-velocity map in Fig. 1.3. However, the study of friction lag is not subject to unidirectional motion as performed in [23], other works concerned with bidirectional motion can be found in [1, 24–28].

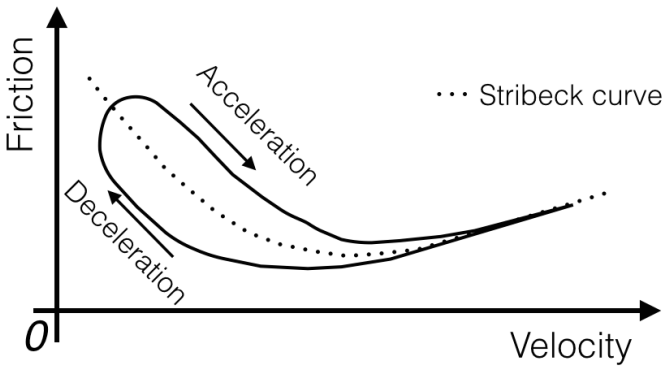


Figure 1.3: Loop observed on the friction-velocity map showing a multi-value behavior.

#### 1.2.1.5 Presliding

Applying an input force lower than the break-away force on the object can produce a microfine displacement between the contact junction. The microfine displacement is usually on the scale of a few micrometers and is alternatively called presliding because such a displacement occurs before the gross sliding. It is well-known that a contact surface behaves like a spring in the presliding region, as described in Fig. 1.4. This is to say, the microfine displacement is approximately a linear function of the applied force. Studies on presliding can be found in [10, 29, 30]. The review of

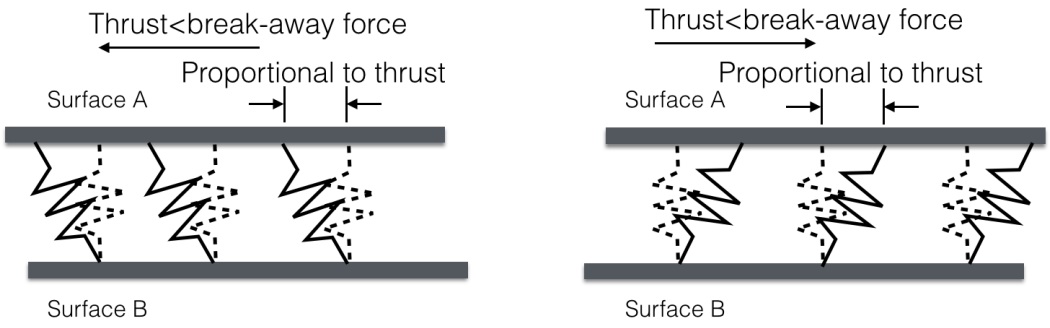


Figure 1.4: Microfine displacement with applied force.

the friction features stops at here and the four friction models of interest are reviewed below along with the physical interpretation of the parameters.

### 1.2.2 Friction Models

#### 1.2.2.1 Classical Model

The Classical model [31] consists of three components, the Coulomb friction [10], the static friction and the viscous friction and has the form of

$$F = \begin{cases} F_e & if\ v = 0\ and\ |F_e| < F_s \\ F_c sgn(v) + \sigma_2 v & if\ v \neq 0 \\ F_s sgn(F_e) & if\ v = 0\ and\ |F_e| \geq F_s \end{cases} \tag{1.1}$$

where $F$ is the friction, $v$ is the velocity, $F_e$ is the external force, $F_s$ is the break-away force, $F_c$ is the Coulomb friction and $\sigma_2$ is the viscous friction coefficient. The static friction describes the friction counteracting the external input, $F_e$ when objects are at rest. Thus, during the static stage, the friction is equal to the external force. Once the break-away force, $F_s$ is reached, the object under observation begins to slide.

The friction is estimated by adding the effect of the Coulomb friction and the viscous friction together while the observed object is in motion. The basic idea of the Coulomb friction, $F_c$, is that the friction opposes motions arising from external loading, and its magnitude is independent of the contact area and velocity, but proportional to the normal load. The viscous friction accounts for the lubricants effect on the friction. It is velocity-dependent and varies linearly.

Figure 1.5 demonstrates the Classical model. The break-away force, $F_s$, does not account for the friction at null velocity; on the contrary, it can take on any value between $\pm F_s$ to balance the external force. Once the velocity is not null, the friction estimation becomes the superposition of the Coulomb friction and the viscous friction.

#### 1.2.2.2 Dahl Model

Dahl completed a series of papers [29, 32, 33] since 1968, which detailed the fundamental differences between sliding friction and rolling friction. The interface bond material properties dictate the former, while the latter is mainly governed by tension and compression properties of the object. A conclusion was made that the static friction was not distinctly identifiable in rolling friction. A dynamic friction

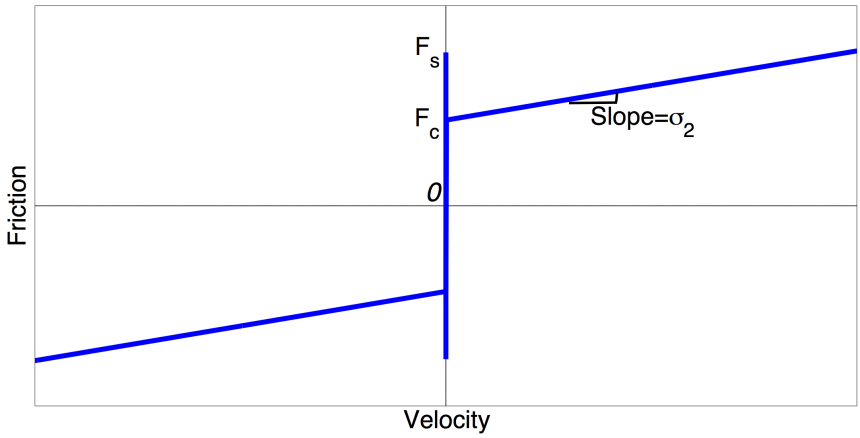


Figure 1.5: Velocity-friction relation of Classical model.

model, named as Dahl model, was developed to simulate the friction in a bearing, and has the form of

$$\frac{dF}{dx} = \sigma \left(1 - \frac{F}{F_c} sgn\left(v\right)\right)^{\alpha} \tag{1.2}$$

where $F$ is the friction, $x$ is the displacement, $\sigma$ determines the slope of the friction curve at $F = 0$, $F_c$ is the Coulomb friction, and $\alpha$ determines the shape of the friction curve. Notice that the friction is only a function of the sign of the velocity and the displacement($x$), and the friction will never go beyond $\pm F_c$ if its initial value $|F\left(0\right)| < F_c$. Figure 1.6 graphically illustrates how the friction varies with respect to the displacement. What intrigues us in this figure is the behaviour of friction after the velocity reversal point, where the direction of the friction does not follow instantly upon a change in velocity direction. Instead, there is a finite regime in which the friction settles from the $F_c$ to 0. This particular phenomena arises primarily from presliding region with switching $sgn\left(v\right)$, where the resistance to motion is overcome by the energy stored due to the deformation of the elastic member at the contact junctions. This interesting phenomena was experimentally observed by Dahl in his testing with bearings [29] and had been discovered by several researchers later.

A time domain model can be obtained by relating $dF$ and $dt$ using the chain rule

$$\frac{dF}{dt} = \frac{dF}{dx}\frac{dx}{dt} = \frac{dF}{dx}v = \sigma\left(1 - \frac{F}{F_c}sgn\left(v\right)\right)^{\alpha} v \tag{1.3}$$

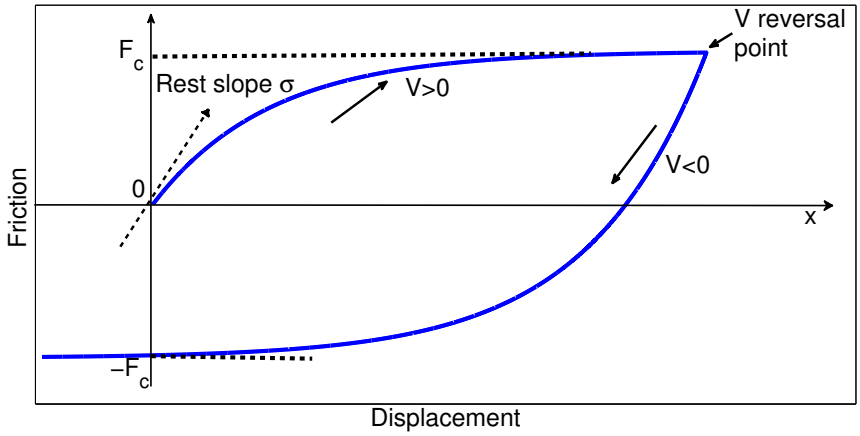


Figure 1.6: Dahl model showing position dependency of friction.

Dahl model avoids the discontinuity spoiling theoretical analysis. However, the ability to predict basic friction features such as sliding friction and break-away force is beyond its scope, leaving the motivation for extensions of Dahl model.

#### 1.2.2.3 Bliman and Sorine Model

This model was developed by Bliman and Sorine in a series of papers published since 1991 [34–36]. The authors emphasized that the friction is not explicitly velocity-dependent, instead it depended on the distance traveled after a zero velocity crossing. The model captures some friction features as follows: Firstly, it reproduces the basic features of friction such as break-away force, Coulomb friction, friction hysteresis cycle and presliding; Secondly, it is a dissipative model since the friction naturally dissipates energy at all times; Thirdly, the identification of the parameters is straightforward once the friction hysteresis cycles produced by the experiments are available. The

Bliman and Sorine model has the form of

$$\begin{aligned} \frac{dx_{s1}}{dt} &= |v| \frac{-x_{s1}}{\eta \varepsilon_f} + \frac{f_1 v}{\eta \varepsilon_f} \\ \frac{dx_{s2}}{dt} &= |v| \frac{-x_{s2}}{\varepsilon_f} - \frac{f_2 v}{\varepsilon_f} \\ F &= x_{s1} + x_{s2} \end{aligned} \tag{1.4}$$

where the $x_{s1}$ and $x_{s2}$ are two states added to produce the friction $F$. $f_1$, $f_2$, $\eta$, and $\varepsilon_f$ do not embrace any physical meanings but are determined through two reference points selected on the friction hysteresis cycle, as can be seen in Fig. 1.7. The first reference point $(x_e, F_s)$ is chosen based on the presence of break-away force $F_s$ and its corresponding displacement $x_e$. The friction approaches the Coulomb friction $F_c$ for the displacement grater than $x_p$. This information is used to form the second reference point $(x_p, F_c)$. Note that the second reference point does not have to lie on the hysteresis cycle.

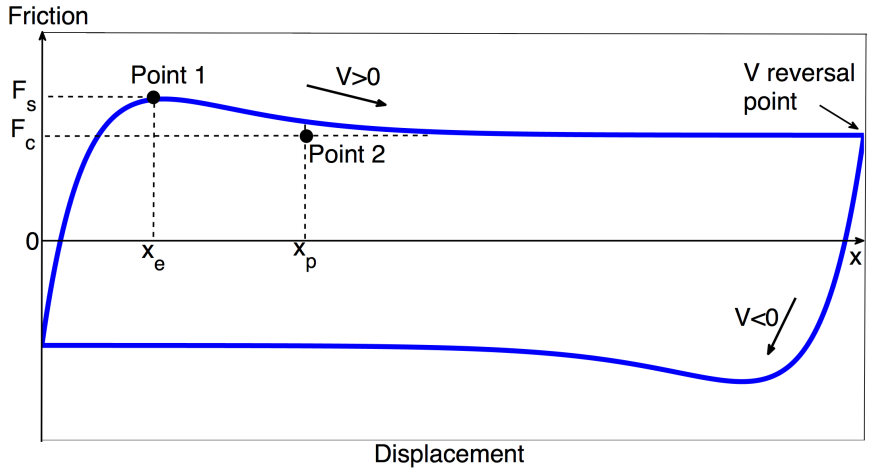


Figure 1.7: Friction hysteresis cycle. $x_e$ is the displacement where the break-away force $F_s$ is experienced. Friction converges to Coulomb friction $F_c$ for relative displacement greater than $x_p$. $x_p$ is the displacement which makes the $\frac{|F(x_p)-F_c|}{F_c^2}$ equal to 5%.

#### 1.2.2.4 LuGre Model

Friction models developed after the 80's have become more sophisticated since the qualitative mechanisms of friction were fairly well understood by taking advantage of tribology. When examined on a microscopic scale, the contact surface is extremely irregular due to the presence of a number of asperities, and it was proved that the junctions deform elastically before the lubricant enters, completely separating two solid bodies [10]. The authors of the LuGre model [37] visualized that two rigid bodies were in contact through elastic bristles, which will deflect, giving rise to the friction force when a tangential force is exerted on the mass. When the tangential force is high enough the bristles become over-deflected, the stationary mass then becomes a slider. Figure 1.8 graphically conveys this notion to readers. The average deflection of the bristles $z$ is modelled by

$$\frac{dz}{dt} = v - \frac{\sigma_0 |v|}{g(v)} z \tag{1.5}$$

where $v$ is the relative velocity between two surfaces, $\sigma_0$ is the stiffness of the bristles, $g(v)$ is a function given by

$$g(v) = F_c + (F_s - F_c) e^{-(v/v_s)^2} \tag{1.6}$$

where $F_c$ is the Coulomb friction, $F_s$ is the break-away force, and $v_s$ is the Stribeck velocity. The friction model suggested in [37] that regards the aggregate behavior of the bristles has the form of

$$F = \sigma_0 z + \sigma_1 \frac{dz}{dt} + \sigma_2 v \tag{1.7}$$

where $\sigma_1$ is the damping of the bristles, and $\sigma_2$ indicates the viscous friction coefficient. This model provides a good approximation for friction in a wide range of the engineering applications with dissimilar operating environments. It makes the correct assumption that the true contact occurs at points where the elastic bristles of the contact surface come together. This assumption agrees with the observations

found in the tribology of engineering surfaces.

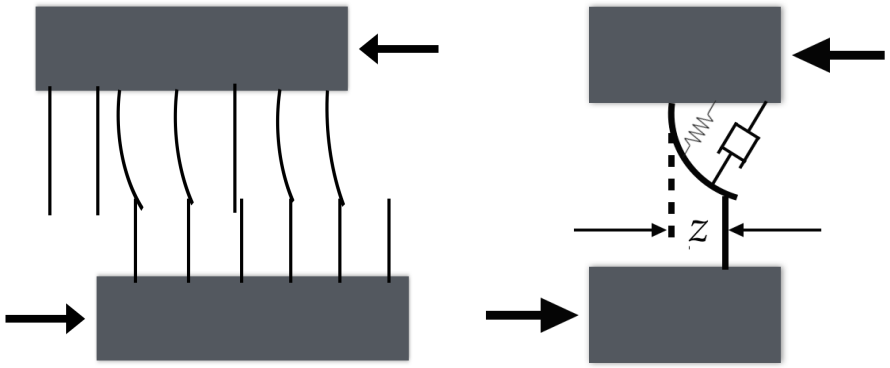


Figure 1.8: (a) Contact area between two solid bodies is thought of as a contact between bristles. (b) The average deflection of the bristles between the contact area is represented by a single bristle with the average deflection $z$.

For the object experiencing constant velocities, the steady-state friction denoted by $F_{ss}$ associated with the velocities is given by

$$\begin{aligned} F_{ss}(v) &= g(v)\, sgn(v) + \sigma_2 v \\ &= F_c sgn(v) + (F_s - F_c)\, e^{-(v/v_s)^2} sgn(v) + \sigma_2 v \end{aligned} \tag{1.8}$$

Equation (1.8) characterizes the famous Stribeck curves [38] which models friction as a function of velocity, see Fig. 1.9. The Stribeck curve experimentally obtained provides us an insight into the smooth transition between static friction and sliding friction instead of having a discontinuous drop once the object is at the onset of motion. The Stribeck velocity $v_s$ in Equation (1.6) determines the slope of the friction curve during the transition period.

#### 1.2.2.5 Numerical Accuracy of Various Friction Models

Friction is a highly nonlinear resistance for a system. The reliable predictions of the studied system dynamics demand accurate friction models. A control system implemented based on an inaccurate friction model may lead to inaccuracy or even

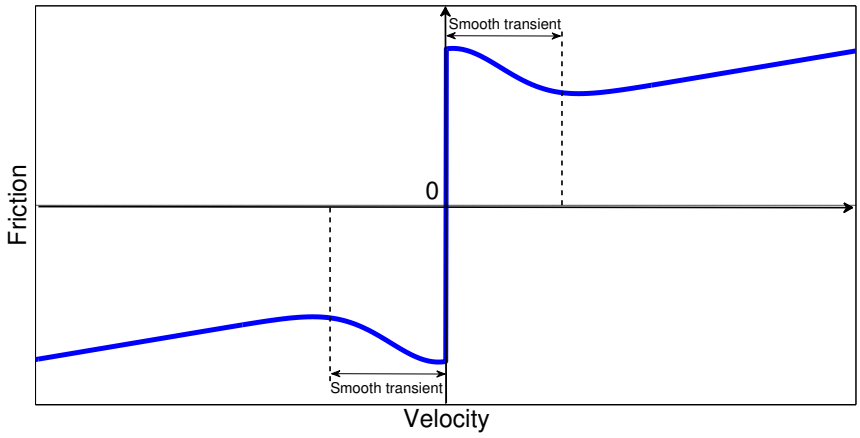


Figure 1.9: Stribeck curve characterizes friction as a function of velocity.

instability. As a result, selecting a friction model in which most of the typical friction features are included is crucial in order to have a good accuracy.

Several simple but fundamental mechanical systems, such as spring-mass system or servo motor, were used in [37, 39–44] as a platform to simulate the key features of friction produced by the friction models of interest. However, the numerical results obtained from various models were not verified by the experimental results. It remains unclear whether all these models can yield simulation results similar to the experimental friction behaviours.

The experimental presliding data were compared with the numerical results yielded by a LuGre-inspired model proposed in [45], using a robot arm. The comparison confirmed that the proposed model was a good approximation of the presliding. However, the ability of the proposed model to account for more dynamic features surveyed in Section 1.2.1 was not demonstrated in the work. The model may not suffice when it comes to producing these unexamined features. Reference [16] and [24] were suffered from the same shortage where only one friction feature was experimentally verified in their works.

In general, all the features surveyed in Section 1.2.1 should be simulated by the models presented in Section 1.2.2. Afterwards, the numerical features produced by various models should be compared with the features experimentally observed. Such

a comparison helps select an accurate friction model for this study. No literature references are known to accomplish this challenging task.

### 1.2.3 Experimental Setups

#### 1.2.3.1 Friction Oscillator

A typical and popular experimental setup used to explore the friction characteristics based on the translational motion is a friction oscillator. Such a rig was originally designed by Liew [46] and was further improved by other researchers [1, 25, 26] over time. Fig. 1.10a shows latest variation of the friction oscillator. Such a rig can be significantly simplified as shown in Fig. 1.10b, and the dynamics of the simplification can be expressed by the following second-order differential equation:

$$(M + m_t)\,\ddot{y} = -2k\,[y - e\,(t)] - c\,[\dot{y} - \dot{e}\,(t)] - F_f \tag{1.9}$$

where all the system parameters, $M, m_t, k$, and $c$, are defined and experimentally identified in [26]. During the experiments, various forms of displacement profiles are provided to the vibrating base where the effect of the oscillation amplitudes/frequencies on the friction behaviours can be studied. The relative displacement $y - e\,(t)$ and relative velocity $\dot{y} - \dot{e}\,(t)$ are measured by the linear velocity and displacement transducer (LVDT) and linear velocity transducer (LVT), respectively. The acceleration, $\ddot{y}$, is sensed by the accelerometer. The friction $F_f$ can be determined based on the experimental data and the dynamic equation (1.9) at each sampling time. Nevertheless, the friction oscillator usually incorporates many mechanical components as shown in Fig. 1.10, which makes it time-consuming to perform the assembly and the calibration.

#### 1.2.3.2 DC motor

DC motor is another popular device to study the friction induced by rotary motion [2, 31, 47–49]. Normally a DC motor is integrated with a gear head as shown in Fig. 1.11a. The gear head is used to vary the speed/torque ratio between the input

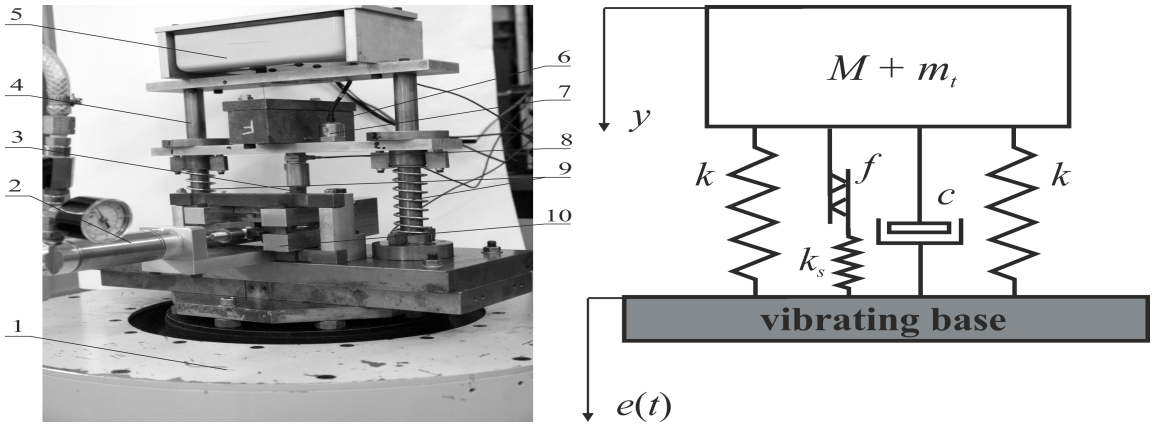


(a) (b)

Figure 1.10: (a) General view of the friction oscillator proposed in [1]. 1-shaker; 2-pneumatic actuator; 3-friction tongue; 4-guiding post; 5-case of LVT and LVDT; 6-mass; 7-accelerometer; 8-force transducer; 9-coil springs; 10-clamping device. (b) Simplified model of the friction oscillator [1].

shaft and the output shaft, which enables the motor to reach high torque/velocity level at reasonable cost based on the applications. In addition, it is easy to implement precise position/velocity control on DC motors, which benefits the investigation into friction features since some features will be seen only when the controlled object is oscillating within a predetermined velocity range (velocity control) or the applied force is varying in a specific fashion (force control). Figure 1.11b shows a typical static friction-velocity map experimentally obtained from the DC motor [2]. Such a map can be produced by most of the commercially available DC motors, and is valuable for parameter identification for various models and further friction modelling. In summary, friction modelling and compensations with DC motors have recently received a great deal of attention from a number of researchers due to the rapid development of electric motor and drive industry. However, friction is generally a combined result of various factors such as material of frictional surfaces and type of lubricant added into the moving surfaces. The frictional surfaces of the DC motors are usually in a sealed environment, which does not allow the factors influencing friction to be easily altered. This limitation makes the DC motors less useful if changeable contact conditions are of great importance.

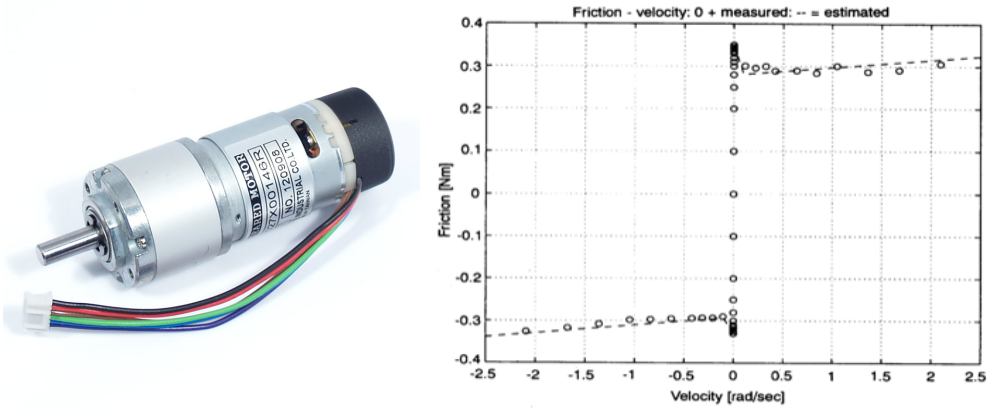


(a) (b)

Figure 1.11: (a) Typical DC motor with encoder and gear head. (b) Friction versus velocity [2].

#### 1.2.3.3 Self-excited System

Self-excited system represented schematically in Fig. 1.12a is frequently used to study a friction-induced phenomenon named as stick-slip oscillation [3, 22, 50, 51]. Such an oscillation caused by the friction is responsible for unpredictable system behaviors in many industrial applications and indeed worth a full understanding. A self-excited system represented in Fig. 1.12a shows a mass block $m$ that is moving on the belt along the horizontal direction subject to one spring and the frictional surface. During the experimental trial, the block is moved toward right then slip back to left due to the growing force arisen from the pulled spring. The block will be toward right again once the pulling force is lower than the static friction, and this back-and-forth motion is repeating indefinitely with a moving belt. Such an oscillation in motion is attributed to the rapid transient between static and Coulomb friction, and a good understanding of which may help elimination of its effects. The phase portrait, shown in Fig. 1.12b, having $x_1$ and $x_2$ as coordinates was presented in [3] where several standard techniques were applied to analyze this interesting dynamical nonlinear behaviours of friction. Please note that $x_1$ is defined as the displacement where its derivative is $x_2$. The modelling of this self-excited system including the friction was carried out, and the effect of various belt driving velocities on the am-

plitude/frequency of the oscillation was experimentally explored and verified by the numerical results. This particular setup was designed back in the 1950's but still remains active nowadays. Although this setup was well-established by the later improvement, none of the improved variations has been reported able to control the force loaded on the mass block. As a result, the investigation of some friction behaviours induced by controlled loading force can not be carried out. In addition, the micrometer-level displacement due to the plastic deformation of asperities under the load in the presliding regime [10] can not be measured using this setup because of the lack of the proper displacement sensors.

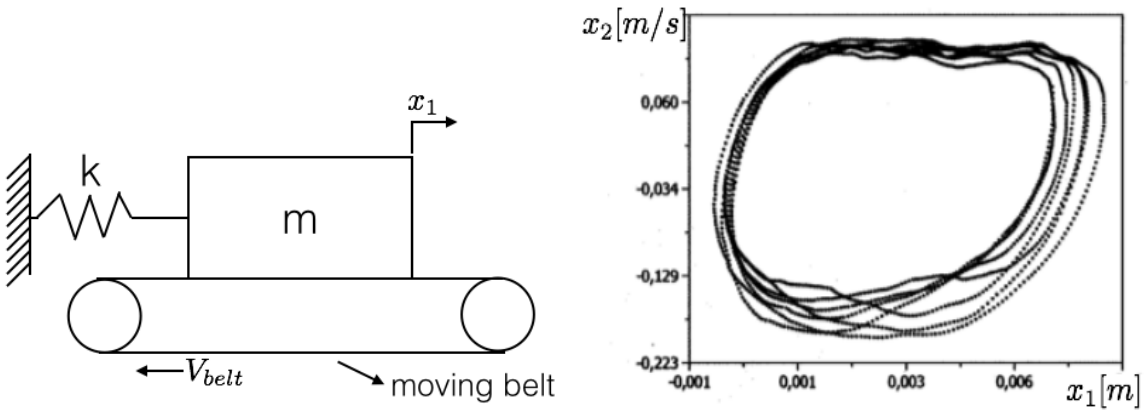


(a) (b)

Figure 1.12: (a) Self-excited system model. (b) Phase portrait of mass block [3].

### 1.2.4 Stability Analysis of Systems with Friction

Stability of systems with several existing friction models has long been studied. The parametric perturbations within the friction models are unavoidable and can vary the qualitative behaviour of the system. A single mass system subject to classical friction model was used to numerically illustrate the effect of various $r$ values on the systems' qualitative behaviour in [4]. Note that $r$ represents the level of the static friction $F_s$ with respect to the Coulomb friction $F_c$, i.e., $r = \frac{F_s}{F_c}$. Figure 1.13 shows the state trajectories of the studied single mass system subject to a PID controller, and the definition of the states are presented in Tab. 1.1. The two trajectories are

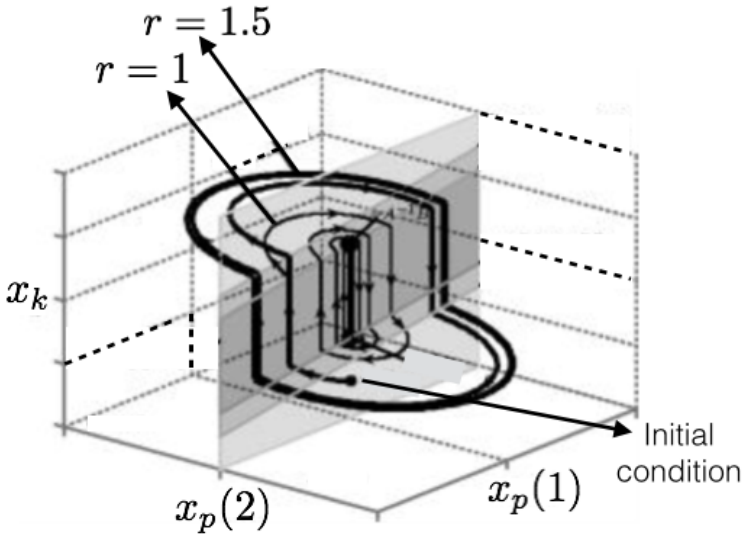


Figure 1.13: State trajectory of single mass system with position PID control [4].

generated from the same initial condition, the thin line and the thick line represent $r = 1$ and $r = 1.5$, respectively. Figure 1.13 shows that the perturbed parameter $r$ has a significant effect on the system dynamic as the state trajectories behave so different. In addition to that, the sufficient conditions on point-wise global stability are given in reference [4]. Such conditions should be considered in the design stage of the controllers for similar systems to ensure the asymptotic stability and avoid undesired system outputs.

Table 1.1: Definition of states for the signal mass system with position PID control.

| State | Definition |
|---|---|
| $x_p(1)$ | Tracking error |
| $x_p(2)$ | Velocity of the mass |
| $x_k$ | Time integral of the tracking error |

The servomechanism device shown in Fig. 1.14 was designed to conduct the stability analysis in reference [5], the block diagram along with the PD controller and the friction compensation is presented in Fig. 1.15a. The authors were interested in how the slight mismatch between the true plant Coulomb friction, $T_c$, and the mod-

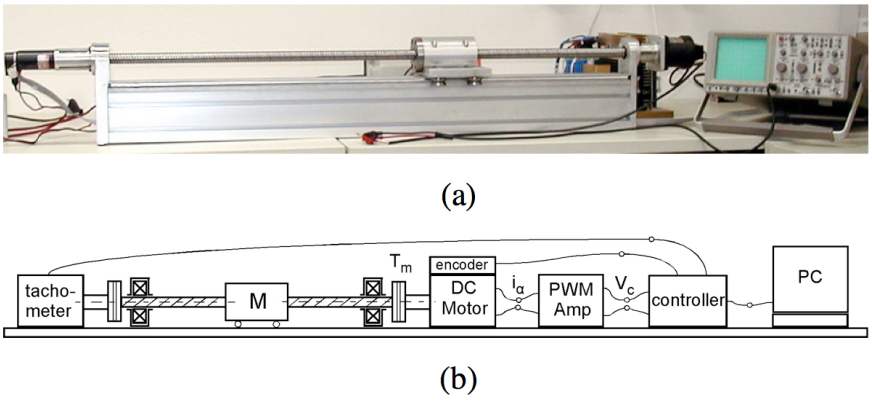


Figure 1.14: General view of experimental rig [5].

elled Coulomb friction taken in the friction compensation, $\hat{T}_c$, affected the systems' qualitative behaviour. In addition, the effect of the mismatch between the true plant viscous friction coefficient, $b$, and the theoretical viscous friction coefficient in friction compensation, $\hat{b}$, on the systems' qualitative behaviour was studied as well. Describing function analysis (DFA) [52], generally agreed upon as being the most practically useful tool for dynamic system analysis, was employed to derive the conditions responsible for limit cycle generation of the studied system. The limit cycle generation map is given in Fig. 1.15b where $\Delta T_c = T_c - \hat{T}_c$, $\Delta b = b - \hat{b}$, $K_{amp}$ is motor amplifier gain, $K_T$ is torque constant and $P$ is a function defined in [5]. A limit cycle in the phase plane analysis is defined as an isolated closed curve, indicating that the each system state displays a sustained oscillation of fixed amplitude and period and the stable limit cycle attracts/repels the nearby trajectories. The map presented in Fig. 1.15b is fundamental but valuable for control engineers when working with this specific setup as the map predicts the occurrence of limit cycles. Limit cycles can be either undesirable or desirable in engineering applications, and a good understanding of limit cycles is required in order to manipulate them as a tool.

Besides the above articles, a number of other articles have been published that relate to the stability analysis for a inclined-spring system subject to constant-velocity sliding [6, 8]. Figure 1.16 shows such a system in which the friction at the contact surfaces was modelled by taking the spring constant $k$ and the spring angle $\Psi$ with

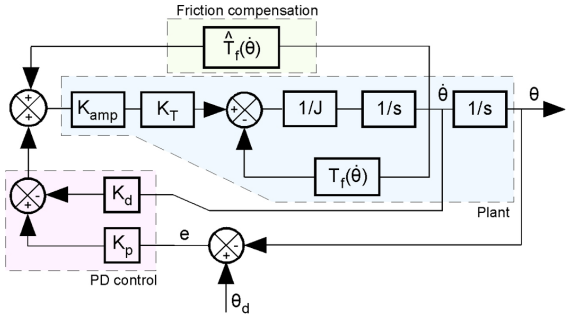


(a)

| | $\Delta b > 0$ | $\Delta b < 0$ |
|---|---|---|
| $\Delta T_C > 0$ | Never | If $0 < K_d < -\frac{\Delta b}{K_{amp} K_T}$ |
| $\Delta T_C < 0$ | If $0 < P < -2\Delta T_C$ | If $\begin{cases} 0 < P < -2\Delta T_C \\ K_d > -\frac{\Delta b}{K_{amp} K_T} > 0 \end{cases}$ or if $\begin{cases} P > -2\Delta T_C > 0 \\ 0 < K_d < -\frac{\Delta b}{K_{amp} K_T} \end{cases}$ |

(b)

Figure 1.15: (a) Block diagram of system with friction compensation and PD control [5]. (b) Limit cycle generation map [5].

respect to the ground into consideration. The mass block $m$ is pulled by the spring at the velocity $v_0$ while the block slides at the velocity $v$, the spring constant $k$ and the spring angle $\Psi$ directly determine the normal force $\sigma_0$. Several numerical trials associated with various $k$ values subject to the same initial condition are simulated in [6, 8] where the trial featuring the largest $k$ value converges to the equilibrium point faster than other trials. As they decrease the $k$ value to the critical spring constant $k_{cr}$, the state trajectory begins to show a sustained circle on the phase plane and neither converge to the origin nor diverge to infinity. The system becomes unstable once the $k$ is smaller than the $k_{cr}$. In addition, the state trajectories corresponding to various $\Psi$ values are simulated in which the authors discovered that the negative spring angle can make the state trajectory converge to the equilibrium point faster than other trials.

References [4, 5] focused on stability analysis for control systems in which the static friction models are used to represent the friction. Thus, it is unclear that the stability results obtained from the static models can be directly applied to the real systems where the dynamic friction features occur. A dynamic friction model proposed in [53] was taken to carry out the stability analysis in [6, 8]. Such a model takes a state variable $\theta$ to model the effect of sudden change in normal force of the studied object on the friction. However, in many industrial applications, the dynamic features of friction are associated with the change in velocity or loading force. The

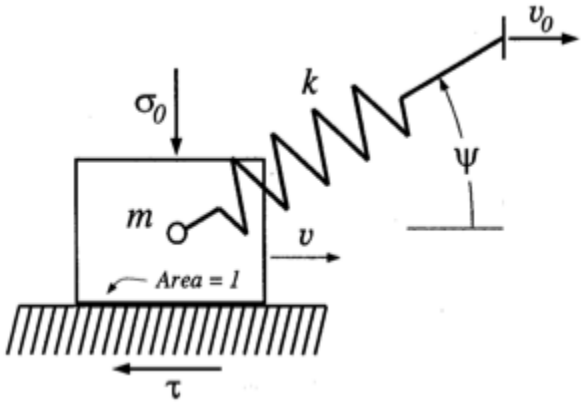


Figure 1.16: Inclined-spring model [6].

model proposed in [53] did not take these factors into consideration in the development of the model, therefore, a more realistic friction model is expected in [6, 8] in order to have a better numerical accuracy.

## 1.3 Thesis Objectives and Methodology

The objectives of this thesis is to provide insights into the effect of parametric uncertainties within a realistic friction model on the control system stability. Towards this goal, three major tasks should be carried out, listed as follows:

- A versatile experimental setup needs to be designed and fabricated to carry out a wide range of experimental analysis. The design choice should be based on the criteria of simplicity of the setup design and flexibility in terms of contact condition changes such as the lubricants and the materials of the contact junction. Last but not least, the setup should be able to demonstrate all the features surveyed in Section 1.2.1 in which several control tasks need to be implemented.

- The fabricated experimental setup should be used to parameterize all the friction models included in Section 1.2.2. All the parameterized models are then validated by the consistency of friction features in experiments and simulations. The friction model which simulates all the features of friction with best accuracy

will be employed to represent the friction of the proposed setup.

- Two set-point controllers are synthesized based on the proposed setup state space model in which the friction is modelled by the most accurate model determined in last task. The parameters of interest in the friction model will be perturbed with respect to their nominal values to study the stability of the two control systems.

## 1.4 Organization of Thesis

The core of this thesis is organized into three chapters. A description of each is outlined below:

**Chapter 2** presents the proposed experimental setup including the mechanical structure, sensing system and experimental procedure. The parameter identifications for the chosen friction models are carried out by the proposed setup that is used to experimentally produce the friction features of interest. The simulated features from the friction models are then compared with the experimental features to judge the accuracy of the models. The relation between the chosen friction models and their numerical feature predictions is investigated and discussed. Such a discussion helps us select the most realistic friction model which is taken to model the friction for our setup.

**Chapter 3** makes efforts to explore the effect of the perturbed friction-related parameters on the stability of the proposed setup. Two set-point controllers are synthesized based on the state-space model of our setup in which the friction is modelled by the most realistic model among the selection in last chapter. The parameters of interested are then perturbed around the nominal values for each control system, and the stability regions associated with two control systems demonstrate the effect of the perturbations subject to the proposed setup.

**Chapter 4** presents the concluding remarks of this thesis and sketches some recommended future work.

# Chapter 2

# Development of One-dimensional Sliding Block Experimental Setup

## 2.1 Introduction

In the previous chapter, part of the content was devoted to review a number of common friction features and friction models. However, the accuracy of each model in our selection with respect to the reviewed features still requires further investigation which involves comparison between the simulated features and the experimental features. A realistic friction model is expected to show a good agreement with the experimental data.

In this chapter, an experimental setup is presented to provide dynamic friction data that would allow us to parameterize the friction models and record the friction features, the advantage of which lies in simplicity in design and flexibility in terms of contact conditions changing. The design, sensing system and the friction estimation procedure of the setup are provided in this chapter. The numerical friction features simulated by the parameterized friction models are compared with those obtained via the proposed setup. The discrepancies between the experimental features and the numerical model predictions help researchers to judge the accuracy of the models. The relation between the candidate model structures and their numerical friction feature predictions is investigated and discussed. A summary describing how to select the

most optimal friction model among a variety of engineering applications is presented at the end of this chapter. The most realistic friction model will be used to formulate the state space equation of our setup in which the parameters are perturbed for stability analysis conducted in Chapter 3.

## 2.2 Approach

### 2.2.1 Setup Design

The experimental table shown in Fig. 2.1 mainly consists of a ball screw, a motor and a brass block. The ball screw is coupled with the motor shaft by a beam coupler. One optical encoder is used to provide information about the motion of the shaft. A thin metal plate is bolted to the ball screw nut to transfer the longitudinal motion to the brass block. The load cell, with male thread studs, provides a rigid connection between the thin metal plate and the brass block. The micrometer head is used to calibrate the dedicated high-sensitivity sensor which is required in the measurement of presliding. Detailed information on the design, working principle, installation, sensitivity and calibration of such a sensor are addressed in Section 2.2.2.

The rotary motion of the shaft is transferred to the ball screw shaft via the beam coupler. The resultant rotary motion of the shaft moves the ball screw nut linearly along the longitudinal axis. The high stiffness of the metal plate and the load cell ensures that one dimensional sliding motion is accurately reproduced on the brass block. The load cell is used to continuously measure either the tension or the compression force applied on the brass block. An optical encoder is used to measure the linear displacement of the mass, which is used in the upcoming analysis as discussed in Section 2.2.3. Such an encoder generates up/down pulses with a resolution of 512 count per revolution. Table 2.1 summarizes the electrical/mechanical parameters of the developed experiment table.

Figure 2.2 demonstrates how the setup interacts with the PC, servo motor amplifier and the Quanser data acquisition (DAQ). The encoder measurements and the load cell data are collected by the Quanser DAQ and transmitted into the PC at

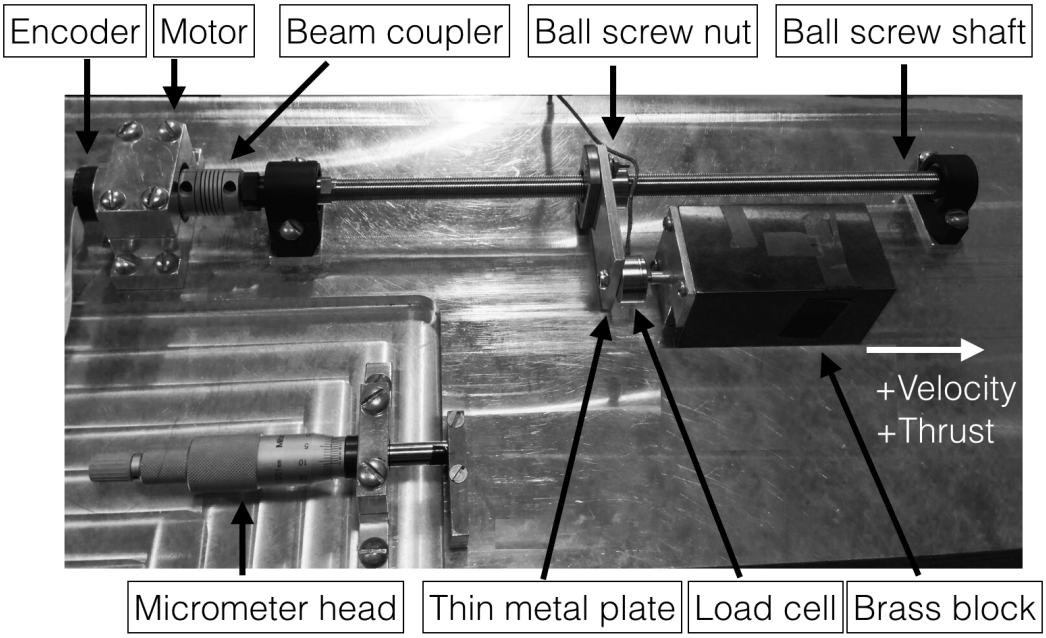


Figure 2.1: Photo of sliding table.

200 $Hz$. The PC is manufactured by Dell, which features a dual-core processor with a clock speed of 2.40 GHz and 4 GB of Ram. The controllers programmed within the Matlab Simulink environment generate the control voltage to the motor based on the tracking error. The amplifier, Maxon ADS/50-5, bridges the controller voltage commands sent from the PC to the motor installed on the experimental setup.

Measurements of the microfine displacement of the block occurring before the gross sliding has posed a well-known challenge to any encoder-based displacement sensing system. Such a displacement, alternatively named presliding, is essential to the identification procedure of the LuGre model and is typically on the scale of a few micrometers. To record the presliding of the block, a capacitance displacement sensor featuring high sensitivity is designed and built. The detailed information of the displacement sensor is addressed in Section 2.2.2.

Table 2.1: Parameters of motor, ball screw and load cell

| Symbol and name | Nominal value | Unit | Equipment |
|---|---|---|---|
| $m_{motor}$, weight of motor | 71 | g | |
| $R$, terminal resistance | 21.4 | Ω | |
| $L$, terminal inductance | 0.953 | mH | |
| $K_m$, torque constant | 37.4 | mNm/A | |
| $K_v$, speed constant | 255.0 | rpm/V | Motor |
| $J_m$, rotor inertia | 4.2 | gcm$^2$ | |
| $V_{nominal}$, nominal voltage | 36.0 | V | |
| $P$, assigned output power | 11.0 | W | |
| $\eta_m$, max. efficiency at nominal voltage | 83 | % | |
| Screw shaft diameter | 10 | mm | |
| Lead | 1 | mm | |
| Thread direction | Right | | ball screw |
| Screw thread length | 262 | mm | |
| Total length | 310 | mm | |
| Excitation | 5 | V | |
| Output | 2 | mV/V | |
| Capacity | 44.5 | N | Load cell |
| Resolution | 0.089 | N | |
| Safe overload | 66.75 | N | |
| Ultimate overload | 133.5 | N | |
| Weight | 1 | kg | Brass block |

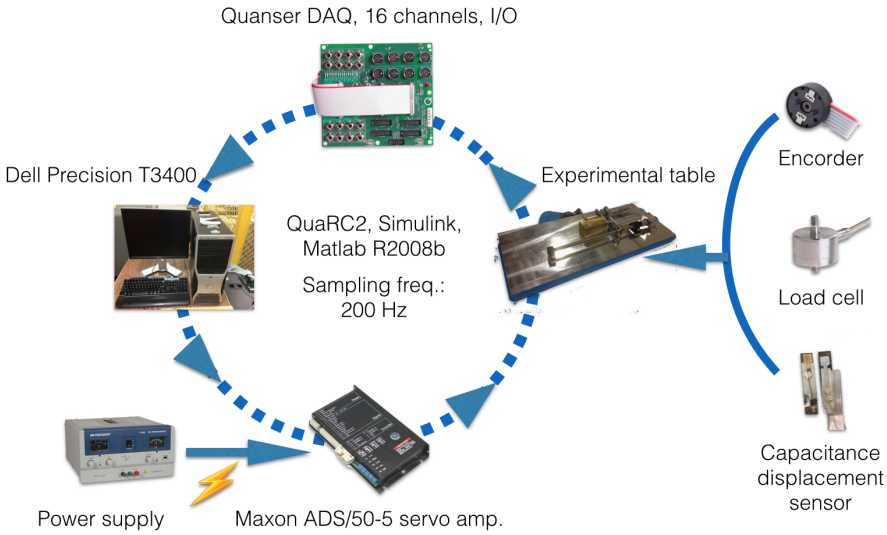


Figure 2.2: Control loop, power source and the sensing system.

### 2.2.2 Design of Capacitance Displacement Sensor

Measuring the presliding necessitates a capacitance displacement sensor, which is introduced in this section. The measurements are used to determine $\sigma_0$ and $\sigma_1$ presented in Eqn. (1.7). Figure 2.3a shows all components included in the sensor, which consists of two conducting plates. Each conducting plate is fabricated by depositing a thin layer of aluminum on one piece of glass slide using the sputtering system. The stencil mask helps define the pattern of the conducting plate. Placing two conducting plates in parallel forms a capacitor. The resultant capacitance varies with the separation between two plates if the overlap area and the background capacitance remain unchanged.

Figure 2.3b shows how the capacitance measurements are transmitted to the Simulink environment. The capacitance arisen from the two conducting plates are converted to the digital signal and sent to the Matlab Simulink. Figure 2.4a depicts the installation of two conducting plates. Conducting plate 1 is attached on aluminum plate 1 bolted to the the spindle. Conducting plate 2 is attached on aluminum plate 2 bolted to the brass block. The two conducting plates are positioned and aligned in a way that its separation gives measurable capacitance, and that the edges of the two square plates are precisely aligned to form a overlap area.

The displacement measured by the sensor consist of two parts. The first part is the true presliding occurring at the contact junction, and the second part comes from the elastic deformation of the material of the brass block due to the applied force. To reduce the displacement of the second part, the capacitance displacement sensor is installed at the bottom of the brass block with a clearance of $2mm$ with respect to the table, as shown in Fig. 2.4b. In this case, the presliding will dominate the sensor reading since it is measured where close to the frictional surface. Figure 2.4c depicts a typical configuration of the sensor. The capacitance caused by such a parallel-plate capacitor has the form of

$$C = \frac{\varepsilon A}{x} \tag{2.1}$$

where $\varepsilon$ is the permittivity of air, normally $8.854 \times 10^{-12}\, F/m$ is used, $A$ is the overlap

area of the two plates, and $x$ is their separation.

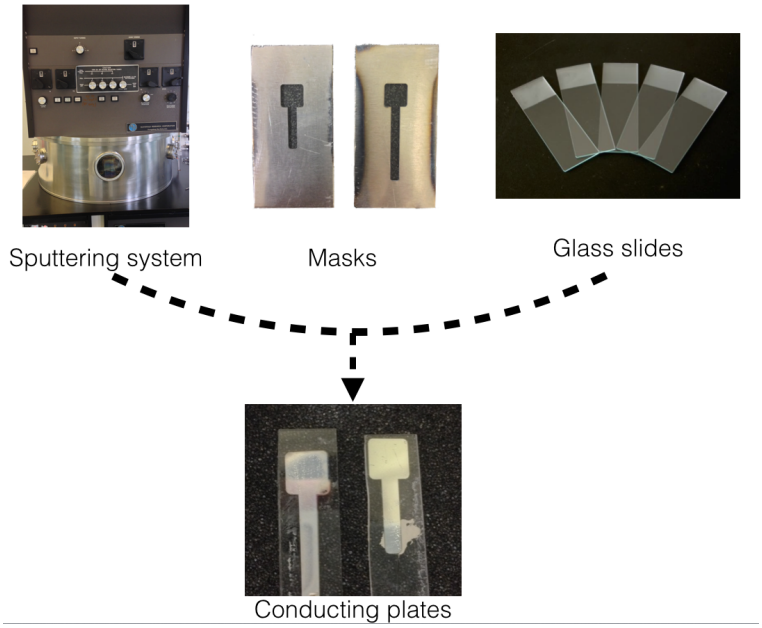


(a)

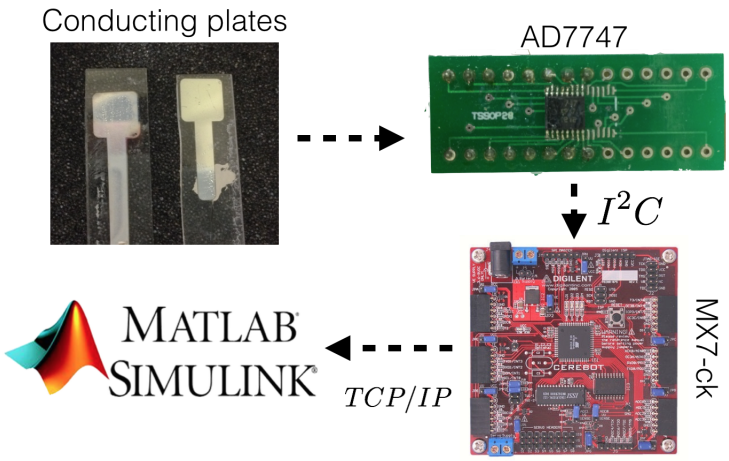


(b)

Figure 2.3: (a) Tools to build the sensor. (b) Transmission of measurement data to Simulink environment. AD7747 helps convert the analog capacitance signal to digital, and MX7-ck board transmits the digital signal to Matlab.

The sensitivity, $S$, of this capacitance displacement sensor is defined as the ratio

of the change in capacitance with respect to the displacement as

$$S = \frac{dC}{dx} = -\frac{\varepsilon A}{x^2} \tag{2.2}$$

where the sensitivity increases for low $x$ that consists of the initial separation and the displacement. This favorable feature makes the capacitance displacement sensor popular in the application of precise position sensing.

Figure 2.5 shows typical calibration results on the capacitance sensor used in this thesis. All the capacitance measurements are sampled at various displacements having the equal interval of $10\mu m$ in between. A quadratic polynomial is used to relate the displacements and the corresponding average capacitances. Such a calibration needs to be carried out for each trial since the initial separation varies from trial to trial. The calibration can be done as follows:

## Capacitance displacement sensor calibration:

1. Bring the brass block to a position close to the spindle of the micrometer head. Turn on the capacitance displacement sensor. Start the data acquisition system.

2. Fine-tune the position of the spindle to ensure that the initial separation of two plates is minimized. Confirm the two conducting plates are precisely overlapped. Once the initial separation is determined, the corresponding capacitance is recorded as $C_{ini}$.

3. Rotate the thimble to move conducting plate 1, shown in Fig. 2.4a, away from conducting plate 2 by $10\mu m$ increments until $70\mu m$ of accumulated displacement is achieved, and the capacitance in response to each displacement is recorded.

4. Establish the relationship between the displacement and the capacitance. A quadratic polynomial is recommended to best fit to all recorded points plotted on the displacement-capacitance map.

Once the calibration is properly performed, we move the spindle back to the initial position where the $C_{ini}$ is observed. The quadratic polynomial obtained in the calibration process is valid for the trial having the same $C_{ini}$ value.

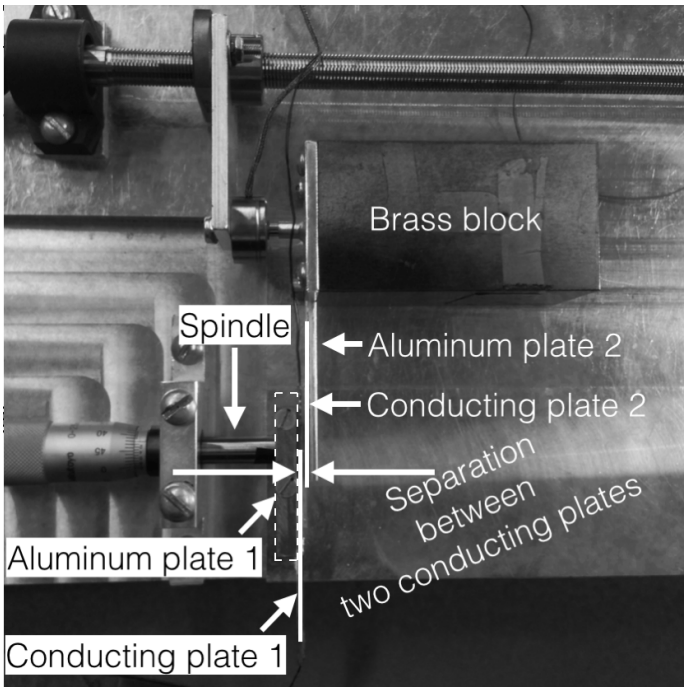


(a)

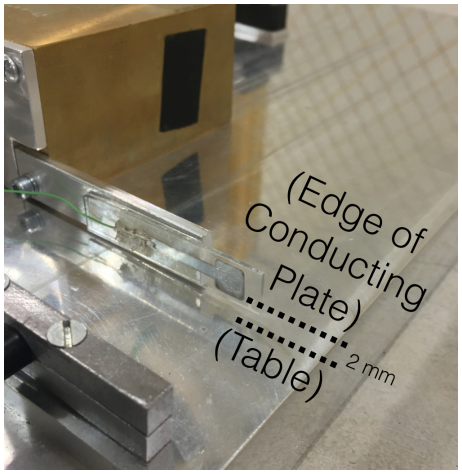


(b)

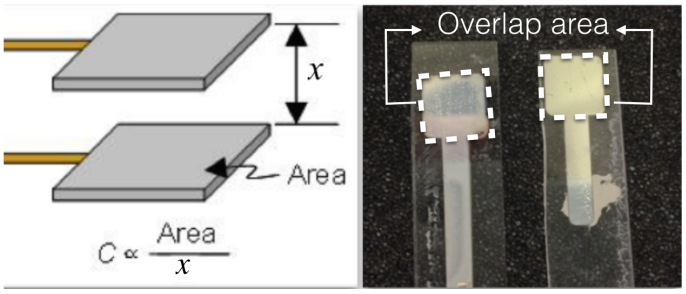


(c)

Figure 2.4: (a) Installation of two conducting plates. (b) Vertical clearance between the table surface and the conducting plate edge. (C)Left: schematic and notations for a parallel-plate capacitor. Right: two square conducting plates with a square overlap area are used to form the capacitor.

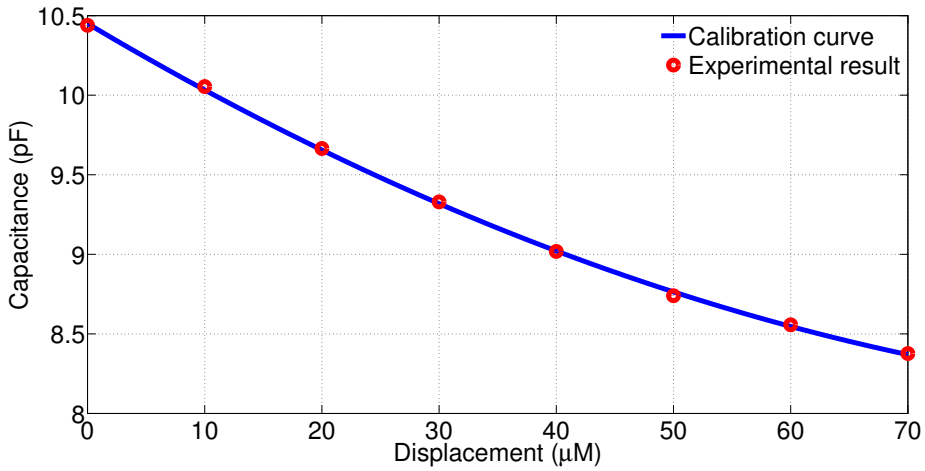


Figure 2.5: Calibration curve versus experimental measurements.

### 2.2.3 Friction Estimation

The friction force between the brass block and the aluminium table, as shown in Fig. 2.6, is estimated to identify the parameters of the selected friction models and to demonstrate various features of friction. For each experimental trial, the procedures outlined below are strictly followed to ensure the friction to be accurately estimated.

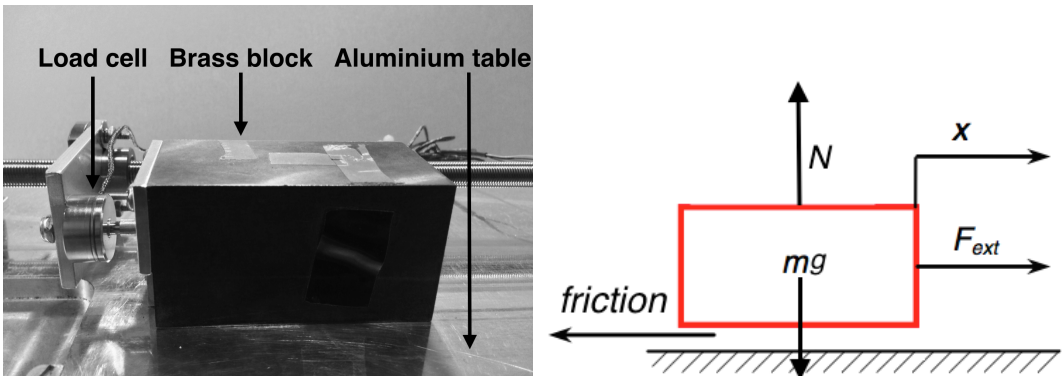


(a) (b)

Figure 2.6: (a) Close-up view of the brass block and the aluminium table under. (b)Schematic of the sliding block subject to friction.

All the trials in this study are performed from rest, i.e., the force applied on the block and the displacement are null before we launch each trial. The following procedure ensures null force is achievable. The brass block is positioned where the

ball screw nut has equal travel to both ends of the shaft. This adjustment ensures that the back and forth motion required for some identification processes can be achieved. After the ball screw nut is in position, we manually zero the force applied on the block by rotating the ball screw shaft. The incremental encoder used in this study provides the relative angle between the origin and the current position of the motor shaft. The origin is the position of the motor shaft when the power is turned on. The control tasks are implemented once null force and displacement are secured.

The dynamics of the brass block in Fig. 2.6 can be described by Newton's second law:

$$F_{ext} - friction = m\ddot{x} \tag{2.3}$$

where the $F_{ext}$ is the input force, $m$ is the mass of the block, and $\ddot{x}$ indicates the acceleration of the block. The friction can be determined from experimental $F_{ext}$ and $\ddot{x}$ data.

Angular displacement of the motor, $\Delta\theta$, is converted to the linear displacement of the block using

$$\Delta x = \frac{1}{2\pi p}\Delta\theta \tag{2.4}$$

where $p$ indicates the pitch of the ball screw, $\Delta\theta$ is the rotational displacement of the lead screw shaft in radians, $\Delta x$ represents the linear displacement of the brass block. The second derivative of the displacement of the mass with respect to time yields the acceleration in Eqn. (2.3). The input force sensed by the load cell and the linear displacement is filtered by a second order low-pass filter. Friction estimation at each time instance is achievable using Eqn. (2.3). So far, a valid procedure is proposed to estimate the friction for conducted trials. The following subsections summarize the reference inputs, controlled variables and the post-processing procedures needed to identify the parameters for the models.

## 2.3 Parameter Identification

### 2.3.1 Classical Model

#### 2.3.1.1 Procedure

Three parameters, $F_s$, $F_c$, and $\sigma_2$, included in Eqn. (1.1) are determined through the Stribeck curve where the break-away force, Coulomb friction and viscous friction coefficient can be clearly observed. The first step is to estimate the friction during constant velocity motion. An experimental test is performed for fifteen trials at dissimilar desired velocities ranging from $v = \pm 2.0\, mm/s$ to $\pm 5.5\, mm/s$ with the equal interval of $0.5\, mm/s$. A PID controller regulates the velocity output and operates on tracking error. During the steady state the friction is therefore equal to the force applied to the block due to the null acceleration. The mean values of the friction profiles, measured for various velocities, are plotted on a friction-velocity map which partially constructs the Stribeck curve.

The second step is to explore the highest load before the dynamic motion of the block is triggered. Thirteen trials are performed by assigning the desired input force to a closed-loop force PID controller. Desired forces for the trials are listed in Table 2.2. Plotting the experimental points on the friction-velocity map completes the the Stribeck curve and the function Eqn. (1.8) is used to perform the curve fitting.

The curve fitting toolbox in Matlab is used to fit the data for Eqn. (1.8). The selected method and algorithm are NonlinearLeastSquares and Trust-Region, respectively. Other options are left with the default settings. The identified parameters for positive and negative velocity regions are averaged to obtain the nominal parameters. This post-processing ensures the model predictions to be symmetrical in both regions of velocities. Note that the parameter $V_s$ in Eq. (1.8) is not applicable to the Classical model.

#### 2.3.1.2 Results

The experimental trials associated with static and dynamic motion are plotted on the friction-velocity map to create the Stribeck curve. As can be seen in Fig. 2.7,

Table 2.2: Desired step input force values for classical model parameter identification.

| Trial No. | Desired force [N] | Trial No. | Desired force [N] |
|---|---|---|---|
| 1 | 0.3 | 8 | 2.2 |
| 2 | 0.6 | 9 | -0.3 |
| 3 | 1.0 | 10 | -0.6 |
| 4 | 1.5 | 11 | -2.1 |
| 5 | 1.8 | 12 | -2.3 |
| 6 | 2.0 | 13 | -2.4 |
| 7 | 2.1 | | |

the points collected from the trials with static motions distribute vertically on the y-axis. It indicates that the brass block remains static if the applied force is in the interval of $[-2.4, 2.2]$ $N$. In addition, the friction data collected from the trials with nonzero velocities show a rate-dependent behaviour. Overall, the higher the velocity, the larger the friction.

Following the procedure presented in Section 2.3.1.1, the parameters are identified and shown in Table 2.3. Such parameters are taken to reproduce the friction for the classical model which is drawn in the solid curve in Fig. 2.7. The experimental measurements and the predictions produced by Eqn. (1.1) are superimposed and agree well, indicating Eqn. (1.1) realistically represents the experimental friction.

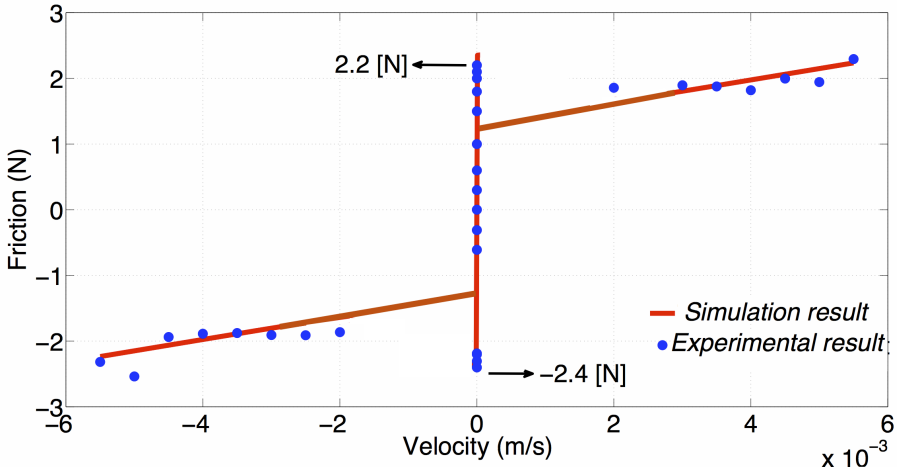


Figure 2.7: Friction-velocity map: experimental findings and classical model output.

Table 2.3: Nominal model parameters for classical model.

| | Velocity | | | |
|---|---|---|---|---|
| Symbol and name | V> 0 | V< 0 | Nominal value | Unit |
| $F_c$, Coulomb friction | 1.11 | 1.458 | 1.284 | N |
| $F_s$, Static friction | 2.3 | 2.4 | 2.35 | N |
| $V_s$, Stribeck velocity | 0.001943 | 0.0003365 | 0.00113975 | m/s |
| $\sigma_2$, Viscous friction coefficient | 193.4 | 152.6 | 173 | N-s/m |

## 2.3.2 Dahl Model

### 2.3.2.1 Procedure

Two parameters, $\sigma$ and $F_c$ in Eqn. (1.2), are identified through sixteen trials. The desired sinusoidal velocity trajectories and durations of conducted trials are listed in Table 2.4. A PID controller regulates the velocity output and operates on tracking error. The frequency and duration for each trial are chosen to slide the block with either positive or negative velocity. The friction-displacement map resulting from each trial contributes to one set of parameters. The absolute peak of $1\,mm/s$ is adopted throughout all the trials. Slow motion and the sinusoidal reference input were also used by Dahl [29] to perform the identification process, whereas in his study the friction behaviour in rotary motion was of interest.

To obtain the friction model which is used to carry out the curve fitting, the Dahl model shown in Eqn. (1.2) with $sgn(v) = 1$ and $\alpha = 1$ [31, 33, 54–56] is integrated using the initial condition $F(x = 0) = 0$. It has the form of

$$F(x) = -F_c e^{\frac{-\sigma}{F_c}x} + F_c \tag{2.5}$$

Furthermore, $sgn(v) = -1$ gives

$$F(x) = F_c e^{\frac{\sigma}{F_c}x} - F_c \tag{2.6}$$

where $F$ and $x$ are friction force and displacement, respectively. Parameters, $F_c$ and $\sigma$, become identifiable with the friction-displacement maps experimentally recorded.

Table 2.4: Desired velocity trajectories for Dahl model parameter identification.

| Trial No. | Desired velocity trajectory $[m/s]$ | Duration $[Seconds]$ |
|---|---|---|
| 1 | $1 \times 10^{-3} sin\,(t)$ | 3.15 |
| 2 | $1 \times 10^{-3} sin\,(t)$ | 3.15 |
| 3 | $1 \times 10^{-3} sin\,(t/2)$ | 6.3 |
| 4 | $1 \times 10^{-3} sin\,(t/2)$ | 6.3 |
| 5 | $1 \times 10^{-3} sin\,(t/4)$ | 12.6 |
| 6 | $1 \times 10^{-3} sin\,(t/4)$ | 12.6 |
| 7 | $1 \times 10^{-3} sin\,(t/6)$ | 19 |
| 8 | $1 \times 10^{-3} sin\,(t/6)$ | 19 |
| 9 | $-1 \times 10^{-3} sin\,(t)$ | 3.15 |
| 10 | $-1 \times 10^{-3} sin\,(t)$ | 3.15 |
| 11 | $-1 \times 10^{-3} sin\,(t/2)$ | 6.3 |
| 12 | $-1 \times 10^{-3} sin\,(t/2)$ | 6.3 |
| 13 | $-1 \times 10^{-3} sin\,(t/4)$ | 12.6 |
| 14 | $-1 \times 10^{-3} sin\,(t/4)$ | 12.6 |
| 15 | $-1 \times 10^{-3} sin\,(t/6)$ | 19 |
| 16 | $-1 \times 10^{-3} sin\,(t/6)$ | 19 |

Selecting Eqn. (2.5) or (2.6) to perform the curve fitting depends on the sign of the velocity of the conducted trial. Trials $1-8$ correspond to Eqn. (2.5) and trials $9-16$ use Eqn. (2.6).

The least squares method is programed in a Matlab m-file for the purpose of finding the best fit to the experimental measurements. The output error cost function is defined as

$$E = \sum_{k=1}^{n} \left[F\left(k\right) - F\left(k, \sigma, F_c\right)\right]^2 \tag{2.7}$$

where $F\left(k\right)$ is the $k^{th}$ sampled friction measurement and $F\left(k, \sigma, F_c\right)$ is the $k^{th}$ value of model prediction given by either Eqn. (2.5) or (2.6). The parameters identified within the positive and negative velocity regions are averaged out to obtain the nominal parameters.

#### 2.3.2.2 Results

All the friction profiles estimated from the trials presented in Section 2.3.2.1 are plotted on the friction-displacement map to identify the parameters. Figure 2.8a and

Fig. 2.8b show a typical set of the velocity and the corresponding friction profiles out of 16 trials. Figure 2.8a shows that the velocity of the mass block follows the desired trajectory reasonably well. A minor fluctuation is found around the desired trajectory due to the tracking error occurring at each sampled time instant. It can be seen in Fig. 2.8b that the friction converges to a fixed value along with mild spikes once the block begins to move. Such spikes are attributed to varying velocities during operation.

Following the procedure presented in Section 2.3.2.1, the parameters are identified for each trial and shown in Table 2.5. Experimental results of Trial 7 is superimposed with the model prediction as shown in Fig. 2.8b. Overall, the model can capture the sliding friction except the spikes. Figure 2.8c zooms in Area 1 marked by dashed line in Fig. 2.8b. As can be seen that the model prediction monotonically approaches to a fixed value once a critical displacement is reached, which indicates that the break-away force can not be reproduced.

According to Table 2.5, each identified $F_c$ value does not have a significant variation with respect to the nominal $F_c$. The highest variation of approximately 13 % of the nominal value can be found in Trial 11. However, the identified $\sigma$ values are less clustered around the nominal value camparing with the $F_c$. This is due to the fact that the $\sigma$, coupled with an exponential function as shown in Eqn. (2.5) and (2.6), accounts for the change of the friction prediction with respect to the displacement during the transition period. It is numerically observed that a minor shift of the friction prediction during the transition period leads to a significant discrepancy in the $\sigma$. Thus a high standard deviation of the experimental results is expected in this parameter.

Figure 2.9 shows the descriptive error bars verifying whether the parameters fit within the normal range. According to [57] each experimental point is considered normal if it falls within two standard deviation(SD) of the mean. Any point falling outside this 2 SD boundary is treated as an abnormal point, which does not represent the typical behavior of the object to be measured/estimated. The standard deviation of $\sigma$ and $F_c$, calculated based on Table 2.5, are 18346.7 and 0.164, respectively. Each point shown in Fig. 2.9a indicates the $\sigma$ value independently identified in each trial

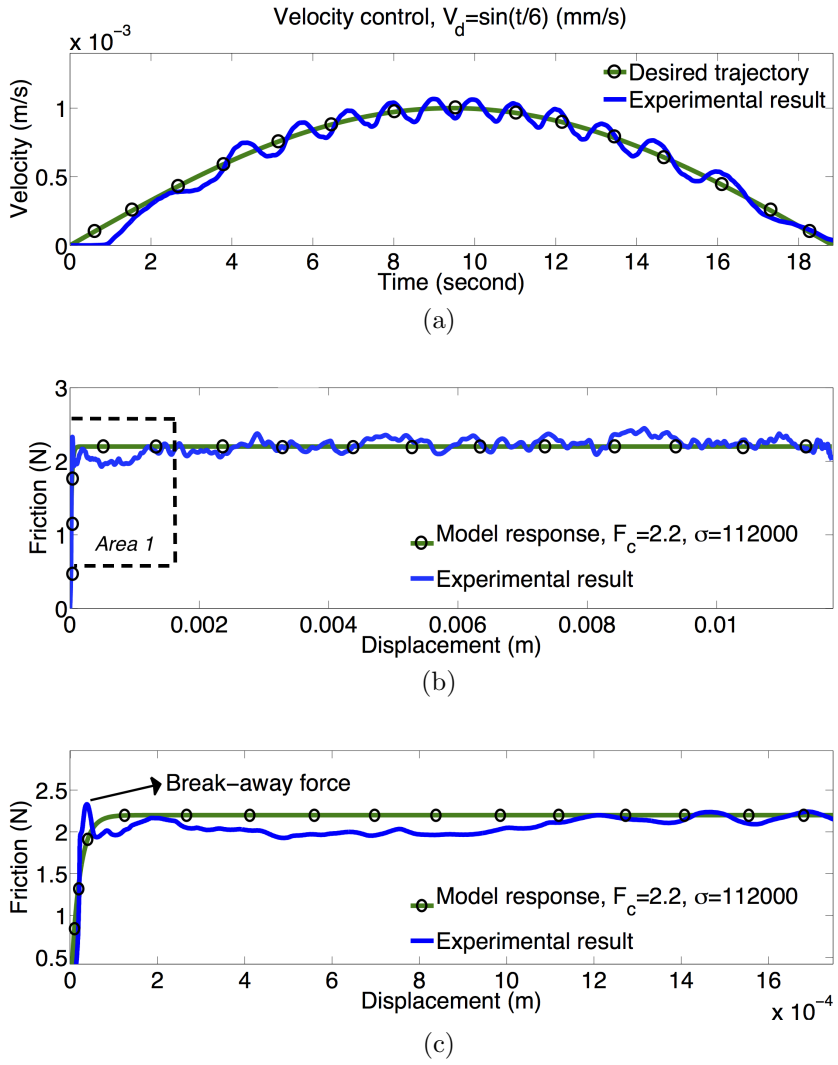


Figure 2.8: Experimental data and fitted curve (trial No. 7).

and $n$ refers to the number of conducted trials in the identification process. The bar on the left shows how the identified $\sigma$ varies. The bar on the right scales up to two standard deviation of the mean. Since all the points fall within the error bars covering the range of two standard deviation, they are considered to be normal. Similarly, the points displayed in Fig. 2.9b are fully encompassed within the two standard deviation band, but even closer to the mean.

Table 2.5: Nominal model parameters for Dahl model.

| Trial No. | $F_c[N]$ | $\sigma$ | Trial No. | $F_c[N]$ | $\sigma$ |
|---|---|---|---|---|---|
| 1 | 1.94 | 55000 | 9 | 1.99 | 84000 |
| 2 | 1.91 | 73000 | 10 | 1.85 | 70000 |
| 3 | 2.25 | 82000 | 11 | 2.27 | 87000 |
| 4 | 2.02 | 64000 | 12 | 1.79 | 107000 |
| 5 | 1.95 | 89000 | 13 | 1.76 | 103000 |
| 6 | 2.24 | 73000 | 14 | 2.0 | 105000 |
| 7 | 2.2 | 112000 | 15 | 1.93 | 108000 |
| 8 | 2.1 | 79000 | 16 | 1.87 | 113000 |
| $F_c$ nominal | 2.0 | $\sigma$ nominal | 87750 | | |

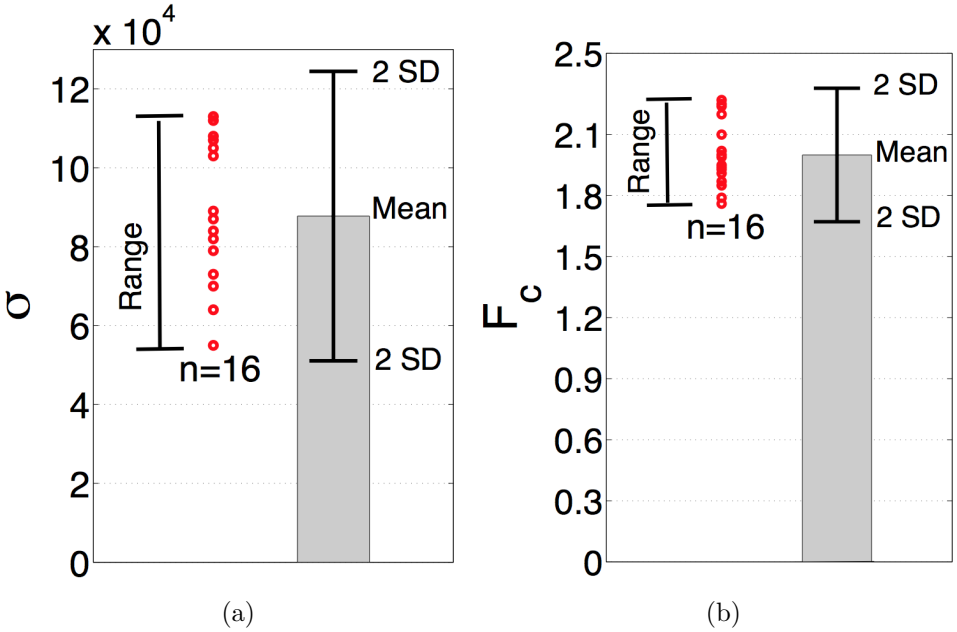


(a) (b)

Figure 2.9: Identified parameters spreading out within two standard deviation band.

### 2.3.3 Bliman and Sorine Model

#### 2.3.3.1 Procedure

Four parameters, $f_1$, $f_2$, $\varepsilon_f$ and $\eta$ in Eqn. (1.4) are identified through nine trials. The desired sinusoidal velocity trajectories and durations of the conducted trials are listed in Table 2.6. A PID controller regulates the velocity output and operates on

tracking error. The frequency and duration in each trial are chosen to slide the brass block for two complete cycles where only the second hysteresis cycle is adopted to perform the identification process. The friction-displacement map resulting from each trial contributes to one set of parameters.

Table 2.6: Desired velocity trajectories for B.S. model parameter identification.

| Trial No. | Desired velocity trajectory $[m/s]$ | Duration $[Second]$ |
|---|---|---|
| 1 | $2 \times 10^{-3} sin\,(2t/3)$ | 18.85 |
| 2 | $2 \times 10^{-3} sin\,(4t/5)$ | 15.7 |
| 3 | $2 \times 10^{-3} sin\,(t)$ | 12.57 |
| 4 | $3 \times 10^{-3} sin\,(2t/3)$ | 18.85 |
| 5 | $4 \times 10^{-3} sin\,(2t/3)$ | 18.85 |
| 6 | $5 \times 10^{-3} sin\,(2t/3)$ | 18.85 |
| 7 | $6 \times 10^{-3} sin\,(2t/3)$ | 18.85 |
| 8 | $6 \times 10^{-3} sin\,(4t/5)$ | 15.7 |
| 9 | $6 \times 10^{-3} sin\,(t)$ | 12.57 |

In each trial, two strictly defined reference points, $(x_e, F_s)$ and $(x_p, F_c)$ as shown in Fig. 1.7, are plotted on the displacement-friction map. The four parameters, $f_1$, $f_2$, $\varepsilon_f$ and $\eta$, can be determined with the known coordinates of two reference points using the following map $[F_s \quad F_c \quad x_e \quad x_p] \mapsto [f_1 \quad f_2 \quad \varepsilon_f \quad \eta]$:

$$\begin{cases} f_1 &= \dfrac{(m_1 m_2 + 2)\, p}{2\,(p-1)} F_c \\ f_2 &= \dfrac{m_1 m_2 p + 2}{2\,(p-1)} F_c \\ \varepsilon_f &= \dfrac{x_p}{3} \\ \eta &= \dfrac{m_1 m_2 + 2}{m_1 m_2 p + 2} \end{cases} \tag{2.8}$$

with $m_1$ and $m_2$ defined as

$$m_1 = \frac{F_s - F_c}{F_c}, m_2 = e^{3x_e/x_p} \tag{2.9}$$

and $p$ is the solution of

$$\frac{m_1 m_2 + 2}{m_1 m2} \ln p = (p-1) \ln m_2 \quad and \quad p > 1 \tag{2.10}$$

where the solution exists and is unique if and only if

$$\ln m_2 < \frac{m_1 m_2 + 2}{m_1 m_2} \tag{2.11}$$

for example when $3x_e < x_p$, as suggested in [36, 58]. This strong constraint on the coordinates of the two experimental reference points requires the a relatively large $x_p$ to obtain a set of valid parameters of the model. A sharp drop in the experimental friction profile will give rise to a unsolvable $p$ value.

#### 2.3.3.2 Results

All the hysteresis loops resulting from the trials presented in Section 2.3.3.1 are plotted on the friction-displacement map to identify the parameters. Figure 2.10 shows the velocity profile of Trial 6 and the resultant hysteresis loop which is taken to determine the two reference points. Figure 2.10a shows that overall the velocity of the brass block follows the desired trajectory reasonably well except for the block is in the vicinity of null velocity. Such a tracking error is attributed to the time that the controller spends overcoming the break-away force. Second part of Fig. 2.10a shows two peaks observed after the velocity zero-crossing on the hysteresis loop. Such peaks account for the break-away force. Figure 2.10b shows that the friction curve experiences a sharp drop after the break-away force is attained along with the coordinates of the two reference points.

Following the procedure presented in Section 2.3.3.1 the parameters are identified and shown in Table 2.7. Experimental results of Trial 6 is superimposed with the model prediction as shown in Fig. 2.10c. One can see that the model highly agrees with the experimental friction except for the sharp drops occurring before the friction converges to the steady-state value. It is found that the experimental friction drops faster than the model prediction.

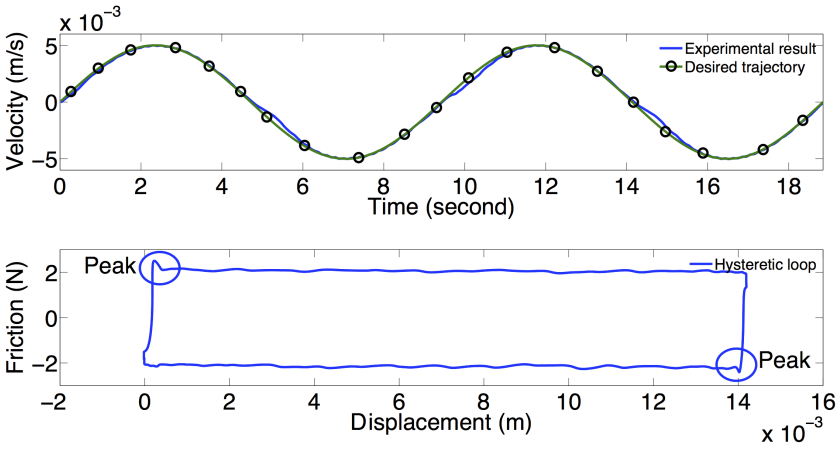


(a)

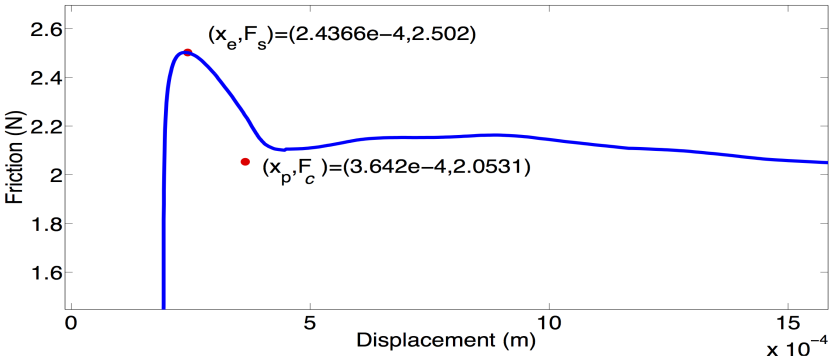


(b)

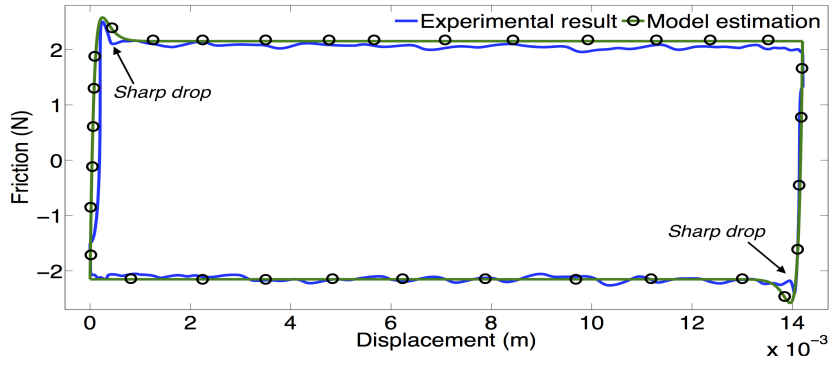


(c)

Figure 2.10: (a) Input profile giving block cyclic motion and its resultant hysteresis loop. (b) Selected two reference points plotted on break-away region in zoom. (c) Model estimation versus realistic friction profile.

According to Table 2.7, only two valid $p$ values are found over the nine conducted trials. The issue of having unsolvable $p$ values has been brought up in [31, 58] and is attributed to the sharp drop of the experimental friction after the break-away force is reached. Such a sharp drop makes the two reference points too close to guarantee the strong condition expressed in Eqn. (2.11). This constraint limits the availability of the parameters for this model. As a matter of fact, frictional surface featuring low stiffness of the asperities in contact will lead to a relatively large value of $x_e$ compared with those with high stiffness of the asperities. Such a large $x_e$ simply makes the constraint $3x_e < x_p$ almost impossible to achieve. Furthermore, it has been found that loading rate of input force during sticking affects the coordinate of first reference point $(x_e, F_s)$ as well. Lower force loading rate gives higher value of $F_s$ and $x_e$ in general. Overall, the parameter identification of the B.S. model is partially determined by a reference point $(x_e, F_s)$ that is highly sensitive to the factors varying from system to system, which makes the model difficult to be parameterized. Reference [58] proposed a solution to deal with this constraint by manually adjusting the coordinates of the two reference points, whereas the rational and the procedure of the adjustment was not discussed in the work.

Table 2.7: Identified parameters for B.S. model.

| Trial No. | $p$ | $(f_1, f_2, \varepsilon_f, \eta)$ |
|---|---|---|
| 1 | no solution | N/A |
| 2 | no solution | N/A |
| 3 | no solution | N/A |
| 4 | no solution | N/A |
| 5 | no solution | N/A |
| 6 | 1.2305 | $(19.875, 17.8227, 0.000121, 0.9063)$ |
| 7 | no solution | N/A |
| 8 | no solution | N/A |
| 9 | 1.1613 | $(9.4050, 7.3367, 0.000188, 0.7931)$ |

### 2.3.4 LuGre Model

#### 2.3.4.1 Procedure

Six parameters within the LuGre model, $F_c, F_s, V_s, \sigma_2, \sigma_0$, and $\sigma_1$ shown in Eqn. (1.6) and (1.7) fall into two categories. The first category, containing the first 4 parameters, is named static parameters and have been identified through the Stribeck curve obtained in Section 2.3.1. The remaining two parameters, $\sigma_0$ and $\sigma_1$ named dynamic parameters, allow the model to predict the microfine motion of the block before the break-away force is reached. These two dynamic parameters are identified through six trials associated with force control. The desired force of the conducted trials are listed in Table 2.8. For each trial, A PID controller regulates the force applied on the block and operates on tracking error. The time series of the microfine displacement resulting from each trial contributes to one set of dynamic parameters.

Table 2.8: Desired step input force values for LuGre model dynamic parameter identification.

| Trial No. | Desired force [N] | Trial No. | Desired force [N] |
|---|---|---|---|
| 1 | 0.5 | 4 | 1.0 |
| 2 | 0.5 | 5 | 1.5 |
| 3 | 1.0 | 6 | 1.5 |

To identify the dynamic parameters, the first step is to relate the microfine displacement sensed by the capacitance displacement sensor to the force applied on the mass block. In the presliding region, there is no gross motion and the displacement is caused by the junctional deformation, in which $z = x$ is satisfied [2, 31, 58–63]. Thus Eqn. (1.7) is revised using the notion $z = x$

$$F = \sigma_0 x + \sigma_1 \frac{dx}{dt} + \sigma_2 \dot{x} \tag{2.12}$$

Substituting the above equation into Eqn. (2.3) and keeping the $F$ at the left hand side, we have

$$F = m\ddot{x} + (\sigma_1 + \sigma_2)\,\dot{x} + \sigma_0 x \tag{2.13}$$

This second-order system can be further reduced to

$$F = \sigma_0 x \tag{2.14}$$

if the input force has a step profile and the system state $x$ reaches its steady state in presliding region. Equation. (2.14) can be used to parameterize the $\sigma_0$, and the identified values are averaged out to obtain the nominal value.

Once the nominal $\sigma_0$ is determined, the last coefficient, $\sigma_1$, is ready to be identified. Equation. (2.13) is equivalent to the following, given $m = 1$

$$F = \ddot{x} + 2\zeta\omega_n\dot{x} + \omega_n^2 x \tag{2.15}$$

where $\omega_n$ is the natural frequency and $\zeta$ represents the damping ration. Comparing Eqn. (2.15) with Eqn. (2.13), we obtain $\omega_n = \sqrt{\sigma_0}$ and also

$$2\zeta\sqrt{\sigma_0} = \sigma_1 + \sigma_2 \tag{2.16}$$

where $\zeta$ is determined as 1 as suggested in [64] to properly damp the system state $x$ while the velocity approaches to zero [58]. Having $\zeta = 1$ leads to the equation

$$2\sqrt{\sigma_0} = \sigma_1 + \sigma_2 \tag{2.17}$$

where $\sigma_1$ can be identified with known $\sigma_0$ and $\sigma_2$ values.

#### 2.3.4.2 Results

The time series data of the microfine displacements obtained from the trials presented in Section 2.3.4.1 are taken to identify the dynamic parameters. The static parameters have been identified in Section 2.3.1.2. Figure 2.11 shows the input force and the displacement profiles obtained from Trial 4 which is considered as a representative trial. It can be seen in Fig. 2.11a that the force takes approximately 4 seconds to reach the steady state. The controller gains are carefully tuned to ensure that the block is loaded in the presliding region. Figure 2.11b shows the variation in the

capacitance measured by the AD7747 chip. The capacitance decreases due to the increasing separation between two conducting plates. The variation in capacitance is converted to the displacement of the block using the conversion obtained in the calibration process. Such a displacement is treated as presliding as discussed in Section 2.2.2 and converges to approximately 15 $\mu m$ after the applied force is stabilized.

Following the procedure presented in Section 2.3.4.1 the dynamic parameter $\sigma_0$ is identified for each trial and shown in Table 2.9. The coverage of the two standard deviation band of the $\sigma_0$ shown in Fig. 2.12 indicates each identified $\sigma_0$ is considered to be normal. The nominal value of $\sigma_0$ is used to determine the $\sigma_1$ using Eqn. (2.17).

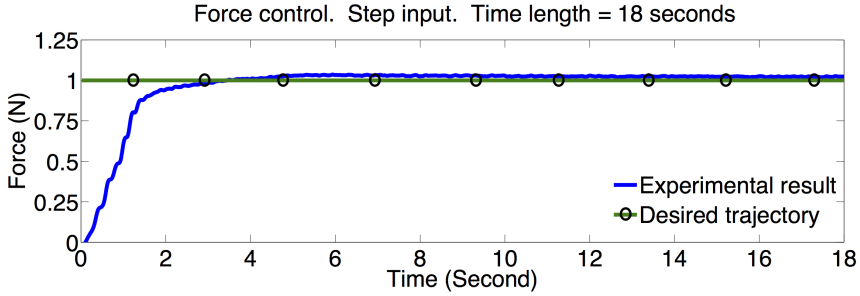


(a) Response of the applied force to the unit step input.

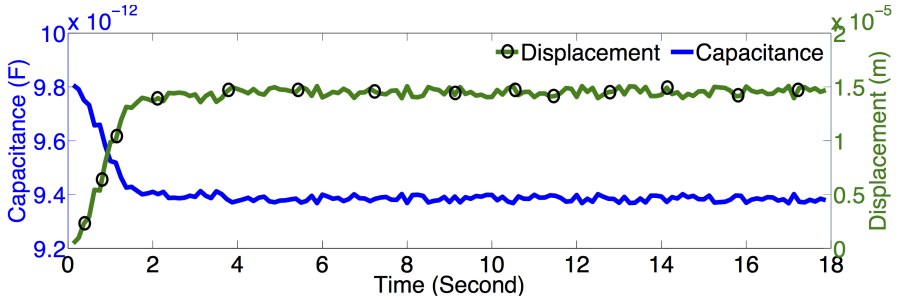


(b) Response of the capacitance displacement sensor together with displacement determined by the quadratic polynomial.

Figure 2.11: Experimental results obtained from a representative trial.

Table 2.9: Identified parameters for LuGre model.

| Trial No. | $\sigma_0$ $[N/m]$ | $\sigma_0$ nominal | $\sigma_1$ nominal |
|---|---|---|---|
| 1 | 65669.888 | 66967.231 | 344.56 |
| 2 | 68265.363 | | |
| 3 | 67188.616 | | |
| 4 | 66851.513 | | |
| 5 | 63950.064 | | |
| 6 | 69877.942 | | |

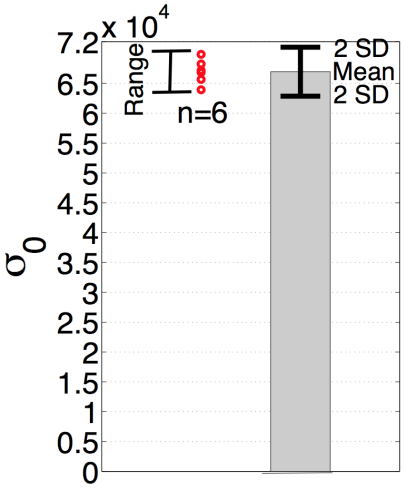


Figure 2.12: Identified parameters spreading out within two standard deviation band.

## 2.4 Feature Comparison

### 2.4.1 Experimental Trials for Feature Demonstration

**Break-away Force**

An experimental test is performed for 13 trials with various constant input forces ranging from $2.2\,[N]$ to $-2.4\,[N]$. The 13 trials are performed by assigning the desired input force to a dedicated PID controller. The force applied on the brass block is compared with the desired force to generate tracking errors. The desired forces for the trials are listed in Tab. 2.10. It has been experimentally found that any input force out of this range will initiate continuous motion of the block.

**Viscous Friction**

Table 2.10: Desired step input force values for break-away force demonstration.

| Trial No. | Desired force [N] | Trial No. | Desired force [N] |
|---|---|---|---|
| 1 | 0.3 | 8 | 2.2 |
| 2 | 0.6 | 9 | -0.3 |
| 3 | 1.0 | 10 | -0.6 |
| 4 | 1.5 | 11 | -2.1 |
| 5 | 1.8 | 12 | -2.3 |
| 6 | 2.0 | 13 | -2.4 |
| 7 | 2.1 | | |

An experimental test is performed for various constant velocities ranging from $v = \pm 3\, mm/s$ to $\pm 8\, mm/s$ with the equal interval of $1\, mm/s$. Five trials are repeated for each desired velocity, and the system velocity output is compared with the desired velocity to generate the tracking error. Such an error is taken by a dedicated PID controller to regulate the system output.

**Friction Lag**

An experimental test is performed to demonstrate friction lag. The desired sinusoidal velocity trajectory and duration of the control task is presented in Tab. 2.11. The system velocity output is compared with the desired input to generate the tracking error. Such an error is taken by a dedicated PID controller to regulate the system output.

Table 2.11: Desired velocity trajectories for friction lag demonstration.

| Desired velocity trajectory $[m/s]$ | Duration $[Seconds]$ |
|---|---|
| $1.5 \times 10^{-3} + 1 \times 10^{-3} sin\,(3t)$ | 18.85 |

**Varying Break-away Force**

An experimental test is performed for 20 trials with various force loading rates ranging from $0.08\,[N/s]$ to $20.3\,[N/s]$ with unequal intervals. The 20 trials are carried out by applying various constant operating voltage values to the motor. Overall, a larger operating voltage value results in a greater loading rate applied to the block.

**Presliding**

An experimental test is performed to demonstrate presliding, where the desired input force trajectory with respect to the time is presented in Fig. 2.13. Such a semi-ramp profile can avoid instantaneous changes in tracking error and any obvious overshoot in the control task. The maximum input force applied on block (1.5 N) is lower than the break-away force of the block (2.2 N), which ensures the block is moving in the presliding region. The input force remains null for the first 2 seconds and then changes in a linear manner with the ramp slope of 0.25 $N/s$ for another 2 seconds. Afterwards, the desired trajectory will be stabilized at a constant value for 3 seconds and ramped up until it reaches the next constant value as shown in Fig. 2.13. The force applied on the brass block is compared with the desired input force trajectory to generate the tracking error. Such an error is taken by a dedicated PID controller to regulate the system output.

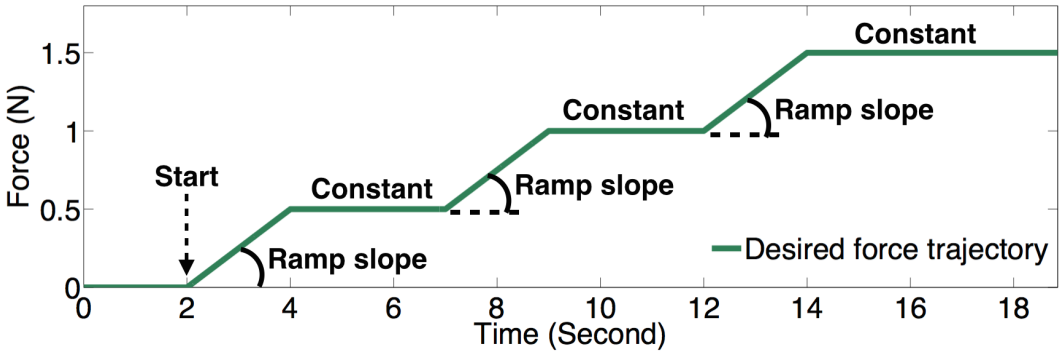


Figure 2.13: Desired input force trajectory used to demonstrate presliding.

### 2.4.2 Break-away Force

In Fig. 2.14a the experimentally obtained data points associated with null velocity indicate the range of the static friction for our experimental rig. The highest and lowest values in that range are used to overlap the break-away forces reproduced by the Classical, Dahl, B.S., and LuGre models. Note that all data points within the range are obtained using the force controller which outputs moderate loading rates to the block. The break-away forces for positive and negative directions are 2.2 and $-2.4$ $[N]$, respectively.

Figures 2.14b and 2.14c zoom in Area 1 and Area 2 in Fig. 2.14a, respectively. As shown in Figs. 2.14b and 2.14c, the break-away forces reproduced by the Classical, B. S. and LuGre model are close to the experimental observations for both directions. The biggest error percentage is about 5%, from the error percentages it can be concluded that the Classical, B.S. and LuGre model are adequate to characterize this feature. Note that the LuGre and Classical model reproduce the identical break-away force as the same set of parameters describing break-away force are shared between them. The break-away force reproduced by the Dahl model is not presented since it can not describe this feature. The structures of chosen friction models also provide insight into the break-away force predictions associated with the models, related analysis based on which is presented below.

The Classical model presented in Eqn. (1.1) shows that the break-away force is characterized by the parameter $F_s$. An external force higher than the $F_s$ takes the object out of the presliding region. The B.S. model is graphically presented in Fig. 3. The expression of the break-away force $F_s$ corresponding to the $x_e$ is derived in Ref. [58] and has the form of

$$F(x_e) = f_1 - f_2 + f_2 \left( \frac{f_2 \eta}{f_1} \right)^{\frac{1}{1-\eta}} (1 - \eta) \tag{2.18}$$

where the break-away force $F_s$ is a constant determined by the parameters $f_1$, $f_2$ and $\eta$. The LuGre model is presented in Section 2.3.4,. By means of the following transformation

$$s = \int_0^t |v(\tau)| \, d\tau \tag{2.19}$$

the LuGre model becomes

$$\frac{dz}{ds} = sgn(v) - \sigma_0 \frac{1}{g(v)} z \tag{2.20}$$

$$F = \sigma_0 z + |v| \, \sigma_1 \frac{dz}{ds} + \sigma_2 v \tag{2.21}$$

For simplicity, neglecting the bristles damping and the viscous friction coefficient as

suggested in Ref. [58], Eqn. (2.21) simplifies to

$$\frac{dF}{ds} = \sigma_0 \left( sgn\left(v\right) - \frac{1}{g\left(v\right)} F \right) \tag{2.22}$$

Eqn. (2.22) is a first order model and the $F$ is partially determined by the velocity dependent term $\frac{\sigma_0}{g(v)}$. The function $g\left(v\right)$ characterizes the famous Stribeck curve and is bounded in a range of $F_c \leq g\left(v\right) \leq F_s$, the output of which is governed by the $v_s$ and the system velocity. According to the discussion presented in Ref. [58], Eqn. (2.22) represents the friction during the sticking phase. Higher sliding velocity during the presliding region gives rise to lower steady-state output of (2.22). Such an output is considered as the break-away force reproduced by the LuGre model. As a result, the break-away force is not a constant when the LuGre model is used, in fact, the microsliding velocity during the presliding region is the key factor determining the break-away force of the system. In this section the loading rates used to numerically demonstrate the break-away forces are low, which are consistent with the experimental trials carried out to obtain the experimental break-away forces shown in Figs. 2.14b and 2.14c.

In summary, the break-away forces reproduced by Classical and B.S. models are unique constants determined by the parameters while the LuGre does not. The LuGre model dynamically adjusts its break-away forces in response to different experimental conditions. All the three models show a good agreement with the experimental results subject to low loading rates.

### 2.4.3 Viscous Friction

All the friction profiles estimated from the trials presented in Section 2.4.1 are plotted on the friction-velocity map for comparison. Figures 2.15a and 2.15b represent the experimental viscous friction of positive and negative velocity, respectively. The points contributing to each testing velocity are clustered closely, which indicates that the viscous friction produced by our rig is highly repeatable. The viscous friction appears to be velocity-dependent. The higher the velocity the higher the friction.

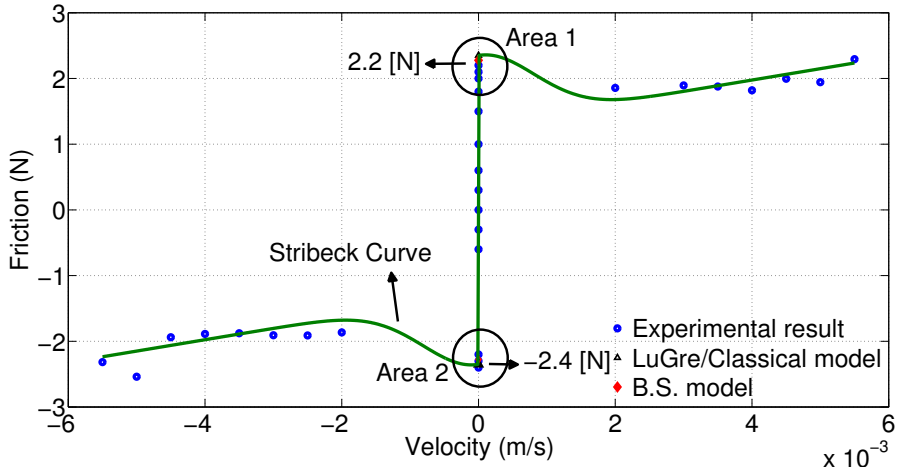


(a) Stribeck curve together with the predictions of the break-away force reproduced by the Classical, B.S. and LuGre model.

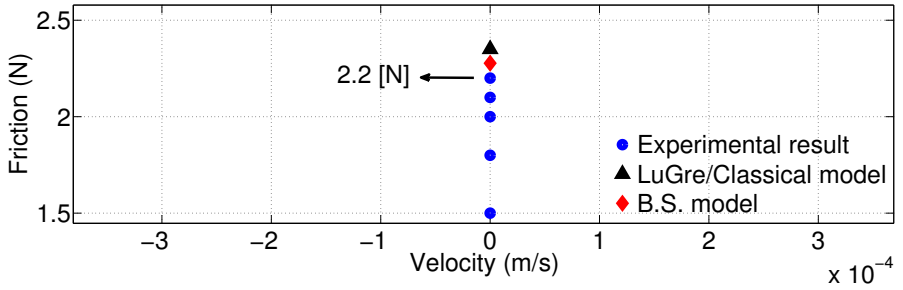


(b) Zoom in to area 1.

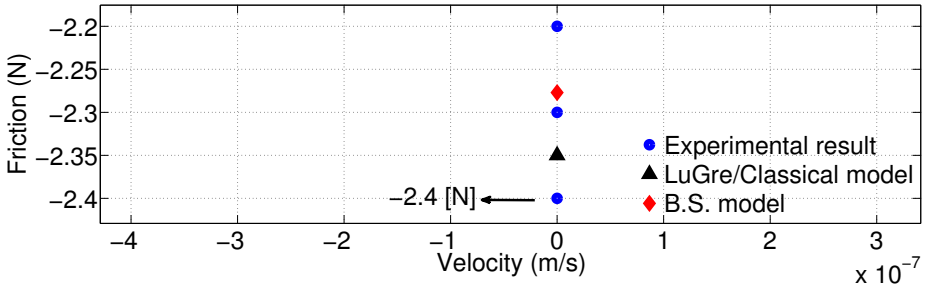


(c) Zoom in to area 2.

Figure 2.14: Static friction-velocity map together with break-away force reproduced by selected models.

In Fig. 2.15c the viscous friction reproduced by the Classical, B.S., Dahl and LuGre model are plotted with the mean values of the experimental viscous frictions. The

error bars presented in Fig. 2.15c indicate the range of 2 standard deviation of the mean values. According to Ref. [57], each experimental point is considered normal if it falls within the above range. One can observe in Fig. 2.15c that the error bars encompass all of the viscous friction reproduced by the LuGre and the Classical model. Therefore, these two models are adequate to characterize the viscous friction. The viscous friction reproduced by the Dahl and the B.S. model remain constant regardless of the velocities, which results in a significant discrepancy in the case of high velocity. It is concluded that the Dahl and the B.S. model does not characterize the viscous friction.

The Classical model presented in Eqn. (1.1) indicates that the viscous friction is obtained by superimposing a term $\sigma_2 v$ linearly varying with velocity on a constant $F_c$. The Classical model is inherently adequate to capture the viscous friction. The Dahl model presented in Eqn. (1.2) shows that the friction only depends on the displacement since the last change of $sgn\,(v)$, the output of which monotonically converge to the $F_c$ with the transient behavior determined by the $\sigma$. The friction output of B.S. model is solely governed by the displacement, which will approach its steady-state value $(f_1 - f_2)$ with growing displacement. This reveals that the B.S. model has similar nature as the Dahl model and does not reproduce any rate-dependent behavior of friction. However the LuGre model presented in Eqn. (1.7) employs the term $\sigma_2 v$ to reproduce the viscous friction while in the gross sliding. Such a sliding makes the summation of the rest two terms of the model approximately $F_c$.

### 2.4.4 Friction Lag

The friction profile estimated from the task presented in Section 2.4.1 is plotted on the friction-velocity map for the comparison. Figure 2.16 shows a loop experimentally recorded under the assigned velocity range. The friction is higher for the acceleration period and lower for the deceleration period. The multi-value friction behavior becomes obvious when the velocity is approaching zero. Referring to Fig. 2.16, the friction lag reproduced by the Dahl and the B.S. model are constants with respect to the varying velocities, which leads to the conclusion that these two models do not

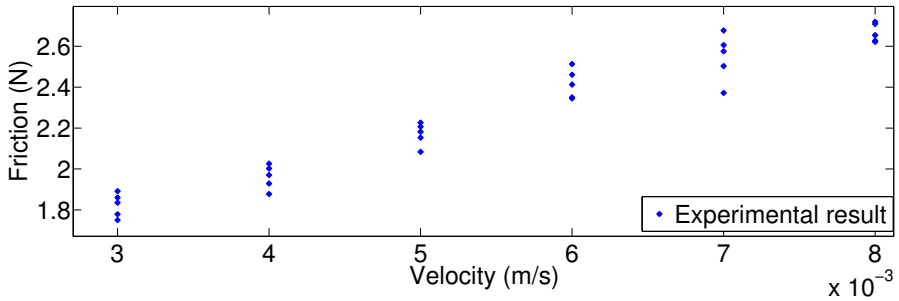


(a) Steady-state characteristics of the friction (Positive velocity).

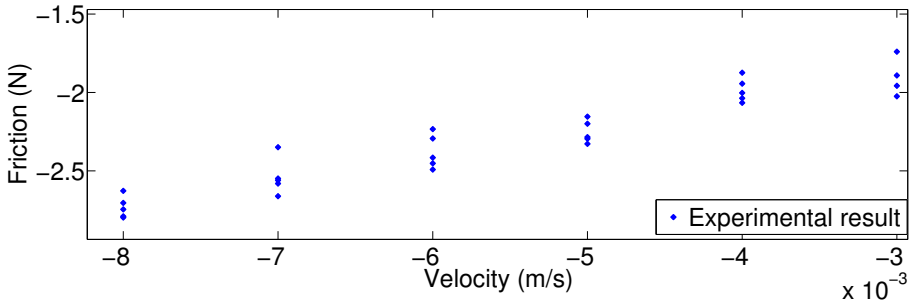


(b) Steady-state characteristics of the friction (Negative velocity).

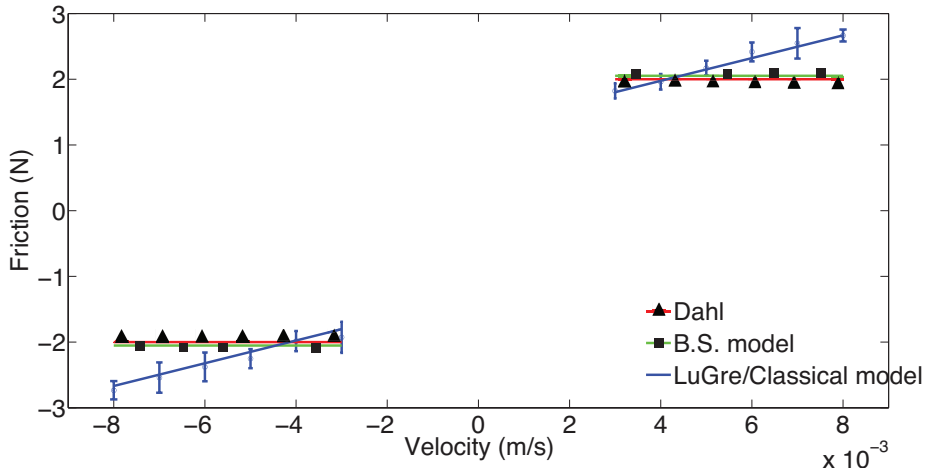


(c) The mean values (circles) and 2 standard deviations (error bars) of the steady-state measurements together with viscous friction reproduced by selected models.

Figure 2.15: Viscous friction behaviour under static velocity profiles.

account for the multi-value shown in Fig. 2.16. The friction lag reproduced by the Classical model varies linearly with the velocity. However, such a prediction does not agree with the friction loop occurring at the low velocity. A more sophisticated

structure is needed to capture this loop pattern. The friction lag reproduced by the LuGre model shows a loop pattern, which follows the experimental observations with a maximum deviation of 7.6% recorded at $V = 5 \times 10^{-4}\, m/s$. Therefore, It is concluded that the LuGre model is the only adequate model among the selection to characterize the friction lag.

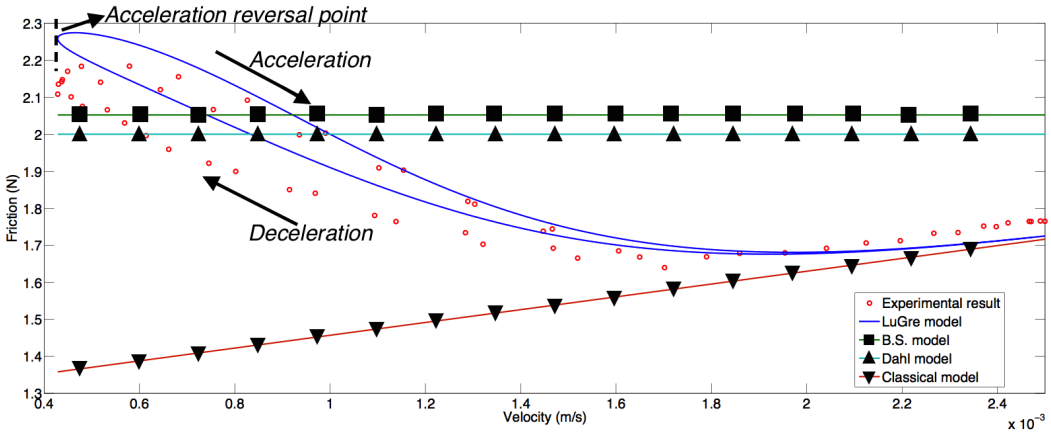


Figure 2.16: Friction lag characteristics of friction (unidirectional velocity variation, slide sinusoidally within $0.5 - 2.5\, mm/s$, freq.=$0.48\, Hz$, two successive cycles of velocity variation are plotted).

The Classical model presented in Eqn. (1.1) uses a term $\sigma_2 v$ to describe the rate dependency of the friction. Any nonzero velocity corresponds to a unique friction force, which indicates the loop pattern cannot be reproduced by the Classical model. The Dahl and the B.S. model cannot reproduce any rate-dependent behavior either, the simulation results of both models become constants when the velocity is varied. Reference [64] shows that the LuGre model presented in Eqn. (1.7) is able to capture the friction lag, and the term $\sigma_0 z$ dominates the friction when it comes to reproducing the friction lag. Thus we consider

$$F = \sigma_0 z \tag{2.23}$$

where the $\frac{dF}{dv}$ can be obtained as following

$$\frac{dF}{dv} = \frac{\sigma_0 v}{a} - \frac{\sigma_0^2 |v| z}{g(v)\, a} \tag{2.24}$$

where $a$ is the acceleration, and the derivative of the friction with respect to the velocity is dynamically determined by $a$, $v$ and $z$. Let us examine the friction behavior around the acceleration reversal point marked in Fig. 2.16. When the velocity is changing from the deceleration to the acceleration period, at the reversal point, $a$ in Eqn. (2.24) becomes a positive value due to the acceleration, which forces the friction curve not to follow the path associated with the deceleration period but bending upward until Eqn. (2.24) gives a negative value. The zero-crossing of acceleration during the transient makes the friction show a loop on the friction-velocity map which is in line with the experimental observations reported by other researchers.

In summary, only the Classical and the LuGre model show the rate dependency among the chosen models, which corresponds to the findings in last section. The stiffness term $\sigma_0 z$ within the LuGre model gives additional rate dependency, which allows the model to reproduce friction lag.

### 2.4.5 Varying Break-away Force

The break-away forces estimated from the trials presented in Section 2.4.1 are plotted on the friction-loading rate map. The map uses a base 10 logarithmic scale for the horizontal-axis and a linear scale for the vertical-axis. As shown in Fig. 2.17, the break-away force shows a dramatic decrease with the increasing loading rate. The prediction of break-away forces from the Dahl model is not presented due to its inability to reproduce such a force. The break-away forces reproduced by the B.S. and the Classical model show an unchanged trend regardless of the variation in loading rate. Such predictions do not agree with the experimental observations. However, the break-away forces reproduced by LuGre model tend to follow the measurements with a maximum deviation of 8% recorded at the loading rate of $20.3\,N/s$. It is concluded that the LuGre model is adequate to capture this feature.

As the discussion presented in Section 2.4.2, the break-away forces of the Classical and the B.S. model are unique constants. The LuGre model utilizes the function $g(v)$ to dynamically determine the break-away force based on the experimental conditions. A Literature survey in Section 1.2.1.3 has shown that the break-away force varies with

the loading rate of the external force. An extremely low loading rate of the external force will result in the low sliding velocity during the presliding region, which makes the output of the function $g(v)$ equal to $F_s$, and therefore the break-away force of the system defined by Eqn. (2.22) has the value of $F_s$. Once the loading rate of the external force increases significantly, the output of function $g(v)$ is moved to another end of the boundary, which reduces the break-away force of the system accordingly. Note that the break-away force reproduced by the LuGre won't enter the open interval $(-F_c, F_c)$.

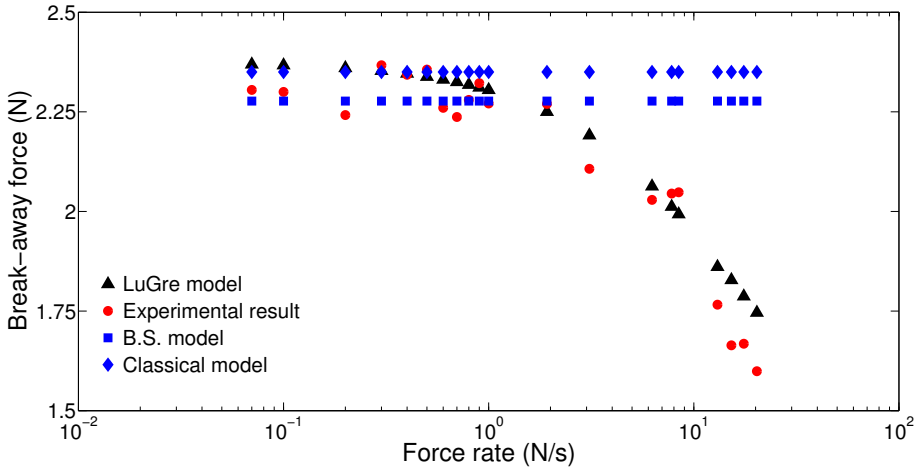


Figure 2.17: Relation between break-away force and force rate.

### 2.4.6 Presliding

The time series of the presliding resulting from the test presented in Section 2.4.1 is plotted in Fig. 2.18 for the comparison. Figure 2.18a shows that the applied force follows the desired force with a minor tracking error, which is attributed to the moderate controller action. The presliding reproduced by the Classical and the LuGre model are graphically illustrated in Fig. 2.18b and compared with the experimental presliding. As can be seen in Fig. 2.18b, the presliding responds quickly to the variation in the applied force without the presence of obvious oscillations, the behaviour of which is similar to a critically damped system with an applied unidirectional force.

Figure 2.18b shows that the classical model tends to hold the brass block at rest when the loading is below the break-away force, but in contrast the LuGre model highly agrees with the experimental results. This high accuracy given by the LuGre model on tracking the presliding is attributed to its model structure and in the way the two dynamic parameters, $\sigma_0$ and $\sigma_1$, are identified. Based on the discussion presented in Ref. [64] , the presliding response of the LuGre model becomes critically damped if the identification procedure suggested in Ref. [64] is strictly followed. Overall, the quality of the dynamic parameters and the identification procedure dominates the model performance in terms of presliding prediction.

Figure 2.18c and 2.18d show the presliding profiles reproduced by the B.S. and the Dahl model. The predictions are similar and they neither capture the magnitude nor depict the trend of the experimental presliding. Both predictions feature a long rise time, which indicates the models act like an overdamped system and can not account for the presliding. However, the Dahl model in several previous works, has been considered a decent model to reproduce the presliding. The inconsistent observation is elaborated in the following. The time domain of the Dahl model has the form of

$$\frac{dF}{dt} = \sigma \left(1 - \frac{F}{F_c} sgn\left(v\right)\right)^{\alpha} v \tag{2.25}$$

where $F$ is the friction, $\sigma$ is the stiffness coefficient, $v$ is the velocity of the object and $\alpha = 1$ is most commonly used. The Dahl model presented by Eqn. (2.25) behaves as a stiff spring (stiffness $\sigma$) at a low relative friction force ratio $\frac{F}{F_c}$ and it can be used to reproduce the presliding [65]. However, in this work, such a relative friction force ratio is not negligible as the $F$ is comparable with the $F_c$ ($F$ is approximately equivalent to the experimental input force shown in Fig. 2.18a at each time step and the $F_c$ value is experimentally identified as 2.0). As a result this additive force ratio term coupled with $sgn\left(v\right)$ deviates the presliding response of the model from the ideal spring representation, which explains why the presliding reproduced by the Dahl in Fig. 2.18d does not have a short transient response to the variation in the applied force. This idea can be further illustrated by the numerical trial shown in Fig. 2.19. Figure 2.19 demonstrates the presliding profile reproduced by the Dahl

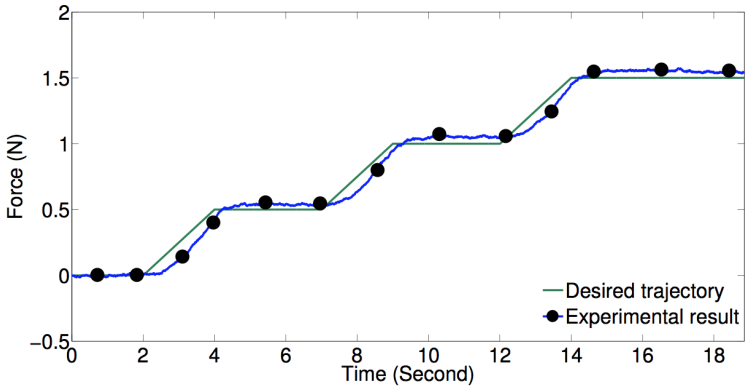


(a) Input force profile.

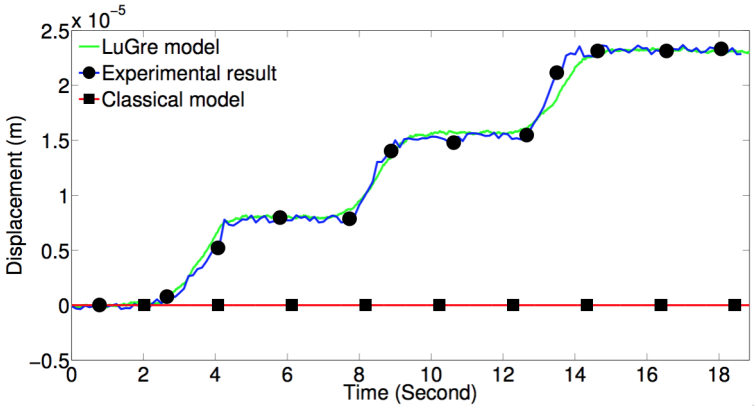


(b) Presliding together with predictions of Classical and LuGre model.

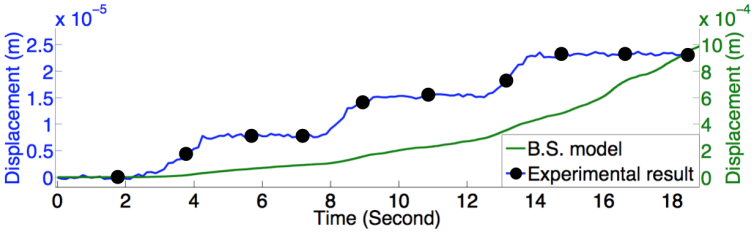


(c) Presliding together with prediction of B.S. model.

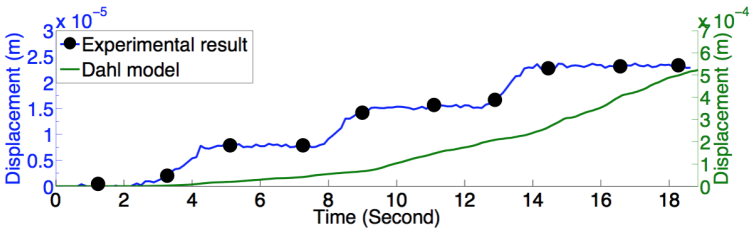


(d) Presliding together with prediction of Dahl model.

Figure 2.18: Presliding measurements along with model predictions (slope=0.25 $N/s$)

model coupled with the parameters experimentally identified. The upper part of the figure is the step input force applied to the brass block, and the lower part is the presliding response from the Dahl model. Note that the input force is lower than the break-away force level of the object to obtain the presliding prediction. The presliding profile reproduced by the model subject to our parameters obviously features a slow transient response in response to the input force, which implies that the model is inadequate to describe the presliding that varies so quick with changing input force. In summary, the Classical model does not reproduce the presliding at all. The Dahl

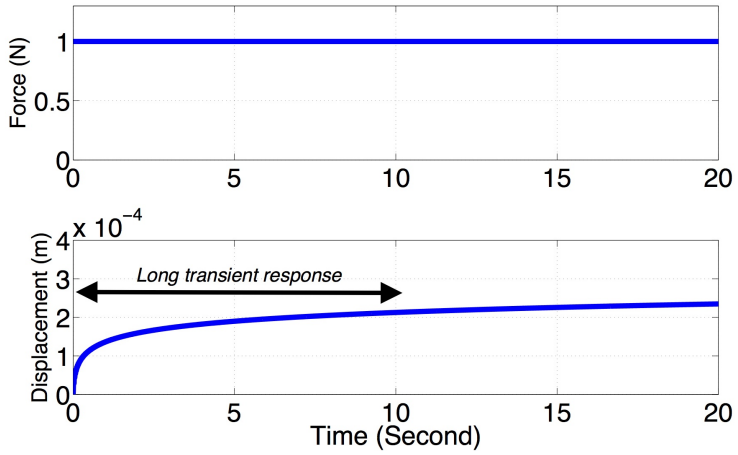


Figure 2.19: Presliding response of Dahl model due to instantaneous change in input force.

model can be used to reproduce the presliding as long as the relative friction force ratio $\frac{F}{F_c}$ in the numerical trials is low enough to be negligible [65]. Nevertheless, it is believed that the Dahl model is adequate up to a critical $\frac{F}{F_c}$ value. Once the critical value is exceeded, the $\frac{F}{F_c}$ term starts to play a role in the presliding response, which makes the Dahl model less realistic in presliding prediction. The B.S. model gives the presliding profiles that are significantly different from the experimental results. The LuGre model is adequate to capture this feature.

### 2.4.7 Comparison of Candidate Friction Models

A comprehensive experimental-numerical feature comparison for the candidate models (The Classical, the Dahl, the B.S. and the LuGre model) has been conducted in this chapter. A one-dimensional sliding block was built and used to demonstrate the frictional features of interest. Additionally, the candidate models' parameters are the result of identification on the same sliding block. The three criteria, namely simplicity, flexibility and controllability, are well undertaken in the design of the setup. The feature comparison leads to the recommendation facilitating the selection of the most relevant model. With such a model, a high level of accuracy for the numerical studies is achievable. Moreover, the model helps control engineers in designing the control laws reducing the strong influence induced by friction. The different friction models studied are as follows:

1. If the object is loaded from rest and the model must reproduce the break-away force resulting from a relatively low loading rate, all the models explored can be used to facilitate the analysis except the Dahl model. Break-away forces induced by the aggressive force rates show a steeper slope between any two points with distinct $x$ coordinates.

2. If the object is loaded from the rest and the loading rate is relatively high, the LuGre model is the only model able to reproduce the break-away forces during varying loading rate. As can be seen in Fig. 2.17, the break-away forces produced by other models remain constant regardless of the changing loading rate. The LuGre model forms a more comparable prediction to the experimental observations.

3. If the study is concerned with presliding, the LuGre model must be used to carry out the analysis. However, identifying the dynamic parameters in the model requires quite precise measurements on the presliding resulting from the known force. The Dahl model is adequate conditionally as we discuss in the previous sections.

4. If the studied object moves with a periodic motion unidirectionally or bidirectionally, the LuGre model should be considered due to the presence of friction lag.

5. If the studied object moves mainly with the gross motion, i.e. the viscous friction dominates the friction, the Classical and the LuGre model simulate accurate prediction on the observed friction. The Dahl and the B.S. model are able to predict the viscous friction by simply adding one representative velocity-dependent term. This modification can be found in [41, 58].

Table 2.12 summarizes the properties of the candidate models based on the conducted study. Friction modelling still needs to be emphasized in order to have the better friction representation, although some models have incorporated most of the features found in diverse applications. Other minor factors often omitted should be considered when developing a new model, e.g., temperature, lubricant film thickness and varying contact surface conditions. However it is important to balance model complexity and accuracy. A good model should at least carry a straightforward parameter identification and meet the real-time computational needs.

Table 2.12: Summary of candidate friction models.

| Model | Break-away force | Viscous friction | Friction lag | Varying break-away force | Presliding | Remarks/ Drawbacks |
|---|---|---|---|---|---|---|
| Classical | ✓ | ✓ | | | | Longest history but discontinuity may hinder numerical analysis |
| Dahl | | ✓[1] | | | ✓[2] | The $1^{st}$ dynamic friction model but with limited accuracy |
| B.S. | ✓ | ✓[1] | | | | Improved Dahl model but significantly increases system state dimension |
| LuGre | ✓ | ✓ | ✓ | ✓ | ✓ | Versatile but parameter identification could be a problem |

[1]By adding a representative velocity-dependent term into equation
[2]The model is adequate conditionally.

## 2.5 Summary

This chapter has proposed an experimental setup featuring simplicity, flexibility and versatility. The velocity and the loading force of the block are well-controlled with this setup. They can be either a constant value or varying in a specific fashion. The development of the capacitance displacement sensor in this setup allows it to have the capability to capture the microscope displacement occurring in the presliding regime. The location where the capacitance displacement sensor is installed ensures the accuracy of the presliding measurements. With this setup, the behaviours of friction in either presliding or gross-sliding regime can be accurately captured.

It has been shown that the parameterization of the selected friction models can be satisfactorily performed by the proposed setup, though for the B.S. model the unsolvable $p$ values are observed in some of the conducted trials. Such a limitation in parameter identification for B.S. model has been pointed out by other researchers in this filed and is attributed to the strong constraints imposed by the model designers. The rectification dealing with this limitation is beyond the scope of this thesis. While friction does vary from system to system, its basic behaviours are the same in many mechanical systems. The experimental friction behaviours produced by the proposed setup not only complete the candidate friction models but also can be used for development of new advanced friction models. It is a very effective and valuable setup for friction-related studies.

Finally, the comparison between the experimental features and the numerical features from the candidate friction models are conducted in this chapter. The comparison makes clear that the LuGre model can account for all the friction features reviewed in Chapter 2 with a relatively good accuracy. As a result, such a model is used to formulate the state space models of our setup which can be written in the form of $\dot{x} = f(x)$. In the next chapter, the stability analysis of our setup is studied aiming at uncovering the effect of the parametric perturbations. Such perturbations can be either a stabilizing or destabilizing factor to our system, and it should not be ignored if a stable system is desired. While the state space models do vary from system to system, the basic features of friction are the same. The stability analysis

results presented in Chapter 3 can provide qualitative insight into the behaviour of a number of systems.

# Chapter 3

# Stability Analysis

## 3.1 Introduction

Previous chapter has confirmed that the friction behaviours of the proposed setup can be satisfactorily modelled by the LuGre model. Nevertheless, even the friction is modelled with high accuracy, there is always a slight mismatch between the values of the identified parameters and the particular system characteristics to be defined. As a result, the effect of such parametric uncertainties (perturbations) on system stability must be studied. This chapter presents the stability analysis based on the proposed setup having the perturbed $\sigma_0$ and $\sigma_1$ values in the LuGre model, provided it is experimentally challenging to measure the presliding for the identification procedure.

Several analysis techniques have been applied to this topic, such as system linearization, describing function analysis (DFA) and Lyapunov's direct method. The system linearization involves the linearization of the original nonlinear system where all the conventional analysis techniques applicable to linear systems can be used to approximate the nonlinear system behaviour near the equilibrium. Therefore, the analysis results are only comparable to the original nonlinear system locally. Such a technique becomes invalid if the global information is required in the stability analysis. DFA is widely adopted where the analysis results become inaccurate when the nonlinearity within the system is dominant. This technique may not deliver satisfactory analysis results since the friction is well known for its nonlinearity, especially when

the motion of the object is semi-static. Lyapunov's direct method is another analysis technique where the decisive scalar energy-like function, also known as Lyapunov function, should be obtained to examine the system stability. However, such a scalar function becomes challenging to be derived in the presence of the LuGre model. The concept of Lyapunov exponents (LEs) has been confirmed an alternatively powerful and systematic tool to fundamental diagnostics in the stability of a control system. The most attractive point of the concept LEs is that the LEs can be constructively calculated by several well-established algorithms. By estimating LEs, the stability analysis of complex dynamic systems can be rigorously carried out.

Aiming at uncovering the effect of the parametric perturbations, the experimental setup presented in the last chapter subject to two different controllers with LuGre model is investigated in this chapter. Two controllers synthesized based on the state space model representing our setup are employed to carry out the stability analysis using the concept of LEs. $\sigma_0$ and $\sigma_1$ in the LuGre model are perturbed around their nominal values, and the stability analysis results reveal the controllers' ability to reject parametric perturbations.

## 3.2 Concept of Lyapunov Exponents

Stability analysis for a high dimensional nonlinear system is a truly challenging task but also fundamental since it is important to know how to guarantee the stability of a system. The concept of Lyapunov exponents(LEs) has been proved a powerful and systematic tool to fundamental diagnostics in the stability of a dynamic system [66, 67]. A smooth nonlinear autonomous dynamic system can usually be expressed by a set of differential equations in the form

$$\dot{x} = f\left(x\left(t\right)\right) \tag{3.1}$$

where $x \in \mathbb{R}^n$ is the $n \times 1$ state vector, and $f\left(x\left(t\right)\right)$ is a continuously differentiable vector function. Given a set of initial condition $x\left(0\right) = x_0$, Eqn. (3.1) defines a curve in state space as time varies from zero to infinity. Considering a infinites-

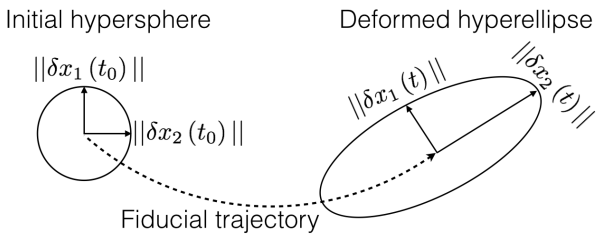


Figure 3.1: Evolution of 2-dimensional infinitesimal sphere.

imal $n$-hypersphere of initial conditions in the state space, the effect of the system dynamics will distort (stretch or contract) the lengths of the principal axes of that $n$-hypersphere as time goes by, which turns the original hypersphere into a hyperellipse as a result. Figure 3.1 demonstrates how a 2-dimensional infinitesimal hypersphere evolves in time, and the LE spectrum is then defined by Eqn. (3.2), where $\|\delta x_i(t)\|$ and $\|\delta x_i(t_0)\|$ correspond to the lengths of the $i^{th}$ principle axes of the $n$-hyperellipsoid at the current and the initial time instance, respectively. The use of binary logarithm in Eqn. (3.2) was presented in [68].

$$\lambda_i = \lim_{t\to\infty} \frac{1}{t} \log_2 \frac{\|\delta x_i(t)\|}{\|\delta x_i(t_0)\|} \tag{3.2}$$

Referring to Eqn. (3.2), one can easily find that LEs are related to the stretching or contracting nature of different directions in phase space. A system with $n$ states will have $n$ exponents, and the exponents are independent of initial conditions if attracted by the same attractor. It is well known that the qualitative behavior of a system can be described by its LE spectrum: a stable fixed point will have all negative exponents; one zero exponent is a signature of limit cycle with all the rest negative; and one positive exponent may be taken as chaotic. Wolf and his colleagues proposed an algorithm to estimate the exponents from analytically defined model [68]. In such an algorithm, a "fiducial" trajectory is selected as the the center of the $n$-hypersphere, the behavior of which is governed by the nonlinear equations on some initial conditions. The trajectories of the points on the surface of the sphere, which are infinitesimally separated from the central point, are determined by the

linearized equations. The principle axis are determined by the initially orthonormal vector frame anchored to the fiducial trajectory at each time instance. The above-mentioned linearized equations govern the evolution of the orthonormal vector frame with respect to time. Wolf's algorithm leads to the following equations

$$\dot{x}(t) = f(x(t)) \tag{3.3}$$

$$\dot{\Psi}_t = J(x(t))\,\Psi_t \tag{3.4}$$

where $\Psi_t$ is the state transition matrix of the linearized system $\delta x(t) = \Psi_t \delta x(0)$. $J(x(t))$, the Jacobian matrix of the original differential equations Eqn. (3.3), is defined as

$$J(x(t)) = \left.\frac{\partial f(x)}{\partial x^T}\right|_{x=x(t)} \tag{3.5}$$

and the initial conditions for numerical integrations are

$$\left\{ \begin{array}{c} x(t_0) \\ \Psi_t(t_0) \end{array} \right\} = \left\{ \begin{array}{c} x_0 \\ I \end{array} \right\} \tag{3.6}$$

where $I$ is a $n \times n$ identity matrix.

LEs are defined by all the column $n$-vectors $\delta x_i$ in $\Psi$ matrix determining the volume of the $n$-ellipsoid at each time step. However, the vectors tend to fall along the direction of most rapid growth resulting in the exponents difficult to compute accurately, thus, the repeat use of Gram-Schmidt reorthonormalization (GSR) procedure is proposed in Wolf's work to orthonormalize the $n$-vectors during each integration step. As can be seen in Fig. 3.2, such a procedure converts a set of vectors $\{\delta x_1, \delta x_2\}$ into a new set of orthonormal vectors $\{u_1, u_2\}$, the $j = 1, \cdots, k$ in the figure denotes the number of integration step. The procedure firstly orthogonalizes the initial vector set $\{\delta x_1, \delta x_2\}$ into $\{v_1, v_2\}$, then normalizing the vector set $\{v_1, v_2\}$ is performed to obtain the vector set $\{u_1, u_2\}$. GSR procedure has orientation preserving properties which allows an arbitrary initial vector set to be chosen. One can obtain LEs by the

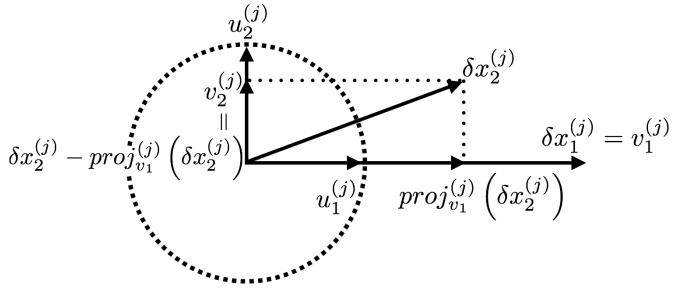


Figure 3.2: Graphical interpretation of GSR for a set of 2D vectors.

vector set $\{u_1, u_2\}$ with a proper time-step size $h$ and a large enough integer $k$,

$$\lambda_i \approx \frac{1}{kh} \sum_{j=1}^{k} log_2 \left\| u_i^{(j)} \right\| \tag{3.7}$$

where $j$ is the number of integration steps.

Conceptually, there are different type of stabilities, among which two basic notions have been widely applied in system engineering: the stability of a system with respect to its equilibrium point and the structural stability itself [69]. In the former case, we have to define the region-of-attraction (ROA) of a stable equilibrium point by perturbing the system states on the phase portrait. All the trajectories emanating from the defined ROA should converge to the equilibrium point. In the latter case, the perturbations are applied on the nominal parameters of a system to examine that to what extent the perturbed system still behaves qualitatively the same dynamics as the unperturbed system. In other words, one can interpreted it as finding the tolerance regions for the parameters of interest. In this study, we focus on the structural stability of the studied system using the concept of LEs as it reflects the idea that parametric perturbations exist in any realistic system and should be carried out as a fundamental requirement at the design phase of a system for its practical value.

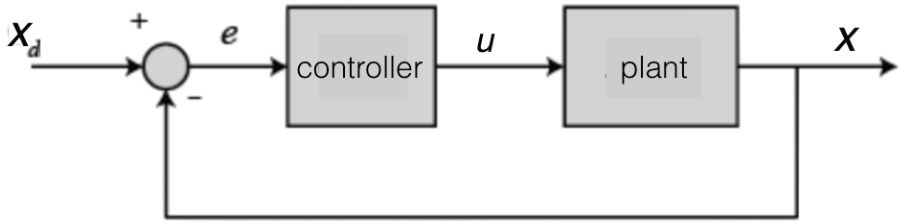


Figure 3.3: Block diagram of plant with controller.

## 3.3 State Space Model

A set-point position control is implemented on the setup presented in this thesis. The block diagram of the close-loop system is shown in Fig. 3.3. $x$ and $x_d$ represent the displacement of the block and the desired reference input, respectively. $e$, the tracking error, is taken by the controller to generate the plant input which is motor terminal voltage represented by $u$ in Fig. 3.3. The friction behaviour at the sliding surface dominates the friction in the plant and is described by a modified version of the LuGre friction model [70] which still preserves the most important analytical properties demonstrated by its original form.

The reason behind this replacement is due to the algorithm for LEs calculation outlined in Section 3.2, where the Jacobian of the state space equation at each time step is required. However, the derivative of the bristle deflection, $\dot{z}$, defined by the original LuGre model depends on the term $|v|$ which is the absolute value of the sliding velocity, therefore the $\ddot{z}$ apparently becomes undefined when $v = 0$. Such an undefined output of $\ddot{z}$ makes the Jacobian of the state space equation not able to be determined under that specific velocity, and a modified LuGre model is needed as a result. A smooth approximation to the absolute value is substituted based on the rectification in [70]. The original system, Eqn. (3.8), is approximated by Eqn. (3.9).

$$\frac{dz}{dt} = v - \frac{\sigma_0 |v|}{g(v)} z \tag{3.8}$$

$$\frac{dz}{dt} = S_v^2 v - \frac{\sigma_0 S_v v}{g(v)} z \tag{3.9}$$

where the main modification lies in the term $|v|$ in the original form approximated by $S_v v$. It is apparent that the non-differentiable term $|v|$ is employed only to inform the absolute value of $v$, this task can also be carried out through the product of $v$ and function $S_v$

$$S_v = \frac{2}{\pi} \arctan(K_v v) \tag{3.10}$$

where $K_v$ is set to $K_v = 10^8$ in order to have a good approximation of $|v|$ as recommended in [70]. The numerical model behaviours obtained from the modified LuGre model are compared with those simulated by the original LuGre model in [70], where both models yield indistinguishable numerical results if $K_v$ is chosen as $10^8$ given the same set of parameters. This means that the parameter we obtained in Section 2.3.4 for the original LuGre model are valid for the modified LuGre model in which the important features of friction can still be preserved.

Based on Fig. 3.3, we define state $x_1$ as $x_1 = x - x_d$ where $x_d$ is a constant in this study, provided it is a set-point position control, the overall system equation can thus be described in a 4-dimensional space based on the Newton's second law and the modified LuGre friction model in conjunction with the motor dynamics in the form of

$$\dot{x_1} = x_2 \tag{3.11}$$

$$\dot{x_2} = \frac{1}{m}\left[k_{tpm} x_4 2\pi p - \sigma_0 x_3 - \sigma_1 S_v^2 x_2 + \frac{\sigma_0 \sigma_1 S_v x_2 x_3}{g(x_2)} - \sigma_2 x_2\right] \tag{3.12}$$

$$\dot{x_3} = S_v^2 x_2 - \sigma_0 \frac{S_v x_2}{g(x_2)} x_3 \tag{3.13}$$

$$\dot{x_4} = \frac{1}{L_a}\left[u - x_4 R_a - k_{apm} 2\pi p x_2\right] \tag{3.14}$$

where $u$ is the controller that will be elaborated later and

$$S_v = \frac{2}{\pi} \arctan(K_v x_2) \tag{3.15}$$

Table 3.1: Physical interpretation of parameters and their nominal values

| Parameter | Physical interpretation | Nominal values | Remarks |
|---|---|---|---|
| $k_{tpm}$ | Torque constant | 37.4 [mNm/A] | Parameters of the motor/ball screw |
| $k_{apm}$ | Speed constant | 255 [rpm/v] | |
| $L_a$ | Terminal inductance | 0.953 [mH] | |
| $u$ | Voltage source applied to the motor | | |
| $R_a$ | Terminal resistance | 21.4 [Ω] | |
| $p$ | Pitch of the ball screw shaft | 1000 [rev/m] | |
| $\sigma_0$ | Stiffness of the bristle | 66967.231 [N/m] | Parameters of the LuGre model |
| $\sigma_1$ | Damping of the bristle | 344.56 [Ns/m] | |
| $\sigma_2$ | Viscous friction coefficient | 173 [Ns/m] | |
| $F_c$ | Coulomb friction | 1.284 [N] | |
| $F_s$ | Break-away force | 2.35 [N] | |
| $V_s$ | Stribeck velocity | 0.00113975 [m/s] | |
| $K_v$ | positive constant | $10^8$ | |

Table 3.2: Definition of states

| State | Definition |
|---|---|
| $x_1$ | $x - x_d$ |
| $x_2$ | Velocity of the block |
| $x_3$ | Average deflection of bristles at the contact junction |
| $x_4$ | Armature current of the motor |

$$g\left(x_2\right) = F_c + \left(F_s - F_c\right) e^{-\left(x_2/V_s\right)^2} \tag{3.16}$$

Physical interpretations of the parameters and the definition of the states are presented in Tab. 3.1 and Tab. 3.2, respectively. The parameters of the friction model are obtained in our lab by identification procedures described in Section 2.3.4. Other parameters come from the manufacture catalogues.

## 3.4 Controller Design and Simulations

### 3.4.1 Input-Output Linearization Controller

#### 3.4.1.1 Development of Controller

Input-output linearization controller, a classical nonlinear controller, is used to carry out our control objective which is minimizing the tracking error ($x_1$) of the set-point position control. The design of the controller subject to our plant involves finding a direct relation between the controlled state of the system ($x_1$) and the controller output $u$ by differentiating $x_1$ in Eqn. (3.11) three times. Afterwards the $\dddot{x}_1$ is directly related to the $u$ and can be represented by

$$\dddot{x}_1 = f(x) + \frac{2\pi p k_{tpm}}{mL_a}\, u \tag{3.17}$$

where $f(x)$ consisting of the system states and the nominal parameters can be found in Appendix. Clearly, Eqn. (3.17) represents an explicit relation between $x_1$ and $u$. By properly designing the controller output $u$ based on such a direct relationship, the controlled state will converge to zero exponentially. More discussions, applications and the design procedures of this controller can be found in [52]. The controller output $u$ which is the voltage applied to the motor has the form of

$$u = \frac{mL_a}{2\pi p k_{tpm}} \left[ V - \hat{f}(x) \right] \tag{3.18}$$

where $\hat{f}(x)$ can be found in Appendix. Such a function is part of our controller output $u$ and is identical to the $f(x)$ except for the parameters are denoted with hats. The selection of $V$ will be discussed later. Substitution of this controller into the plant dynamics Eqn. (3.17) leads to a new relationship between the $x_1$ and the function $V$

$$\dddot{x}_1 = V - \hat{f}(x) + f(x) \tag{3.19}$$

$$= V - \tilde{f}(x) \tag{3.20}$$

where $\tilde{f}(x)$ is defined as $\hat{f}(x) - f(x)$ and the newly defined function $V$ has the form

$$V = -18\ddot{x}_1 - 107\dot{x}_1 - 210x_1 \tag{3.21}$$

where the coefficients coupled with the state $x_1$ and its derivatives are carefully selected for shortest settling time in our set-point position control task without exceeding the motor's nominal voltage which results in extra heat and shorter lifespan of the motor.

Ideally, if one can estimate all the parameters precisely (i.e. no parametric uncertainty and parameter values within $f$ and $\hat{f}$ are the same, e.g. $\sigma_0 = \hat{\sigma_0}$), $\tilde{f}$ in Eqn. (3.20) becomes null as a result and leads to a simple linear triple-integrator relationship between the state $x_1$ and the $V$

$$\dddot{x}_1 = -18\ddot{x}_1 - 107\dot{x}_1 - 210x_1 \tag{3.22}$$

which represents an exponentially stable $x_1$ regardless of initial conditions. However, it is imperative that the identified parameters we use to describe the studied system can only be approximations. The parametric perturbations can give additive terms on the right-hand side of the linear triple-integrator relationship shown in Eqn. (3.22), which likely change the qualitative behaviour of the studied system. Therefore, it is fundamental but desperately in need of knowing the sensitivity of the controller to the perturbations that are not modelled in the design phase.

#### 3.4.1.2 Simulation Results

The controller designed above is used to perform the set-point position control on our experimental rig where all the parameters remain nominal. The desired input reference in this trial is selected to be $8cm$ with respect to the origin, which presents the initial conditions $\boldsymbol{x} = [-0.08, 0, 0, 0]^T$. Please note that the origin is the position of the brass block when the power is turned on. The corresponding displacement output is monitored and compared with the input reference to generate the tracking error. The simulation time is 20 seconds. As can be seen in Fig. 3.4, the displacement

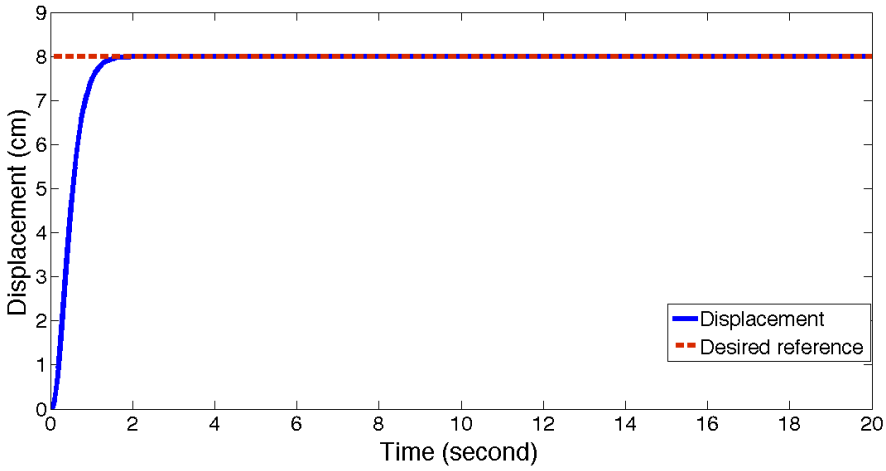


Figure 3.4: Numerical time response of displacement.

with respect to time (solid line) converges to the desired point (dotted line) rapidly without overshoot and steady-state error. These results suggest that the controller adopted in this work is very effective subject to our plant.

Figure 3.5 shows the controller output $u$ with respect to time during the control task. As can be seen that the voltage applied to the motor has a peak value of approximately 33 V at $t = 0.32$ seconds. The coefficients in Eqn. (3.21) are carefully chosen to bound the voltage within its nominal value which is 35 V. The rapid climbing voltage after launching the trial is caused by the initial tracking error. The voltage profile starts to decrease after the critical time instance $t = 0.32$ seconds and enters its steady state after $t = 1.5$ seconds due to the output eventually settles to its desired value. Based on the numerical results and the discussion presented here, it is concluded that using the input-output linearization controller can achieve a favorable displacement control performance without the consideration of friction uncertainty. However, so far the stability of the control system is not clear for varying friction parameters.

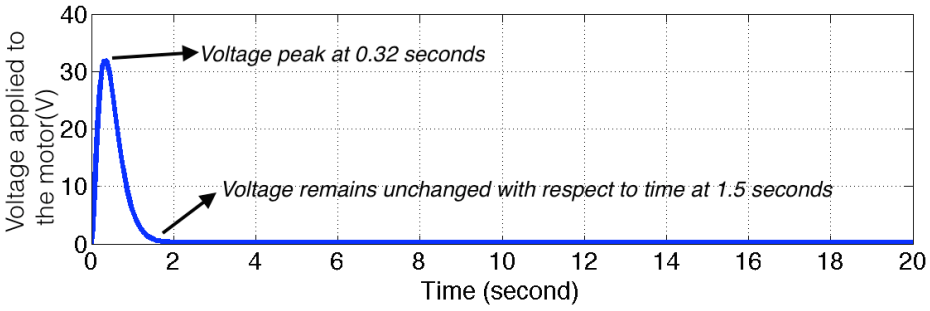


Figure 3.5: Voltage source applied to motor during set-point position control.

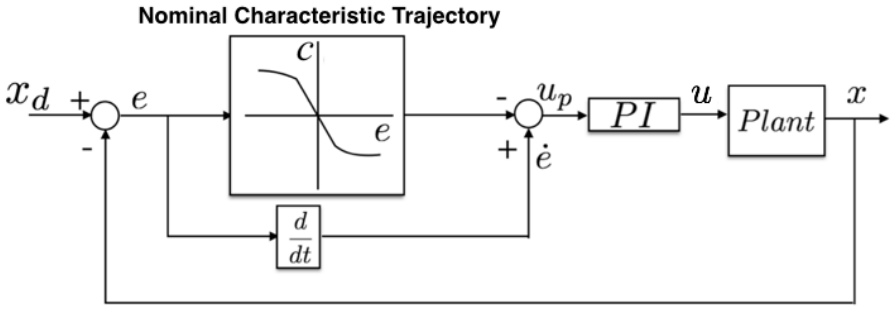


Figure 3.6: Structure of NCTF control system.

## 3.4.2 Nominal Characteristic Trajectory Following (NCTF) Controller

### 3.4.2.1 Development of Controller

NCTF controller is used to carry out our control objective which is minimizing the tracking error ($x_1$) of the set-point position control. The design of the controller involves finding an experimental nominal characteristic trajectory (NCT) and designing a PI compensator by using the NCT information. The block diagram of the NCTF controller is illustrated in Fig. 3.6, where the signal $u_p$ represents the difference between the actual error rate $\dot{e}$ and the NCT output $c$. Such a $u_p$ is taken by the PI compensator to generate the input voltage to the plant. It has been experimentally shown in [71–77] that although the NCTF controller is simple structurally, it can

regulate the control object better than the conventional PID controller with higher accuracy and robustness to friction variation when it comes to implementing tracking or set-point position control. Comprehensive discussions on the stability analysis and the theoretical background of the NCTF controller can be found in [75, 77]. Step-by-step design procedure of the NCTF controller subject to our plant is precisely described as follows:

1. Open-loop drive our plant with the step voltage input $u_r$ shown in Fig. 3.7a, and measure the amplitude of the velocity response $h$. $A$ is the time that the steady-state velocity needs to take to converge to static (deceleration process). In this paper, the amplitude $u_r$ is chosen as 85% of the nominal voltage of the motor to avoid the plant from being damaged. As can be seen in Fig. 3.7b, the $u_r$ is selected as 30 volts, and $h$ and $A$ are measured as 0.1193 m/s and 0.1 seconds through the numerical experiments.

2. The NCT is constructed by using the open-loop response $h$ and $A$. As can be seen in Fig. 3.7c, $m$ is defined as the inclination near the origin, which will be used to design the PI compensator gains. In this work $m$ is estimated as

$$m = -\frac{h}{A} = -1.193 \tag{3.23}$$

3. Design the compensator gains $K_p$ and $K_i$ based on the NCT information. According to [71],

$$K_p = \frac{2\zeta\omega_n u_r}{mh} \tag{3.24}$$

$$K_i = \frac{\omega_n^2 u_r}{mh} \tag{3.25}$$

where $\omega_n$ and $\zeta$ are decided by the designer. Based on the theoretical background of the NCTF controller proposed in [75, 77], the transfer function of a NCTF positioning control systems driven by DC servo motor can be simplified by a first order subsystem multiplied by a second order subsystem. The $\omega_n$ and $\zeta$ are the natural frequency and the damping ration of the second order

subsystem, and their effect on the overall system dynamics is studied in [77]. It is suggested to make $\omega_n$ larger than $\zeta$ [73] to have small overshoot and fast response, but at the same time their values should not be too large to give practically realizable control signal to the plant. In this work, $\omega_n$ and $\zeta$ are designed as 3 and 0.3, respectively. The rest of the parameters for determining $K_p$ and $K_i$ are obtained by Steps 1 and 2.

Due to the fact that the NCT controller incorporates a PI controller in its structure, it is not surprising that the integral part of the PI controller produces a signal that is proportional to the time integral of the signal $u_p$ during the control tasks. Such an integration brings an additional state $x_5$ into the system's state space equation, namely

$$\dot{x_5} = u_p \tag{3.26}$$

and the PI controller output within NCTF controller, which is the voltage applied to the motor is in the form of

$$u = K_p u_p + K_i x_5 \tag{3.27}$$

where $u_p$ is expressed as

$$u_p = -0.1193 \tanh(13.25 x_1) - x_2 \tag{3.28}$$

and the first term in Eqn. (3.28) represents the NCT shown in Fig. 3.7c. Figure 3.8 shows the model prediction from the first term superimposed with the NCT. The coefficients and the hyperbolic tangent function are the results of the curve fitting box programmed in Matlab in which the selected method and algorithm are Nonlinear-LeastSqures and Trust-Region. Other options are left with the default values. Please note that a smooth function is required to represent the NCT as the algorithm used in this thesis for Lyapunov exponent calculation relies on the smoothness of the system. Although a piecewise function can model the NCT better but the non-smoothness may hinder the exponent calculation.

Unlike the input-output linearization controller we discuss in the last section that takes so many parameters to construct the controller output, the NCTF controller

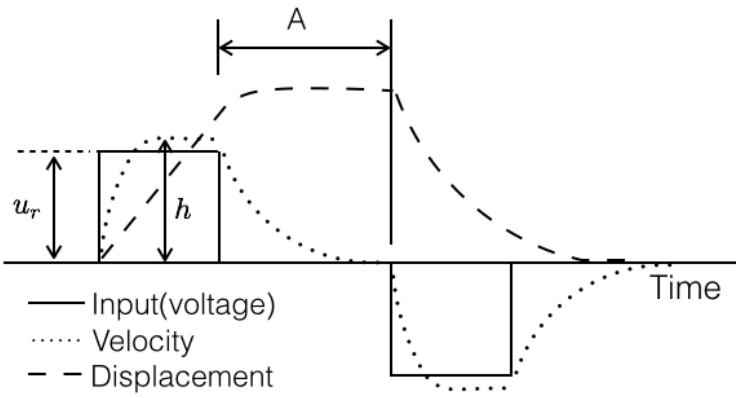


(a) Stepwise voltage input and corresponding responses.

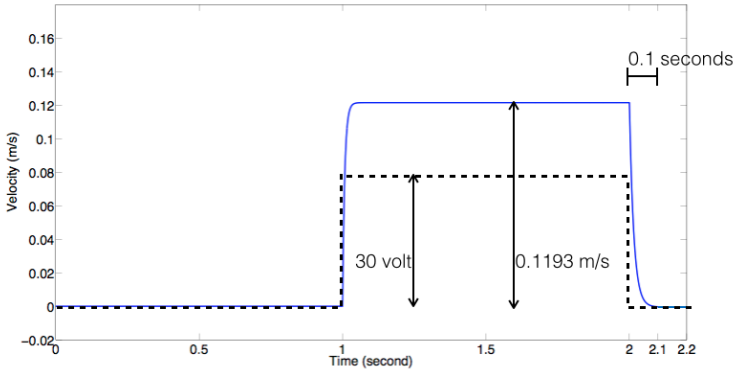


(b) Stepwise input and responses subject to our setup.

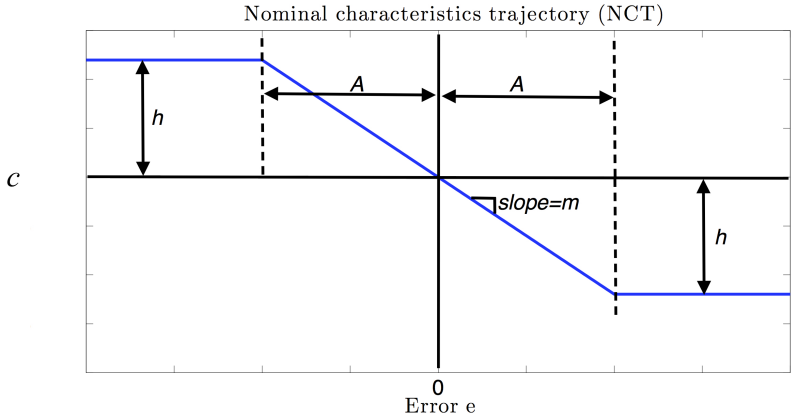


(c) Nominal characteristics trajectory (NCT).

Figure 3.7: Construction of NCT.

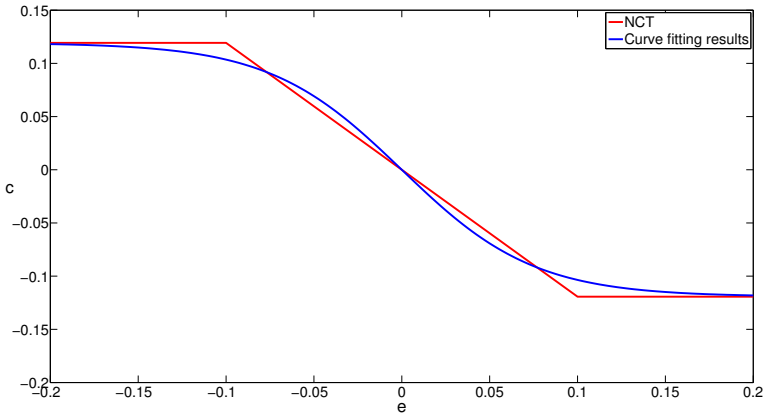


Figure 3.8: NCT and curve fitting results.

is computed mainly from two variables, $x_1$ and $x_2$, as seen in Eqn. (3.27) and (3.28). This feature makes the NCTF controller potentially more robust as the parameter variations do not directly add additive terms (perturbations) in the controller output. The sensitivity of the NCTF controller to the perturbations will be systematically examined later.

#### 3.4.2.2 Simulation Results

The controller designed above is used to perform the set-point position control on our experimental rig where all the parameters remain nominal. The desired input reference and time length of this numerical trial are selected identical to the trial conducted in Section 3.4.1.2, which leads to the initial conditions being $\boldsymbol{x} = [-0.08, 0, 0, 0, 0]^T$. As can be seen in Fig. 3.9, the displacement with respect to time (solid line) converges to the desired point (dotted line) rapidly without overshoot and steady-state error observed, which indicates that the control system has great quickness in responding to input with sudden changes. In many applications, the actual desired inputs of a system may vary in unpredictable manner, thus having such a great quickness to some extent implies that the system subject to the controller will perform satisfactorily to most of the forms of input signals.

Figure 3.10 shows the controller output $u$ with respect to time during the imple-

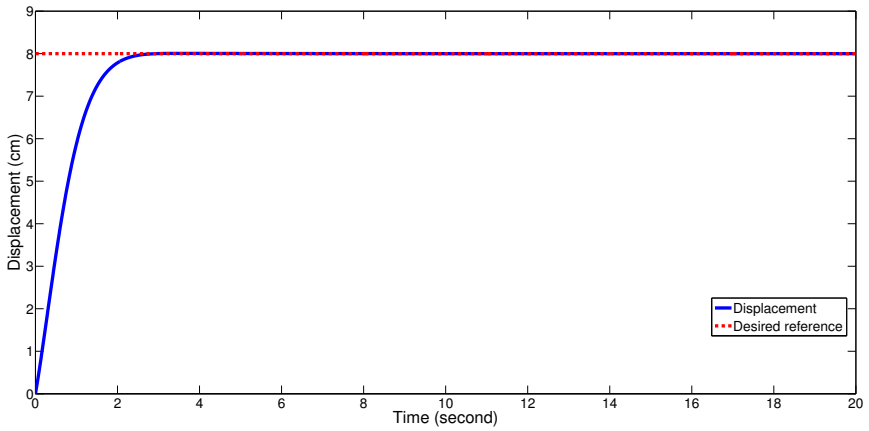


Figure 3.9: Numerical time response of displacement.

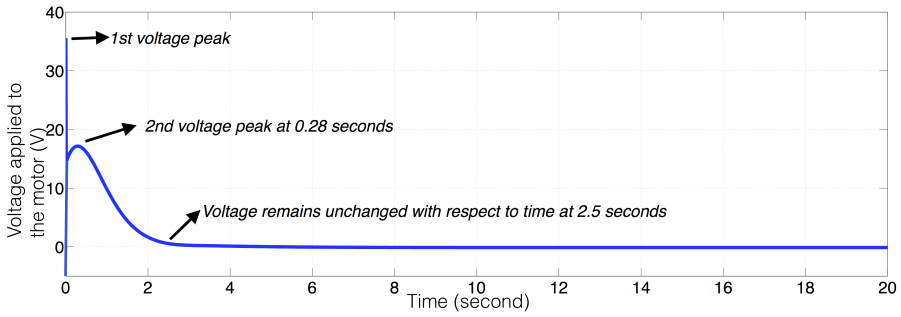


Figure 3.10: Voltage source applied to motor during set-point position control.

mented control task. The initial voltage peak is caused by the initial tracking error, and the voltage profile drops down rapidly right after the numerical trial is launched. Second voltage peak is observed approximately at t = 0.3 seconds. None of the peaks exceed the nominal voltage value of the motor. The voltage profile remains steady after $t = 2.2$ seconds due to the output eventually settles to its desired value. Based on the numerical results, it is concluded that for the NCTF controller, the desired position trajectory has been followed precisely, and the transient of the position following is quick and satisfactory. Stability of this control system is guaranteed based on the state trajectories. In conclusion, the NCTF controller achieves a favourable displacement control performance in absence of the friction uncertainty.

## 3.5 Effect of Parametric Uncertainties

### 3.5.1 Structural Stability Analysis for Input-Output Linearization Controller

Here we focus on how the parameters $\hat{\sigma_0}$ and $\hat{\sigma_1}$ in controller Eqn. (3.18) affect the control system stability while the rest parameters with hat notations remain nominal. The initial conditions for system states and the time length are consistent with the one used in Section 3.4.1.2. The concept of LEs can be used to carry out the system stability analysis associated with the perturbed parameters $(\hat{\sigma_0}, \hat{\sigma_1})$ on the $\hat{\sigma_0} - \hat{\sigma_1}$ parametric space around their nominal values. Two perturbed systems are presented in the following along with their state trajectories and the evolution of the exponents, from which the effect of the parametric uncertainties can be clearly seen. Last but not least, $\hat{\sigma_0}$ and $\hat{\sigma_1}$ values used in Eqn. (3.18) are perturbed in region $\Gamma_1$ defined in Section 3.5.1.3 where the qualitative behavior of each perturbed system is presented by different colors.

#### 3.5.1.1 Perturbed System 1:

$$(\hat{\boldsymbol{\sigma_0}}, \hat{\boldsymbol{\sigma_1}}) = (\mathbf{100.001}\ \%\ \boldsymbol{of}\ \boldsymbol{\sigma_0}\ \boldsymbol{nominal\ value}, \mathbf{103.251}\ \%\ \boldsymbol{of}\ \boldsymbol{\sigma_1}\ \boldsymbol{nominal\ value})$$

The $\hat{\sigma_0}$ and $\hat{\sigma_1}$ values are adjusted as 100.001% of the nominal $\sigma_0$ value and 103.251 % of the nominal $\sigma_1$ value, respectively. This means $\hat{\sigma_0} = 66967.331$ and $\hat{\sigma_1} = 355.76$. The initial conditions for system states and the time length are consistent with the one used in Section 3.4.1.2. Figure 3.11 and 3.12 demonstrate the time trajectories of all the system states. The convergence of the state trajectories can be typically linked to a stable system. Figure 3.13 depicts the evolution of all system LEs, from which it can be observed that all the exponents converge to the negative values as shown in each sub-datatips. The negative largest LE $\lambda_1$ in Fig. 3.13 is found $-0.03413$, suggesting the perturbed system has a stable fixed point.

The LEs of this particular perturbed system are calculated using the desktop presented in Section 2.2.1 and the algorithm introduced in Section 3.2. Calculating the LEs for this single case takes 1177 seconds to simulate. Note that such a computa-

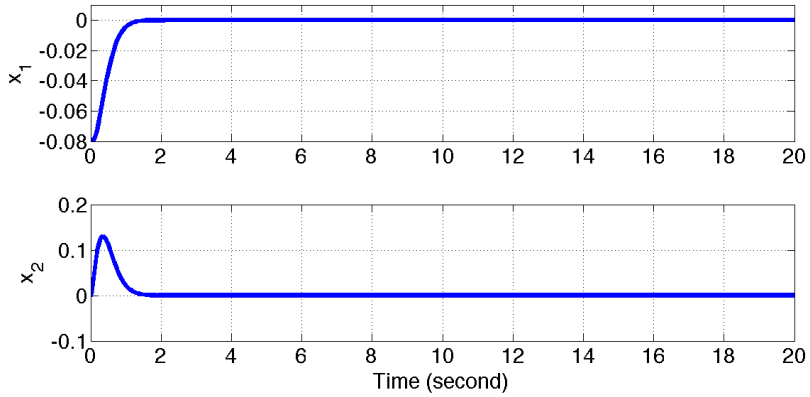


Figure 3.11: States $x_1$ and $x_2$ of input-output linearization control system.

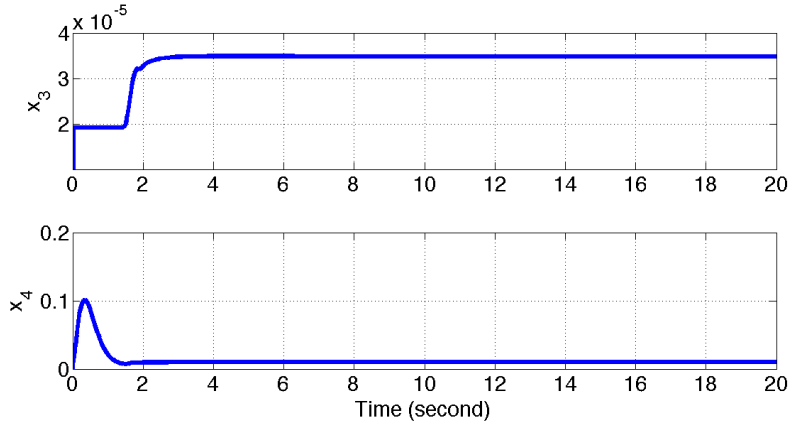


Figure 3.12: States $x_3$ and $x_4$ of input-output linearization control system.

tion time is strongly influenced by hardware and software architecture used for the calculation, thus it would not lead to a final judgement and is not calculated for the following perturbed control systems as a result.

#### 3.5.1.2 Perturbed System 2:

$$(\hat{\sigma_0}, \hat{\sigma_1}) = (\mathbf{99.998\,\%\, of\ \sigma_0\ nominal\ value}, \mathbf{101.407\,\%\, of\ \sigma_1\ nominal\ value})$$

The $\hat{\sigma_0}$ and $\hat{\sigma_1}$ values are adjusted as 99.998% of the nominal $\sigma_0$ value and 101.407% of the nominal $\sigma_1$ value, respectively. This means $\hat{\sigma_0} = 66966.331$ and $\hat{\sigma_1} = 349.41$. The initial conditions for system states and the time length are consistent with the

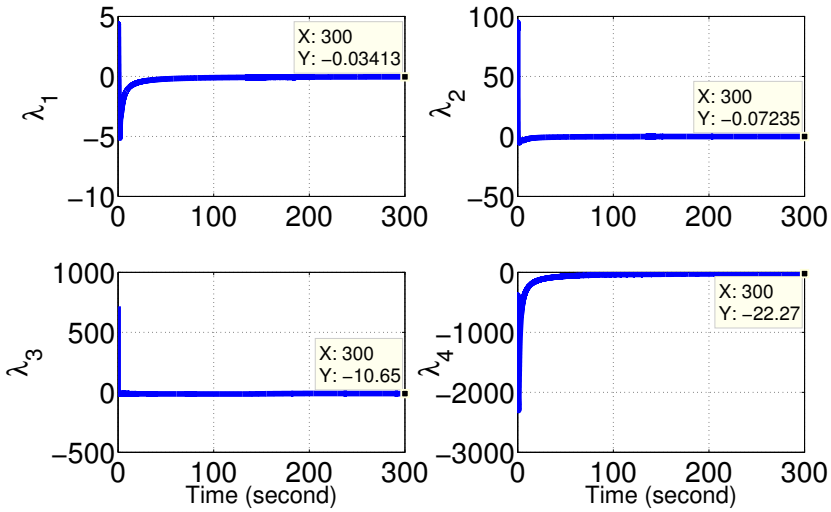


Figure 3.13: Evolution of system Lyapunov exponents (ordered in decreasing value).

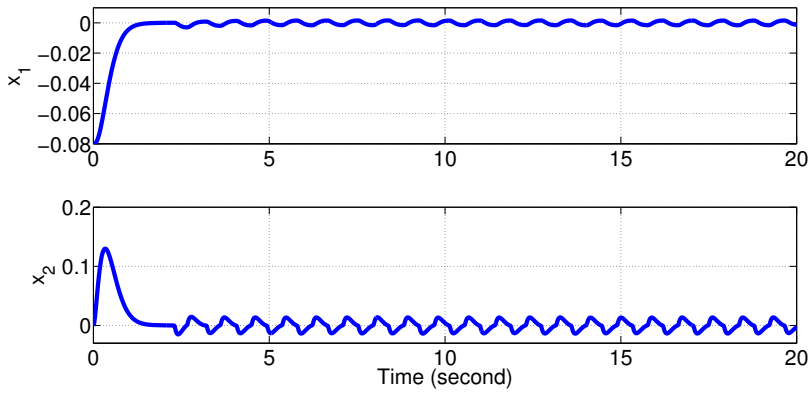


Figure 3.14: State $x_1$ and $x_2$ of input-output linearization control system.

one used in Section 3.4.1.2. Figure 3.14 and 3.15 show that the perturbed system displays sustained oscillations of fixed amplitude and fixed period in each system state with no external excitation throughout the trial. Such oscillations are limit cycles which are unique features of nonlinear system. Unlike the marginally stable linear system that has the amplitude governed by its initial conditions, the amplitude of the self-sustained oscillations in limit cycle are independent of the initial conditions.

Figure 3.16 shows the $x_1 - x_2$ phase portrait of the perturbed system, from

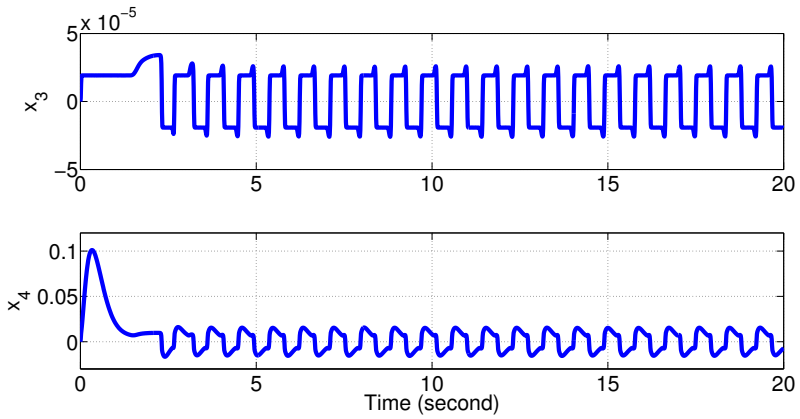


Figure 3.15: States $x_3$ and $x_4$ of input-output linearization control system.

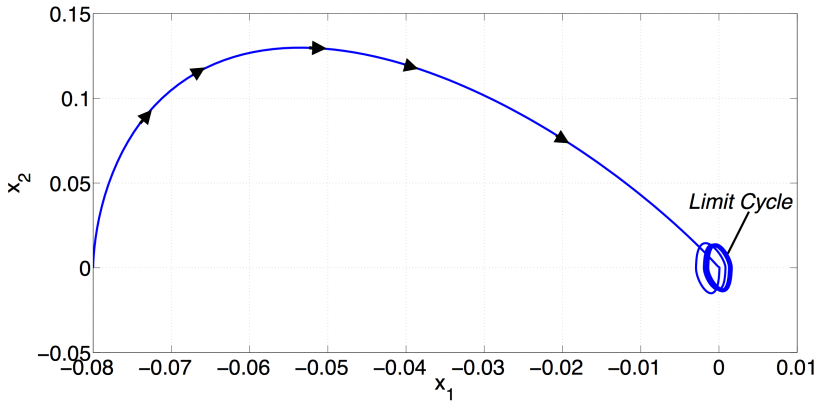


Figure 3.16: Phase portrait for system states $x_1$ and $x_2$.

which we observe that the trajectory starting from outside of the limit cycle converges to it as time goes by and cycles periodically around the origin. Figure 3.17 depicts the evolution of all system LEs. The values of the LEs are found to be $(0, -0.00173, -13.03, -13.19)$, indicating the perturbed system is moving in a stable periodic motion.

#### 3.5.1.3 Perturbation Region $\Gamma_1$

The numerical results obtained from the previous systems clearly show that the qualitative behaviour of the control system can be significantly changed by minor

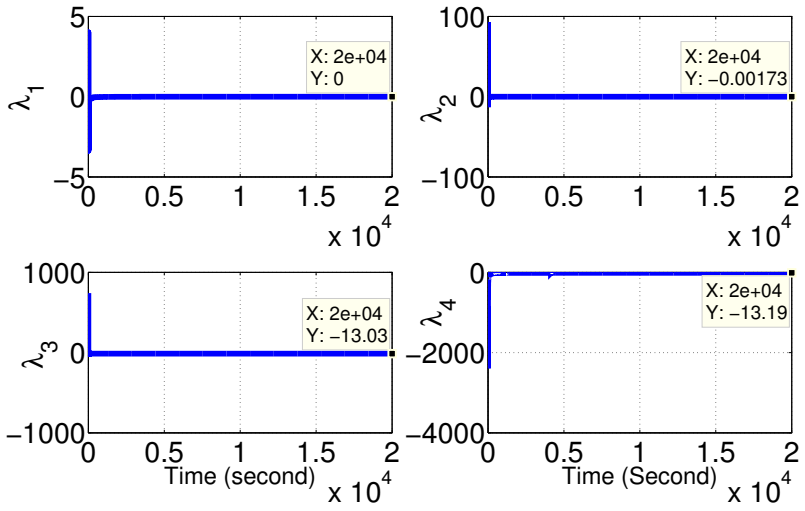


Figure 3.17: Evolution of system Lyapunov exponents (ordered in decreasing value).

perturbations, which suggests the control system is very sensitive to the variations in $\sigma_0$ and $\sigma_1$ values, therefore we bound the parameter perturbation region $\Gamma_1$ near the nominal values with a grid size of 0.05 to observe the subtle change in the qualitative behaviour in response to the parametric uncertainties. $\hat{\sigma_0}$ and $\hat{\sigma_1}$ will be perturbed in the following region $\Gamma_1$

$$\begin{aligned}\Gamma_1 = \big\{&\hat{\sigma_0} \in [99.998\,\%\, of\ \sigma_0\ nominal\ value, 100.003\,\%\, of\ \sigma_0\ nominal\ value]\,,\\ &\hat{\sigma_1} \in [98.548\,\%\, of\ \sigma_1\ nominal\ value, 106.675\,\%\, of\ \sigma_1\ nominal\ value]\big\}\end{aligned} \tag{3.29}$$

Values of LEs are used to determine the system stability associated with $\Gamma_1$ region, but it is inefficient and unfeasible due to long computation time and unreasonable load. Therefore, here the stability of each perturbed system is determined using the simulation results as suggested in [78]. The motion tendency of the system states based on the simulation is used to measure its stability for each perturbed system. Figure 3.18 shows the stability region defined by the simulations for all the conducted perturbed systems subject to the set $\Gamma_1$ in Eqn. (3.29). Three different colors are used to present the stability associated with each set of perturbed $\hat{\sigma_0}$ and $\hat{\sigma_1}$ values.

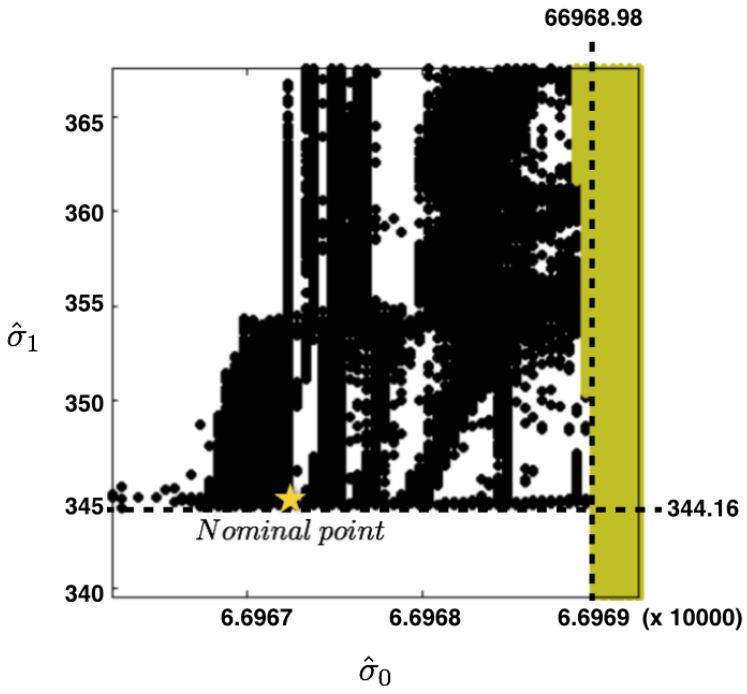


Figure 3.18: Structure stability region of experimental rig determined by the simulation results. The golden star pins on the nominal $\sigma_0$ and $\sigma_1$ values.

Black dot suggests that the corresponding perturbed system retains a stable fixed point; white dot indicates that the corresponding perturbed system has a stable limit cycle; yellow dot represents that the corresponding perturbed system has the state trajectories diverging rapidly from the initial condition.

Let us firstly examine how the system stability varies along with the perturbed $\hat{\sigma_0}$ (horizontal axis). As shown in Fig. 3.18 that all the perturbed systems with $\hat{\sigma_0}$ greater than a critical value $\hat{\sigma_0} = 66968.98$ are unstable. The systems having the perturbed $\hat{\sigma_0}$ values from the nominal to the critical value demonstrate a mixture of three different colors. However, it is obvious that the black dots dominate over other colors, indicating that the qualitative behavior of the perturbed system has a great chance to be stable if the perturbations are bounded within this window. When we gradually perturb $\hat{\sigma_0}$ from the nominal to its left boundary defined in Eqn. (3.29), most of the perturbed systems within this window are observed to possess the limit

cycle in their qualitative behavior. Based on the discussion here, it is concluded that the controller adopted in this study is highly sensitive to varying $\hat{\sigma_0}$ values. A minor perturbation less than 0.01% off its nominal value can potentially deviate its qualitative behavior from a stable fixed point to the limit cycle or even unstable state, which is a signature of poor robustness.

We now examine how the system stability varies along with the perturbed $\hat{\sigma_1}$ (vertical axis). As shown in Fig. 3.18 that a system having $\hat{\sigma_1}$ lower than the critical value of 344.16 will demonstrate either limit cycle or unstable state. When we gradually perturb $\hat{\sigma_1}$ from the nominal to its upper boundary defined in Eqn. (3.29), it is found that the the black and white data points equally dominate the area while the yellow dots only take a small portion. It appears that regardless of how little $\hat{\sigma_1}$ varies around its nominal value, the perturbed system is less likely to have qualitatively the same dynamics as the nominal system based on the distribution of the white and the yellow data points. Therefore, we again draw a conclusion that the controller in this system is sensitive to the varying $\hat{\sigma_1}$ values.

### 3.5.2 Structural Stability Analysis for NCTF Controller

Stability analysis is carried out to demonstrate the effect of parameter perturbations subject to this controller, and the initial conditions for system states and the time length are consistent with the one used in Section 3.5.1. Unlike the input-output linearization controller in which the control law can be written explicitly in terms of the parameters of interest $(\sigma_0, \sigma_1)$, the NCTF controller is mainly governed by a NCT and a conventional PI controller. The NCT is modeled by the open-loop velocity responses $h$ subject to the plant input $u_s$, and the $K_p$ and $K_i$ are designed based on that $h$ value as well, i.e. the NCTF controller does not directly take $\sigma_0$ and $\sigma_1$ as the independent variables to construct the controller, which indicates that we are not able to perturb the $\sigma_0$ and $\sigma_1$ values used in the controller. Therefore, for this controller, we firstly perturb the parameters in the plant friction model. Each set of perturbed $\sigma_0$ and $\sigma_1$ values results in a unique NCTF controller, and the original unperturbed system controlled by the NCTF controller derived with the perturbations is studied

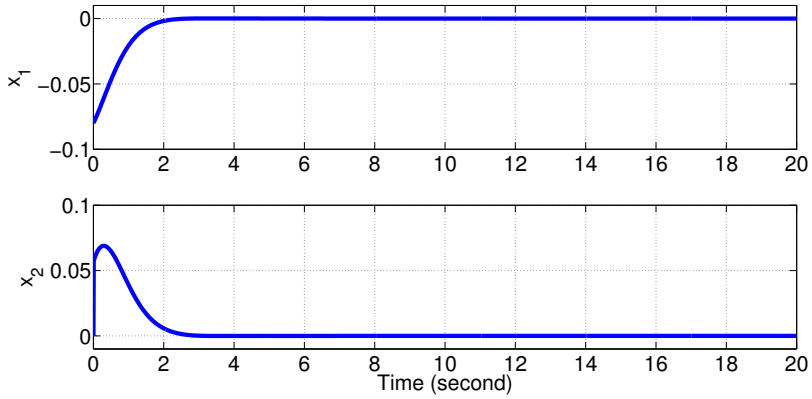


Figure 3.19: States $x_1$ and $x_2$ of NCTF control system.

and used to calculate its LE spectrum. All the LE spectra representing the perturbed systems are taken to define their qualitative behaviors. Two perturbed systems are presented in the following along with their time trajectories of system states and the evolution of the system LEs, from which the effect of the perturbations can be clearly seen. Additionally, $\sigma_0$ and $\sigma_1$ values in the plant friction model are perturbed in region $\Gamma_2$ defined in Section 3.5.2.3 where the qualitative behavior of each perturbed system is presented by different colors.

#### 3.5.2.1 Perturbed System 1:

$$(\boldsymbol{\sigma_0, \sigma_1}) = (\mathbf{70}\,\%\,\boldsymbol{of}\ \boldsymbol{\sigma_0}\ \boldsymbol{nominal\ value}, \mathbf{70}\,\%\,\boldsymbol{of}\ \boldsymbol{\sigma_1}\ \boldsymbol{nominal\ value})$$

The NCTF controller is derived from the plant model in which the $\sigma_0$ and $\sigma_1$ values are adjusted to 70% of the nominal $\sigma_0$ value and 70% of the nominal $\sigma_1$ value, respectively. This means $\sigma_0 = 46877.06$ and $\sigma_1 = 241.19$. Such a NCTF controller derived with the perturbations is used to control the unperturbed plant. The initial conditions for system states and the time length are consistent with the one used in Section 3.4.2.2. Figure 3.19 and 3.20 demonstrate that time trajectories of all the system states. All the states converge quickly after the trial is launched. The convergence of the state trajectories can be typically linked to a stable system. Figure 3.21 depicts the evolution of all system LEs, from which it can be observed

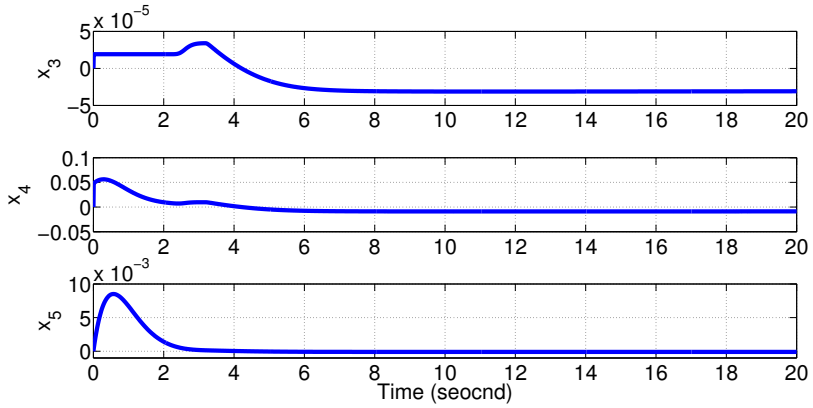


Figure 3.20: States $x_3$, $x_4$ and $x_5$ of NCTF control system.

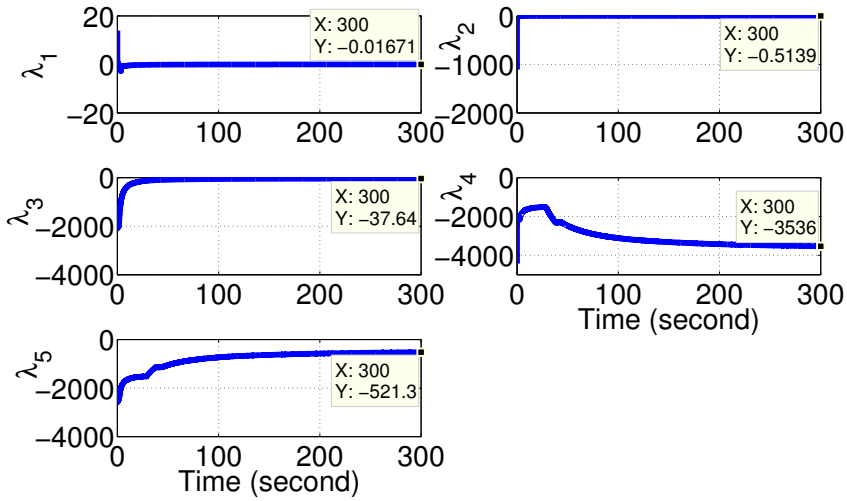


Figure 3.21: Evolution of system Lyapunov exponents (ordered in decreasing value).

that all the exponents converge to the negative values. The negative largest LE $\lambda_1$ in Fig. 3.21 suggests that the perturbed system has a stable fixed point.

The NCTF controller introduces a PI compensator as shown earlier in the design stage, and typically a PI compensator will improve the steady-state error at the expense of system stability since the I compensator makes the system one order higher than the original system. The system subject to the PI compensator may be less stable or even become unstable if the controller gains $K_p$ and $K_i$ are not properly

selected. Based on our numerical findings shown in Figs. 3.19 and 3.20, it is seen that the procedure proposed in [71] for the design of the controller gains $K_p$ and $K_i$ is quite robust against the variation in the LuGre friction model since the controller derived from the largely perturbed plant model can still stabilize the unperturbed system. This finding in terms of robustness is in agreement with experimental results reported in [71, 73].

#### 3.5.2.2 Perturbed System 2:

$$(\boldsymbol{\sigma_0, \sigma_1}) = (\mathbf{130\,\%\, of\ \sigma_0\ nominal\ value, 130\,\%\, of\ \sigma_1\ nominal\ value})$$

The NCTF controller is derived from the plant model in which the $\sigma_0$ and $\sigma_1$ values are adjusted to 130% of the nominal $\sigma_0$ value and 130% of the nominal $\sigma_1$ value, respectively. This means $\sigma_0 = 87057.4$ and $\sigma_1 = 447.93$. Such a NCTF controller derived with the perturbations is used to control the unperturbed plant. The initial conditions for system states and the time length are consistent with the one used in Section 3.4.2.2. Figures 3.22 and 3.23 demonstrate the time trajectories of all the system states. All the states converge quickly after the trial is launched. One can easily verify that with the same initial condition, the system state trajectories of this perturbed system do not show a significant difference comparing with perturbed system 1, i.e. this particular controller is not sensitive to the perturbations within the $(\sigma_0, \sigma_1)$ values. In practice, it is usually desirable for a controller to have this uniformity in the system state trajectories since it is a signature of robustness to parameter variations. Figure 3.24 depicts the evolution of all system LEs, from which it can be observed that all the exponents converge to the negative values as shown in each sub-datatips. The negative largest LE $\lambda_1$ in Fig. 3.24 suggests that the perturbed system has a stable fixed point.

#### 3.5.2.3 Perturbation Region $\Gamma_2$

In this section, the parameters of this control system are perturbed with a grid

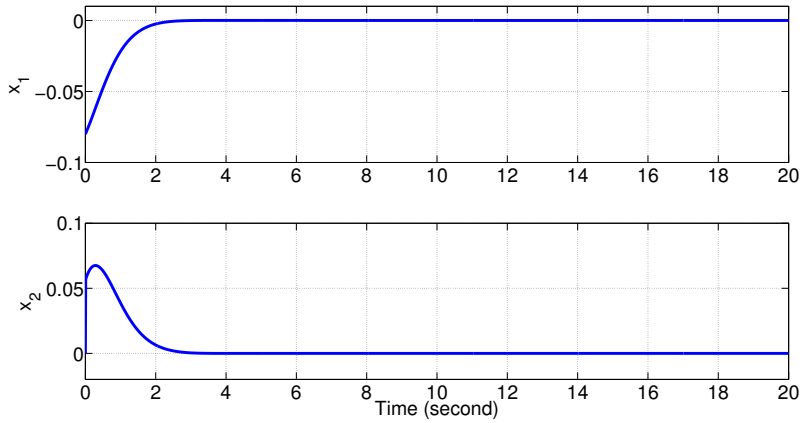


Figure 3.22: States $x_1$ and $x_2$ of NCTF control system.

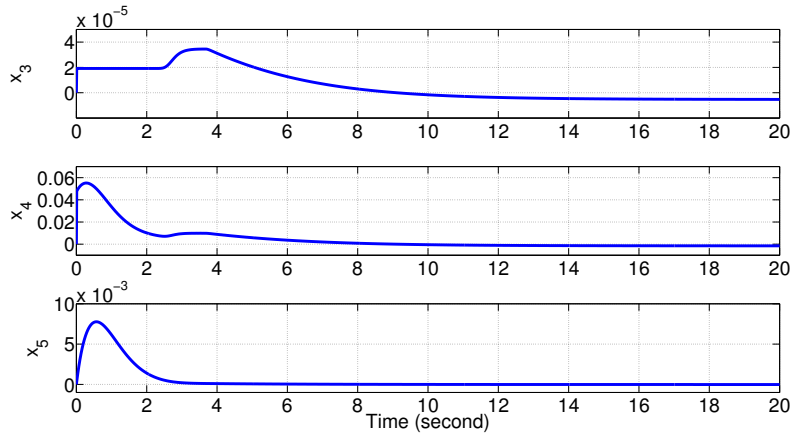


Figure 3.23: States $x_3$, $x_4$ and $x_5$ of NCTF control system.

size of 5% in a region $\Gamma_2$ bounded by

$$\begin{aligned}\Gamma = \{&\sigma_0 \in [70\,\%\,of\,\sigma_0\,nominal\,value, 130\,\%\,of\,\sigma_0\,nominal\,value]\,,\\ &\sigma_1 \in [70\,\%\,of\,\sigma_1\,nominal\,value, 130\,\%\,of\,\sigma_1\,nominal\,value]\,\}\end{aligned} \tag{3.30}$$

where the nominal values for $\sigma_0$ and $\sigma_1$ are listed in Tab. 3.1. Each set of perturbed $\sigma_0$ and $\sigma_1$ results in an independent NCTF controller, and the original unperturbed system controlled by each NCTF controller derived with the perturbations is studied and used to calculate its LE spectrum. All the LE spectra representing the perturbed systems are taken to define their qualitative behaviours. Tables 3.3 and 3.4 shows the

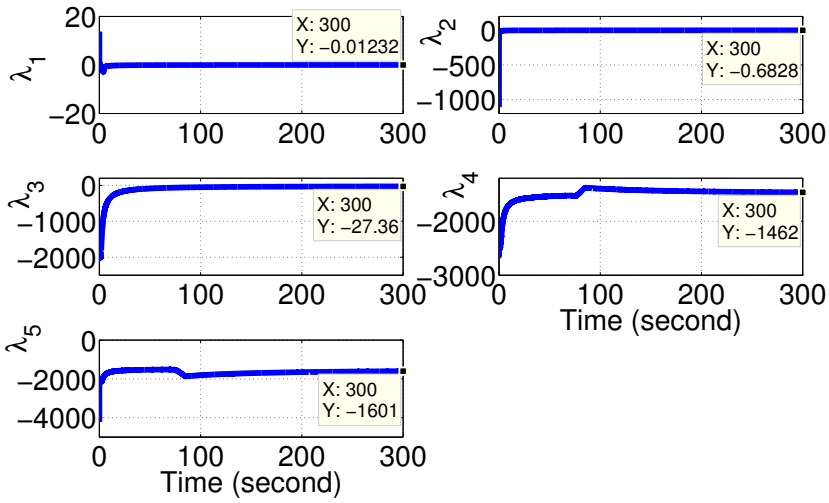


Figure 3.24: Evolution of system Lyapunov exponents (ordered in decreasing value).

general trends of largest LEs obtained from all the perturbed systems subject to the set $\Gamma_2$ in Eqn. (3.30), where one can observe that all the systems have negative largest exponents, which indicates that all the perturbed systems have qualitatively the same dynamics as the unperturbed system. This consistency in qualitative behaviour explains why we do not draw the stability results for all the perturbed systems on the $\sigma_0 - \sigma_1$ plane as in Fig. 3.18 since the plane will be entirely covered by black dots.

As can be observed in Tabs. 3.3 and 3.4, the largest LE value is not governed by the $\sigma_0$ value. As the $\sigma_0$ values are perturbed from 70% to 130% with respect to its nominal value under the same $\sigma_1$ values, the largest LE values remain unchanged; by contrast, the largest LE values increase along with the increasing $\sigma_1$ values. Note that one cannot conclude that the state trajectories of a system with larger value of the negative largest LE will converge faster to the equilibrium point than the one having a lower value of the negative largest LE. As a matter of fact, LEs only describe the average exponential rate of expansion or contraction of the principal axes of the infinitesimal n-(hyper)sphere of initial conditions. The $i^{th}$ LE does not relate to the dynamics of the $i^{th}$ state in the phase space. This concept is confirmed and pointed out in [68].

Based on the observation from Tabs. 3.3 and 3.4, it is obvious that the NCTF controller subject to our plant is insensitive to the friction parameter variation $(\sigma_0, \sigma_1)$ in comparison with the input-output linearization controller. Perturbations are unavoidable and normally lead to performance degradation in a control system, and control engineers naturally favor a controller that can withstand such uncertainties when performing the tasks of interest.

| | 70 % of $\sigma_0$ | 75 % of $\sigma_0$ | 80 % of $\sigma_0$ | 85 % of $\sigma_0$ | 90 % of $\sigma_0$ | 95 % of $\sigma_0$ | 100 % of $\sigma_0$ |
|---|---|---|---|---|---|---|---|
| 70 % of $\sigma_1$ | -0.0167 | -0.0167 | -0.0167 | -0.0167 | -0.0167 | -0.0167 | -0.0167 |
| 75 % of $\sigma_1$ | -0.0161 | -0.0161 | -0.0161 | -0.0161 | -0.0161 | -0.0161 | -0.0161 |
| 80 % of $\sigma_1$ | -0.0154 | -0.0154 | -0.0154 | -0.0154 | -0.0154 | -0.0154 | -0.0154 |
| 85 % of $\sigma_1$ | -0.0147 | -0.0147 | -0.0147 | -0.0147 | -0.0147 | -0.0147 | -0.0147 |
| 90 % of $\sigma_1$ | -0.0142 | -0.0142 | -0.0142 | -0.0142 | -0.0142 | -0.0142 | -0.0142 |
| 95 % of $\sigma_1$ | -0.0137 | -0.0137 | -0.0137 | -0.0137 | -0.0137 | -0.0137 | -0.0137 |
| 100 % of $\sigma_1$ | -0.0134 | -0.0134 | -0.0134 | -0.0134 | -0.0134 | -0.0134 | -0.0134 |
| 105 % of $\sigma_1$ | -0.0130 | -0.0130 | -0.0130 | -0.0130 | -0.0130 | -0.0130 | -0.0130 |
| 110 % of $\sigma_1$ | -0.0127 | -0.0127 | -0.0127 | -0.0127 | -0.0127 | -0.0127 | -0.0127 |
| 115 % of $\sigma_1$ | -0.0125 | -0.0125 | -0.0125 | -0.0125 | -0.0125 | -0.0125 | -0.0125 |
| 120 % of $\sigma_1$ | -0.0124 | -0.0124 | -0.0124 | -0.0124 | -0.0124 | -0.0124 | -0.0124 |
| 125 % of $\sigma_1$ | -0.0123 | -0.0123 | -0.0123 | -0.0123 | -0.0123 | -0.0123 | -0.0123 |
| 130 % of $\sigma_1$ | -0.0123 | -0.0123 | -0.0123 | -0.0123 | 0.0123 | -0.0123 | -0.0123 |

Table 3.3: Largest Lyapunov exponents for perturbed systems subject to region $\Gamma_2$.

| | 105 % of $\sigma_0$ | 110 % of $\sigma_0$ | 115 % of $\sigma_0$ | 120 % of $\sigma_0$ | 125 % of $\sigma_0$ | 130 % of $\sigma_0$ |
|---|---|---|---|---|---|---|
| 70 % of $\sigma_1$ | -0.0167 | -0.0167 | -0.0167 | -0.0167 | -0.0167 | -0.0167 |
| 75 % of $\sigma_1$ | -0.0161 | -0.0161 | -0.0161 | -0.0161 | -0.0161 | -0.0161 |
| 80 % of $\sigma_1$ | -0.0154 | -0.0154 | -0.0154 | -0.0154 | -0.0154 | -0.0154 |
| 85 % of $\sigma_1$ | -0.0147 | -0.0147 | -0.0147 | -0.0147 | -0.0147 | -0.0147 |
| 90 % of $\sigma_1$ | -0.0142 | -0.0142 | -0.0142 | -0.0142 | -0.0142 | -0.0142 |
| 95 % of $\sigma_1$ | -0.0137 | -0.0137 | -0.0137 | -0.0137 | -0.0137 | -0.0137 |
| 100 % of $\sigma_1$ | -0.0134 | -0.0134 | -0.0134 | -0.0134 | -0.0134 | -0.0134 |
| 105 % of $\sigma_1$ | -0.0130 | -0.0130 | -0.0130 | -0.0130 | -0.0130 | -0.0130 |
| 110 % of $\sigma_1$ | -0.0127 | -0.0127 | -0.0127 | -0.0127 | -0.0127 | -0.0127 |
| 115 % of $\sigma_1$ | -0.0125 | -0.0125 | -0.0125 | -0.0125 | -0.0125 | -0.0125 |
| 120 % of $\sigma_1$ | -0.0124 | -0.0124 | -0.0124 | -0.0124 | -0.0124 | -0.0124 |
| 125 % of $\sigma_1$ | -0.0123 | -0.0123 | -0.0123 | -0.0123 | -0.0123 | -0.0123 |
| 130 % of $\sigma_1$ | -0.0123 | -0.0123 | -0.0123 | -0.0123 | -0.0123 | -0.0123 |

Table 3.4: Largest Lyapunov exponents for perturbed systems subject to region $\Gamma_2$ (cont'd).

## 3.6 Summary

A controlled ball screw mechanical system proposed in Chapter 2 has been formulated in state space framework, the friction of which is modelled by the modified

LuGre friction model. Two set-point position controllers, namely the input-output linearization controller and the NCTF controller, are synthesized based on such a state space model. The effect of perturbed $\sigma_0$ and $\sigma_1$ values on the controlled mechanical system is investigated by carrying out the stability analysis using the concept of LEs.

The stability results from two control systems showed that the varying $\sigma_0$ and $\sigma_1$ values have an obvious effect on the system stability. The input-output linearization controller employed to perform the set-point position control on the investigated setup is very sensitive to the parametric uncertainties. The minor perturbations less than 0.01% off the nominal $\sigma_0$ and $\sigma_1$ values can result in limit cycles on the phase portrait and even diverging system states. In contrast, qualitative behavior of the nominal characteristic trajectory following (NCTF) controller remains unchanged when the studied parameters are perturbed 30% more or less with respect to the nominal values. For the mechanical system under consideration in this thesis, the NCTF controller is superior to the input-output linearization controller as the NCTF controller is more robust to the disturbed $\sigma_0$ and $\sigma_1$ values. The poor robustness of the input-output linearization control system is the result of the inability of the controller to deal with parametric uncertainties within this specific setup.

In summary, the outcome of this chapter provides qualitative insight into the effect of parametric uncertainties of an advanced friction model on a control system's behavior. The modified LuGre model is encouraged to be used for various analysis [70], as it captures the friction features surveyed in Chapter 1. If one is designing a system in which the friction is described by such a friction model, the foremost consideration is to ensure the variation of $\sigma_0$ and $\sigma_1$ can be carefully compensated by the controller used for the control tasks. While controllers vary from system to system, the parametric variations of the modified LuGre model are basically unavoidable. Consequently, the results presented here could provide qualitative insight into the behavior of a variety of control systems.

# Chapter 4

# Conclusions

This chapter presents a summary of the research contributions and recommendation for further research in this area.

## 4.1 Contributions

The contributions and findings of this thesis are summarized here:

1. A versatile experimental setup powered by DC motor is designed and fabricated to provide accurate friction data. The design choice is based on the criteria of the simplicity and flexibility in terms of altering contact conditions, little attention has been given to these two factors in the setup design dedicated to friction investigation. It has been shown experimentally that the friction features in either presliding regime or gross-sliding regime can be satisfactorily demonstrated by our setup. Moreover, the setup can be used to parameterize the chosen friction models. While friction does vary from system to system, its basic behaviours are the same in many mechanical systems. The proposed setup is able to provide valuable friction data that would allow a better understanding and modelling of the friction. It is a very effective and practical setup for friction-related studies. The novelty and the experimental results of the the proposed setup have been discussed and published in [79, 80].

2. A comprehensive experimental-numerical friction feature comparison for the candidate models has been conducted. The unique experimental friction features are compared with the numerical model outputs, where the discrepancies help us judge the accuracy of the models. A series of profound discussions addressing the relation between the candidate models structures and their numerical friction feature predictions are provided, which help modify the existing models or develop new advanced models. Table 2.12 summarizes the properties of the candidate friction models, which can be useful for researchers selecting the most relevant friction models for their applications. The significance and the results of such a comprehensive friction feature comparison have been discussed and published in [81]. It must be underlined that the LuGre friction model is a realistic model for simulations and analyses, especially where the nonlinear friction features occur.

3. Two set-point position controllers are synthesized based on the plant state space model in which the friction is modelled by the modified LuGre model. By means of Lyapunov exponents, the effect of the varying $\sigma_0$ and $\sigma_1$ values on the stability of the studied control systems is examined. It has been shown that the first control system integrating input-output linearization controller is sensitive to the perturbed $\sigma_0$ and $\sigma_1$ values, whereas the NCTF controller can still stabilize the system output in the presence of significant parameter variation. It is concluded that the variation of $\sigma_0$ and $\sigma_1$ has an obvious effect on the stability of the studied control systems and should not be overlooked in the design phase. The framework of systematic stability analysis conducted in this work is thus recommended to avoid undesired qualitative behaviors of control systems experiencing friction. It must be underlined that although the NCTF controller demonstrates better robustness when controlling the mechanical system proposed in Chapter 2, but such a robustness is not guaranteed if the system to be controlled is altered. In practice, the robustness of a controller is strongly influenced by the characteristics of the system to be controlled, and should be systematically examined in the design phase.

## 4.2 Future Work

The outlines of future work are described below:

1. To extent the stability analysis results subject to the LuGre model on various friction compensation techniques, it is expected to have more controllers such as sliding, adaptive, bang-bang or fuzzy controller synthesize based on our plant model. Afterwards the stability analysis results of these control systems can be rigorously carried out where the robustness of various control systems can be explored. It must be underlined that some of the aforementioned controllers involve the use of switching functions in response to the system feedback, in this case the control system becomes non-smooth and the algorithm employed in this thesis for the LEs calculation is invalid. Other algorithms meant for dynamical systems with discontinuities should be considered for LEs calculation.

2. Perturbing $\sigma_0$ and $\sigma_1$ values in this thesis are motivated by the fact that they are experimentally challenging to be parameterized. However, apart from which, the perturbations arisen from other parameters in the modified LuGre model are expected. It has been shown that the qualitatively behaviour of a system controlled by PID controller varies with different values of parameter $F_c$ and $F_s$ [4]. This means that $F_c$ and $F_s$ values may also have a significant effect on the qualitative behaviour of a system controlled by other controllers. Thus, it would be of interest to learn the stability of a control system with respect to the varying $F_c$ and $F_s$ values.

# Appendix: Detailed description of $f(x)$ and $\hat{f}(x)$

Appendix provides two functions $f(x)$ and $\hat{f}(x)$ presented in Chapter 3.4.1.1. $f(x)$ is presented in Eqn. (3.17) that describes a direct relation between the controlled state $x_1$ and the controller output $u$, and $\hat{f}(x)$ is part of the controller output $u$ presented in Eqn. (3.18).

$f(x)$ in Eqn. (3.17) has the form of

$$
\begin{aligned}
f = & -\frac{k_{tpm}R_a 2\pi p x_4}{mL_a} - \frac{k_{tpm}k_{apm}4\pi^2 p^2 x_2}{mL_a} - \frac{\sigma_0}{m}\left(S_v^2 x_2 - \sigma_0 \frac{S_v x_2 x_3}{g(x_2)}\right) \\
& + \frac{2\sigma_0\sigma_1}{m^2\pi}\left[\frac{\frac{K_v x_2}{1+K_v^2 x_2^2}\left(k_{tpm}x_4 2\pi p - \sigma_0 x_3 - \sigma_1 S_v^2 x_2 + \frac{\sigma_0\sigma_1 S_v x_2 x_3}{g(x_2)} - \sigma_2 x_2\right)}{g(x_2)}\right] \\
& - \frac{8\sigma_1}{m^2\pi^2}\arctan(K_v x_2)\frac{K_v x_2}{1+K_v^2 x_2^2}\left(k_{tpm}x_4 2\pi p - \sigma_0 x_3 - \sigma_1 S_v^2 x_2 + \frac{\sigma_0\sigma_1 S_v x_2 x_3}{g(x_2)} - \sigma_2 x_2\right) \\
& - \frac{4\sigma_1}{m^2\pi^2}\left(\arctan(K_v x_2)\right)^2\left(k_{tpm}x_4 2\pi p - \sigma_0 x_3 - \sigma_1 S_v^2 x_2 + \frac{\sigma_0\sigma_1 S_v x_2 x_3}{g(x_2)} - \sigma_2 x_2\right) \\
& + \frac{2\sigma_0\sigma_1}{m^2\pi}\left[\frac{\arctan(K_v x_2)\, x_3\left(k_{tpm}x_4 2\pi p - \sigma_0 x_3 - \sigma_1 S_v^2 x_2 + \frac{\sigma_0\sigma_1 S_v x_2 x_3}{g(x_2)} - \sigma_2 x_2\right)}{g(x_2)}\right] \\
& + \frac{2\sigma_0\sigma_1}{m\pi}\left[\frac{\arctan(K_v x_2) x_2\left(S_v^2 x_2 - \sigma_0\frac{S_v x_2}{g(x_2)} x_3\right)}{g(x_2)}\right] \\
& - \frac{\sigma 2}{m^2}\left(k_{tpm}x_4 2\pi p - \sigma_0 x_3 - \sigma_1 S_v^2 x_2 + \frac{\sigma_0\sigma_1 S_v x_2 x_3}{g(x_2)} - \sigma_2 x_2\right) \\
& + \left[\frac{4\sigma_0\sigma_1 \arctan(K_v x_2)\, x_2^2 x_3 (F_s - F_c)\, e^{-x_2^2/V_s^2}\left(k_{tpm}x_4 2\pi p - \sigma_0 x_3 - \sigma_1 S_v^2 x_2\right)}{m^2\pi V_s^2 g^2(x_2)}\right]
\end{aligned}
$$

$$+\left[\frac{4\sigma_0\sigma_1\arctan\left(K_v x_2\right)x_2^2 x_3\left(F_s-F_c\right)e^{-x_2^2/V_s^2}\left(\frac{\sigma_0\sigma_1 S_v x_2 x_3}{g(x_2)}-\sigma_2 x_2\right)}{m^2\pi V_s^2 g^2\left(x_2\right)}\right]$$

and $\hat{f}(x)$ in Eqn. (3.18) determining the controller output has the form of

$$\begin{aligned}
\hat{f} =& -\frac{k_{tpm}R_a 2\pi p x_4}{mL_a}-\frac{k_{tpm}k_{apm}4\pi^2 p^2 x_2}{mL_a}-\frac{\hat{\sigma_0}}{m}\left(S_v^2 x_2-\hat{\sigma_0}\frac{S_v x_2 x_3}{\hat{g}\left(x_2\right)}\right)\\
&+\frac{2\hat{\sigma_0}\hat{\sigma_1}}{m^2\pi}\left[\frac{\frac{K_v x_2}{1+K_v^2 x_2^2}\left(k_{tpm}x_4 2\pi p-\hat{\sigma_0}x_3-\hat{\sigma_1}S_v^2 x_2+\frac{\hat{\sigma_0}\hat{\sigma_1}S_v x_2 x_3}{\hat{g}(x_2)}-\hat{\sigma_2}x_2\right)}{\hat{g}\left(x_2\right)}\right]\\
&-\frac{8\hat{\sigma_1}}{m^2\pi^2}\arctan\left(K_v x_2\right)\frac{K_v x_2}{1+K_v^2 x_2^2}\left(k_{tpm}x_4 2\pi p-\hat{\sigma_0}x_3-\hat{\sigma_1}S_v^2 x_2+\frac{\hat{\sigma_0}\hat{\sigma_1}S_v x_2 x_3}{\hat{g}\left(x_2\right)}-\hat{\sigma_2}x_2\right)\\
&-\frac{4\hat{\sigma_1}}{m^2\pi^2}\left(\arctan\left(K_v x_2\right)\right)^2\left(k_{tpm}x_4 2\pi p-\hat{\sigma_0}x_3-\hat{\sigma_1}S_v^2 x_2+\frac{\hat{\sigma_0}\hat{\sigma_1}S_v x_2 x_3}{\hat{g}\left(x_2\right)}-\hat{\sigma_2}x_2\right)\\
&+\frac{2\hat{\sigma_0}\hat{\sigma_1}}{m^2\pi}\left[\frac{\arctan\left(K_v x_2\right)x_3\left(k_{tpm}x_4 2\pi p-\hat{\sigma_0}x_3-\hat{\sigma_1}S_v^2 x_2+\frac{\hat{\sigma_0}\hat{\sigma_1}S_v x_2 x_3}{\hat{g}(x_2)}-\hat{\sigma_2}x_2\right)}{\hat{g}\left(x_2\right)}\right]\\
&+\frac{2\hat{\sigma_0}\hat{\sigma_1}}{m\pi}\left[\frac{\arctan(K_v x_2)x_2\left(S_v^2 x_2-\hat{\sigma_0}\frac{S_v x_2}{\hat{g}(x_2)}x_3\right)}{\hat{g}\left(x_2\right)}\right]\\
&-\frac{\hat{\sigma_2}}{m^2}\left(k_{tpm}x_4 2\pi p-\hat{\sigma_0}x_3-\hat{\sigma_1}S_v^2 x_2+\frac{\hat{\sigma_0}\hat{\sigma_1}S_v x_2 x_3}{\hat{g}\left(x_2\right)}-\hat{\sigma_2}x_2\right)\\
&+\left[\frac{4\hat{\sigma_0}\hat{\sigma_1}\arctan\left(K_v x_2\right)x_2^2 x_3\left(\hat{F_s}-\hat{F_c}\right)e^{-x_2^2/\hat{V_s}^2}\left(k_{tpm}x_4 2\pi p-\hat{\sigma_0}x_3-\hat{\sigma_1}S_v^2 x_2\right)}{m^2\pi\hat{V_s}^2\hat{g}^2\left(x_2\right)}\right]\\
&+\left[\frac{4\hat{\sigma_0}\hat{\sigma_1}\arctan\left(K_v x_2\right)x_2^2 x_3\left(\hat{F_s}-\hat{F_c}\right)e^{-x_2^2/\hat{V_s}^2}\left(\frac{\hat{\sigma_0}\hat{\sigma_1}S_v x_2 x_3}{\hat{g}(x_2)}-\hat{\sigma_2}x_2\right)}{m^2\pi\hat{V_s}^2\hat{g}^2\left(x_2\right)}\right]
\end{aligned}$$

where $\hat{\sigma_0}, \hat{\sigma_1}, \hat{\sigma_2}, \hat{F_c}, \hat{F_s}$ and $\hat{V_s}$ are the adjustable parameters used to construct the controller's output. $\hat{g}\left(x_2\right)$ contains the adjustable parameters and is defined by

$$\hat{g}\left(x_2\right)=\hat{F_c}+\left(\hat{F_s}-\hat{F_c}\right)e^{-\left(x_2/\hat{V_s}\right)^2}$$

# References


[1] J. Wojewoda, A. Stefański, M. Wiercigroch, and T. Kapitaniak, "Hysteretic effects of dry friction: modelling and experimental studies," *Philosophical Transactions of the Royal Society A: Mathematical, Physical and Engineering Sciences*, vol. 366, no. 1866, pp. 747–765, 2008.

[2] C. C. De Wit and P. Lischinsky, "Adaptive friction compensation with partially known dynamic friction model," *International journal of adaptive control and signal processing*, vol. 11, no. 1, pp. 65–80, 1997.

[3] J. Awrejcewicz and P. Olejnik, "Friction pair modeling by a 2-dof system: numerical and experimental investigations," *International Journal of bifurcation and chaos*, vol. 15, no. 06, pp. 1931–1944, 2005.

[4] S. Jeon and M. Tomizuka, "Stability of controlled mechanical systems with ideal Coulomb friction," *Journal of Dynamic Systems, Measurement, and Control*, vol. 130, no. 1, p. 011013, 2008.

[5] E. G. Papadopoulos and G. C. Chasparis, "Analysis and model-based control of servomechanisms with friction," *Journal of dynamic systems, measurement, and control*, vol. 126, no. 4, pp. 911–915, 2004.

[6] P. E. Dupont and D. Bapna, "Stability of sliding frictional surfaces with varying normal force," *Journal of vibration and acoustics*, vol. 116, no. 2, pp. 237–242, 1994.

[7] B. Bona and M. Indri, "Friction compensation in robotics: an overview," in *Decision and Control, 2005 and 2005 European Control Conference. CDC-ECC'05. 44th IEEE Conference on*, pp. 4360–4367, IEEE, 2005.

[8] P. E. Dupont and D. Bapna, "Perturbation stability of frictional sliding with varying normal force," *Journal of vibration and acoustics*, vol. 118, no. 3, pp. 491–497, 1996.

[9] L. L. Liu, "Effects of the varying normal force on the stick slip motion of systems with friction," *Advanced Materials Research*, vol. 479, pp. 1078–1083, 2012.

[10] B. Armstrong-Helouvry, *Control of machines with friction*, vol. 128. Springer, 1991.

[11] B. Armstrong-Hélouvry, P. Dupont, and C. C. De Wit, "A survey of models, analysis tools and compensation methods for the control of machines with friction," *Automatica*, vol. 30, no. 7, pp. 1083–1138, 1994.

[12] J. Liang and B. Feeny, "A comparison between direct and indirect friction measurements in a forced oscillator," *Transactions-American Society of Mechanical Engineers Journal of Applied Mechanics*, vol. 65, pp. 783–785, 1998.

[13] J.-W. Liang and B. Feeny, "Dynamical friction behavior in a forced oscillator with a compliant contact," *Journal of Applied Mechanics*, vol. 65, no. 1, pp. 250–257, 1998.

[14] F. Al-Bender, V. Lampaert, and J. Swevers, "A novel generic model at asperity level for dry friction force dynamics," *Tribology Letters*, vol. 16, no. 1-2, pp. 81–93, 2004.

[15] C.-L. Chen, K. Lin, and C. Hsieh, "Presliding friction mode: modelling and experimental study with a ball-screw-driven set-up," *Mathematical and Computer Modelling of Dynamical Systems*, vol. 11, no. 4, pp. 397–410, 2005.

[16] S. Thiery, M. Kunze, A. Karimi, A. Curnier, and R. Longchamp, "Friction modeling of a high-precision positioning system," in *American Control Conference, 2006*, pp. 5–pp, IEEE, 2006.

[17] B. Bona, M. Indri, and N. Smaldone, "Nonlinear friction estimation for digital control of direct-drive manipulators," in *European Control Conference (ECC'03), Cambridge, UK*, 2003.

[18] J. Nakanishi, T. Fukuda, and D. E. Koditschek, "A brachiating robot controller," *Robotics and Automation, IEEE Transactions on*, vol. 16, no. 2, pp. 109–123, 2000.

[19] V. Johannes, M. Green, and C. Brockley, "The role of the rate of application of the tangential force in determining the static friction coefficient," *Wear*, vol. 24, no. 3, pp. 381–385, 1973.

[20] R. Richardson and H. Nolle, "Surface friction under time-dependent loads," *Wear*, vol. 37, no. 1, pp. 87–101, 1976.

[21] E. Rabinowicz, "The nature of the static and kinetic coefficients of friction," *Journal of applied physics*, vol. 22, no. 11, pp. 1373–1379, 1951.

[22] E. Rabinowicz, "The intrinsic variables affecting the stick-slip process," *Proceedings of the Physical Society*, vol. 71, no. 4, p. 668, 1958.

[23] D. Hess and A. Soom, "Friction at a lubricated line contact operating at oscillating sliding velocities," *Journal of Tribology*, vol. 112, no. 1, pp. 147–152, 1990.

[24] H. Yanada and Y. Sekikawa, "Modeling of dynamic behaviors of friction," *Mechatronics*, vol. 18, no. 7, pp. 330–339, 2008.

[25] A. Stefański, J. Wojewoda, M. Wiercigroch, and T. Kapitaniak, "Chaos caused by non-reversible dry friction," *Chaos, Solitons & Fractals*, vol. 16, no. 5, pp. 661–664, 2003.

[26] M. Wiercigroch, V. Sin, and Z. Liew, "Non-reversible dry friction oscillator: design and measurements," *Proceedings of the Institution of Mechanical Engineers, Part C: Journal of Mechanical Engineering Science*, vol. 213, no. 5, pp. 527–534, 1999.

[27] J. Wojewoda, R. Barron, and T. Kapitaniak, "Chaotic behavior of friction force," *International Journal of Bifurcation and Chaos*, vol. 2, no. 01, pp. 205–209, 1992.

[28] K. Guo, X. Zhang, H. Li, and G. Meng, "Non-reversible friction modeling and identification," *Archive of Applied Mechanics*, vol. 78, no. 10, pp. 795–809, 2008.

[29] P. R. Dahl, "A solid friction model," tech. rep., The Aerospace Corporation, 1968.

[30] J. Courtney-Pratt and E. Eisner, "The effect of a tangential force on the contact of metallic bodies," *Proceedings of the Royal Society of London. Series A. Mathematical and Physical Sciences*, vol. 238, no. 1215, pp. 529–550, 1957.

[31] H. Olsson, K. J. Åström, C. Canudas de Wit, M. Gäfvert, and P. Lischinsky, "Friction models and friction compensation," *European journal of control*, vol. 4, no. 3, pp. 176–195, 1998.

[32] P. R. Dahl, "Solid friction damping of spacecraft oscillations," tech. rep., DTIC Document, 1975.

[33] P. R. Dahl, "Measurement of solid friction parameters of ball bearings," tech. rep., DTIC Document, 1977.

[34] P. A. Bliman and M. Sorine, "Friction modelling by hysteresis operators. application to dahl, sticktion and stribeck effects," in *Proceedings of the Conference Models of Hytersis*, 1991.

[35] P. A. Bliman and M. Sorine, "A system-theoretic approach of systems with hysteresis. application to friction modelling and compensation," *In Proceedings of the second European Control Conference*, pp. 1844–1849, 1993.

[36] P. A. Bliman and M. Sorine, "Easy-to-use realistic dry friction models for automatic control," *In Proceedings of 3rd European Control Conference*, pp. 3788–3794, 1995.

[37] C. C. De Wit, H. Olsson, K. J. Astrom, and P. Lischinsky, "A new model for control of systems with friction," *Automatic Control, IEEE Transactions on*, vol. 40, no. 3, pp. 419–425, 1995.

[38] B. Jacobson, "The Stribeck memorial lecture," *Tribology International*, vol. 36, no. 2003, pp. 781–789, 2003.

[39] D. A. Haessig and B. Friedland, "On the modeling and simulation of friction," *Journal of Dynamic Systems, Measurement, and Control*, vol. 113, no. 3, pp. 354–362, 1991.

[40] D. Karnopp, "Computer simulation of stick-slip friction in mechanical dynamic systems," *Journal of dynamic systems, measurement, and control*, vol. 107, no. 1, pp. 100–103, 1985.

[41] M. Gäfvert, "Comparisons of two dynamic friction models," in *Control Applications, 1997., Proceedings of the 1997 IEEE International Conference on*, pp. 386–391, IEEE, 1997.

[42] C. C. De Wit, H. Olsson, K. Astrom, and P. Lischinsky, "Dynamic friction models and control design," in *American Control Conference, 1993*, pp. 1920–1926, IEEE, 1993.

[43] X. Song and D. G. Smedley, "Glitchless static friction models in simulink for vehicle simulation study," *Journal of Computational and Nonlinear Dynamics*, vol. 5, no. 1, p. 014502, 2010.

[44] N. B. Do, A. A. Ferri, and O. A. Bauchau, "Efficient simulation of a dynamic system with LuGre friction," *Journal of Computational and Nonlinear Dynamics*, vol. 2, no. 4, pp. 281–289, 2007.

[45] J. Swevers, F. Al-Bender, C. G. Ganseman, and T. Projogo, "An integrated friction model structure with improved presliding behavior for accurate friction compensation," *Automatic Control, IEEE Transactions on*, vol. 45, no. 4, pp. 675–686, 2000.

[46] F. K. Lieu, "Theoretical and experimental study of linear oscillator with Coulomb friction," bachelor thesis, University of Aberdeen, 1995.

[47] T. Tjahjowidodo, F. Al-Bender, and H. Van Brussel, "Friction identification and compensation in a DC motor," in *submitted to 16th IFAC World Congress, Prague*, 2005.

[48] W.-F. Xie, "Sliding-mode-observer-based adaptive control for servo actuator with friction," *Industrial Electronics, IEEE Transactions on*, vol. 54, no. 3, pp. 1517–1527, 2007.

[49] N. P. Mahajan and S. Deshpande, "Study of nonlinear behavior of DC motor using modeling and simulation," *International Journal of Scientific and Research Publications*, vol. 3, no. 3, pp. 576–581, 2013.

[50] S. Kato, N. Sato, and T. Matsubayashi, "Some considerations on characteristics of static friction of machine tool slideway," *Journal of Tribology*, vol. 94, no. 3, pp. 234–247, 1972.

[51] P. Olejnik and J. Awrejcewicz, "Application of hénon method in numerical estimation of the stick–slip transitions existing in Filippov-type discontinuous dynamical systems with dry friction," *Nonlinear Dynamics*, vol. 73, no. 1-2, pp. 723–736, 2013.

[52] J.-J. E. Slotine, W. Li, *et al.*, *Applied nonlinear control*, vol. 199. Prentice-hall Englewood Cliffs, NJ, 1991.

[53] M. Linker and J. Dieterich, "Effects of variable normal stress on rock friction- observations and constitutive equations," *Journal of Geophysical Research*, vol. 97, no. B4, pp. 4923–4940, 1992.

[54] S. Andersson, A. Söderberg, and S. Björklund, "Friction models for sliding dry, boundary and mixed lubricated contacts," *Tribology International*, vol. 40, no. 4, pp. 580–587, 2007.

[55] T. Piatkowski, "Dahl and LuGre dynamic friction models - the analysis of selected properties," *Mechanism and Machine Theory*, vol. 73, pp. 91–100, 2014.

[56] D. Chou, "Dahl friction modeling," tech. rep., Massachusetts Institute of Technology, 2004.

[57] G. Cumming, F. Fidler, and D. L. Vaux, "Error bars in experimental biology," *The Journal of Cell Biology*, vol. 177, no. 1, pp. 7–11, 2007.

[58] M. Gagvert, "Comparison of two friction models," Master's thesis, Lund University, 2012.

[59] M. Couillard, P. Masson, and P. Micheau, "Identification of friction parameters for limited relative displacement contacts," *Shock and Vibration*, vol. 16, no. 5, pp. 481–493, 2009.

[60] P. S. Gandhi, F. H. Ghorbel, and J. Dabney, "Modeling, identification, and compensation of friction in harmonic drives," in *Decision and Control, 2002, Proceedings of the 41st IEEE Conference on*, vol. 1, pp. 160–166, IEEE, 2002.

[61] R. H. Hensen, M. J. van de Molengraft, and M. Steinbuch, "Frequency domain identification of dynamic friction model parameters," *Control Systems Technology, IEEE Transactions on*, vol. 10, no. 2, pp. 191–196, 2002.

[62] Y. Q. Zheng, "Parameter identification of LuGre friction model for robot joints," *Advanced Materials Research*, vol. 479, pp. 1084–1090, 2012.

[63] P. Lischinsky, C. C. De Wit, and G. Morel, "Friction compensation for an industrial hydraulic robot," *Control Systems, IEEE*, vol. 19, no. 1, pp. 25–32, 1999.

[64] H. Olsson, *Control systems with friction*. PhD thesis, Lund University, 1996.

[65] J.-C. Mare, "Friction modelling and simulation at system level: a practical view for the designer," *Proceedings of the Institution of Mechanical Engineers, Part I: Journal of Systems and Control Engineering*, p. 0959651812441749, 2012.

[66] Y. Sun, M. Alghooneh, Y.-H. Sun, and C. Q. Wu, "On constrained and energy efficient balance control of a standing biped: Experimentation and stability analysis," *Journal of Dynamic Systems, Measurement, and Control*, vol. 136, no. 5, p. 054504, 2014.

[67] Y. Sun and C. Q. Wu, "Stability analysis via the concept of Lyapunov exponents: a case study in optimal controlled biped standing," *International Journal of Control*, vol. 85, no. 12, pp. 1952–1966, 2012.

[68] A. Wolf, J. B. Swift, H. L. Swinney, and J. A. Vastano, "Determining Lyapunov exponents from a time series," *Physica D: Nonlinear Phenomena*, vol. 16, no. 3, pp. 285–317, 1985.

[69] G. Chen, "Stability of nonlinear systems," *Encyclopedia of RF and Microwave Engineering*, pp. 4881–4896, 2004.

[70] M. Sobczyk, E. Perondi, and M. Cunha, "A continuous approximation of the LuGre friction model," in *ABCM Symposium Series in Mechatronics*, vol. 4, pp. 218–228, 2010.

[71] M. Wahyudi, "Robustness evaluation of two control methods for friction compensation of ptp positioning systems," 2003.

[72] R. M. Nor and S. H. Chong, "Positioning control of a one mass rotary system using NCTF controller," in *Control System, Computing and Engineering (ICCSCE), 2013 IEEE International Conference on*, pp. 381–386, IEEE, 2013.

[73] K. Sato, A. Shimokohbe, *et al.*, "Robustness evaluation of three friction compensation methods for point-to-point (ptp) positioning systems," *Robotics and Autonomous Systems*, vol. 52, no. 2, pp. 247–256, 2005.

[74] R. Akmeliawati, A. Wijaya, *et al.*, "Improved NCTF control method for a two mass point-to-point positioning system," in *Intelligent and Advanced Systems (ICIAS), 2010 International Conference on*, pp. 1–6, IEEE, 2010.

[75] K. Sato, A. Shimokohbe, *et al.*, "Characteristics of practical control for point-to-point (ptp) positioning systems: Effect of design parameters and actuator saturation on positioning performance," *Precision Engineering*, vol. 27, no. 2, pp. 157–169, 2003.

[76] K. Sato, K. Nakamoto, and A. Shimokohbe, "Practical control of precision positioning mechanism with friction," *Precision engineering*, vol. 28, no. 4, pp. 426–434, 2004.

[77] K. Sato, A. Shimokohbe, *et al.*, "Robustness evaluation of new practical control for ptp positioning systems," in *Advanced Intelligent Mechatronics, 2001. Proceedings. 2001 IEEE/ASME International Conference on*, vol. 2, pp. 843–848, IEEE, 2001.

[78] D. Koop, "Dynamics and stability of passive dynamic biped walking using an advanced mathematical model," Master's thesis, University of Manitoba, 2012.

[79] Y.-H. Sun, T. Chen, C. Q. Wu, and C. Shafai, "A comprehensive experimental setup for identification of friction model parameters," *Mechanism and Machine Theory*, vol. 100, pp. 338–357, 2016.

[80] Y.-H. Sun, T. Chen, and C. Shafai, "Parameter identification of LuGre friction model: Experimental set-up design and measurement," in *ASME 2015 International Mechanical Engineering Congress and Exposition*, pp. V04AT04A057–V04AT04A057, American Society of Mechanical Engineers, 2015.

[81] Y.-H. Sun, T. Chen, C. Q. Wu, and C. Shafai, "Comparison of four friction models: Feature prediction," *Journal of Computational and Nonlinear Dynamics*, vol. 11, no. 3, p. 031009, 2016.